UCLA
UCLA Electronic Theses and Dissertations

Title

Ionogels: Addressing the Challenges of Lithium Ion Solid Electrolytes

Permalink

https://escholarship.org/uc/item/0fj996q2

Author

Ashby, David

Publication Date

2018

Peer reviewed|Thesis/dissertation

UNIVERSITY OF CALIFORNIA

Los Angeles

Ionogels: Addressing the Challenges of Lithium Ion Solid Electrolytes

A dissertation submitted in partial satisfaction of the requirements for the degree Doctor of

Philosophy in Materials Science and Engineering

by

David Scott Ashby

2018

ABSTRACT OF THE DISSERTATION

Ionogels: Addressing the Challenges of Lithium Ion Solid Electrolytes

by

David Scott Ashby

Doctor of Philosophy in Materials Science and Engineering

University of California, Los Angeles, 2018

Professor Bruce S Dunn, Chair

Recently, ionogels, pseudo-solid-state electrolytes consisting of an ionic liquid electrolyte confined in a mesoporous inorganic matrix, have attracted interest for use as a solid electrolyte in Li^+ batteries because of their high ionic conductivity, stability, and solution processability. Herein, we report adapting the ionogel synthesis route through spin coat processing to obtain thin films. Films down to 600 nanometers were obtained that maintained the properties of the bulk ionogel. By using spin coating to achieve thin films, the ionogel can be processed directly on electrode surfaces as a sol. Thin film ionogels processed on lithium iron phosphate cathodes achieved capacities of 125 mAh g^{-1} at charge/discharge rates of 2 hours stably over 150 cycles, which corresponds to the highest reported power densities for silica ionogels. The sol-gel process was modified through the addition of a photoacid generator to add UV patternability. The UV crosslinked gel showed comparable properties and cycling to the spin-coated ionogel.

While having high achievable capacities, there have been few studies into deciphering the electrode-ionogel interface. The second section will review our work directed at understanding the interface for solution-processable ionogel electrolytes with various electrode materials. Using XPS, Raman spectroscopy, and electrochemical testing to probe the electrode-ionogel interface, surface reactions were identified as being the source of the interfacial barriers. Our results indicate that the acidity of the sol led to reduction of the transition metal and breakdown of the solvent and organic acid, forming an organic surface layer, which impedes Li^+ transport. By adjusting the silica gelation route these interfacial reactions can be avoided, leading to stable cycling.

The high ionic conductivity of ionogels shown in Chapter 3, in comparison to other solid electrolytes, and its solution processability opens the possibility for incorporation into multidimensional cell designs. The last portion of my dissertation will explore using the ionogel electrolyte to form a 2.5D cell consisting of a 3D $LiFePO_4$ cathode and 2D Li metal anode. The electrolyte is shown to penetrate uniformly throughout the 3D electrode array and into each individual post. High areal capacities (1.1 mAh cm^{-2}) were achieved at 1 mA cm^{-2} with a stable capacity retention at 0.5 mA cm^{-2} over 50 cycles. The 2.5D cell is comparable or better than current 3D batteries in literature.

The dissertation of David Scott Ashby is approved.

Jeffrey I. Zink

Jane Pei-Chen Chang

Ximin He

Bruce S. Dunn, Committee Chair

University of California, Los Angeles

2018

To Christini

and my parents Mike and Robbi

Table of Contents

List of Figures

List of Tables

through the project and ensured that I graduated on time. Thank you for also helping address all of the issues with fabricating the posts.

Last, I would like to thank Professor Suneel Kodambaka for his advice and opportunities provided during my undergraduate studies. The opportunity provided by Professor Kodambaka to work in his lab and internship at LLNL led me to want to pursue a PhD degree and continue working in research and development.

Vita

2011-2014   *Undergraduate Student Researcher*- Electrodeposition of CNT Yarns

Professor Suneel Kodambaka

University of California, Los Angeles

2013-2014   *Undergraduate Research Scholars Program (URSP)*

University of California, Los Angeles

2013   *Research Assistant- In-situ* AFM Analysis of Electrodeposited Zn

Lawrence Livermore National Labs

Chris Orme

2014   B.S. in Materials Science and Engineering

University of California, Los Angeles

2014-2015   *Research Assistant*- Electrodeposition of Co-Re Alloys

HRL Laboratories

2014-2018   *Graduate Student Researcher*

Professor Bruce Dunn

University of California, Los Angeles

2016   M.S. in Materials Science and Engineering

University of California, Los Angeles

Publications and Patents

- Lau J, Deblock R, Butts D, **Ashby D**, Choi C, and Dunn B. "Sulfide Solid Electrolytes for Lithium Battery Applications." **Adv. Energy Mater.** 2018, 1800933.

- Munteshari O, Lau J, **Ashby D**, Dunn B, and Pilon L. "Effects of constituent materials on heat generation in individual EDLC electrodes." **J. Electrochem. Soc.** 2018, *165,* A1547-1557.

- Martinez J, **Ashby D**, Zhu C, Dunn B, Baker L, and Siwy Z. "Probing ion current in solid-electrolytes at the meso- and nanoscale" **Faraday Discuss.** 2018,*210*, 55-67 .

- Lai CH, **Ashby D**, Lin T, Lau J, Dawson A, Tolbert S, and Dunn B. "Application of Poly(3-hexylthiophene-2,5-diyl) as a Protective Coating for High Rate Cathode Materials." **Chem. Mater.** 2018, 30 (8), 2589–2599.

- **Ashby D**, DeBlock R, Lai CH, Choi C, and Dunn B. "Patternable, Solution-Processed Ionogels for Thin-Film Lithium-Ion Electrolytes." **Joule** 2017, *1*, 2, 344-358.

- Martin H, **Ashby D**, and Schaedler T. "Thin walled high temperature alloy structures via additive manufacturing and metal deposition." **Mater. Des.** 2017, *120,* 291-297.

- Lai CH, **Ashby D**, Moz M, Gogotsi Y, Pilon L, and Dunn B. "Designing Pseudocapacitance for Nb_2O_5/Carbide-Derived Carbon Electrodes and Hybrid Devices." **Langmuir** 2017, *33* (37), 9407–9415.

- Smith L, Malati P, Fang J, Richardson W, **Ashby D**, Lai CH, and Dunn B. "Sol–gel encapsulated lithium polysulfide catholyte and its application in lithium–sulfur batteries." **Mater. Horiz**. 2016,*3*, 137-144.

Chapter 1: Introduction and Objectives

      With the start of the information age in the 1970's, technology has consistently strived for smaller, lightweight, energy-efficient devices. This is best visualized with the current desire for the internet of things (IoT), the interconnectedness and miniaturization of electronics. Many electronic components have progressively become more energy efficient and smaller, such as transistors, actuators, cameras, and antennas, which has allowed the penetration of wireless technologies through our society. Integration into household devices such as water heaters, refrigerators, and air conditioning units, allows the devices to communicate with each other and better respond to fluctuating energy demands (Figure 1.1).[1] Not only could this lower individual household bills, but it also could improve the flexibility of the energy grid, which ensures better utilization of renewable energy sources. For the improvement to be realized, small, wireless connected nodes must be developed that can operate without external power. These nodes will require small components, especially batteries that can supply energy reliably and at appreciable rates.
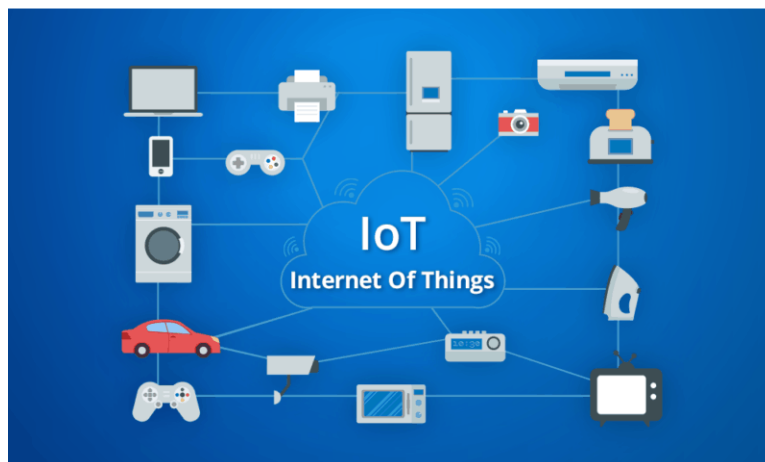
Figure 1.1: The Internet of Things

Though many electronic components have improved at a steady rate, the same cannot be said about energy storage technologies. Recently the Joint Center for Energy Storage Research disclosed that from the 1990's to 2015 Li^+ batteries cost per kWh has decreased by six times and gravimetric density has tripled to 250 Wh kg^{-1}.[2] This improvement, while impressive, has not kept up with the year-to-year improvements in microelectronic technologies facilitated by the rise of new fabrication techniques, such as microelectromechanical systems (MEMS) (Figure 1.2). Thus, batteries remain the largest volumetric and gravimetric component of small electronics such as cellphones, tablets, and smart accessories.
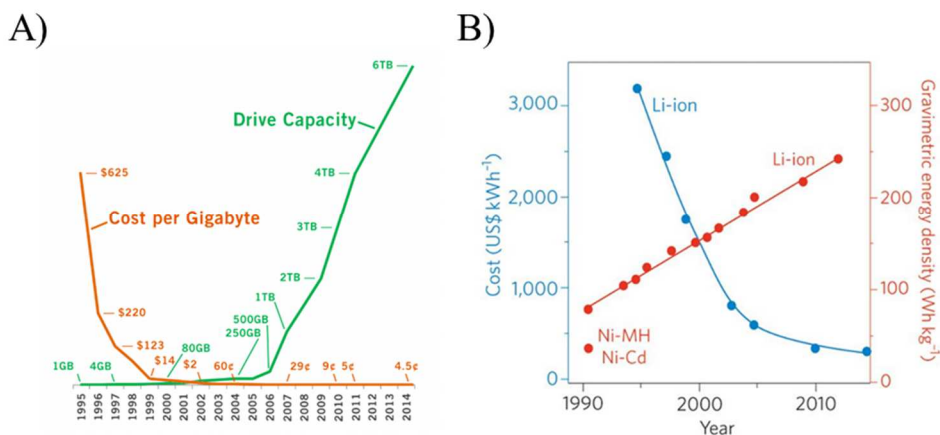
Figure 1.2: The developmental trend over the last several decades of A) transistors cost and capacity and B) Li^+ batteries cost and energy density.[3,4]

A reason for the lack of improvement in Li^+ technology is the stagnation in cell design. In current packaging, the electrodes are enclosed in a pouch or coin cell type design and kept electronically isolated through a use of a separator. (Figure 1.3) To enable ion transport, the cell is soaked in a liquid electrolyte usually consisting of an anhydrous carbonate. The use of liquid electrolytes facilitates high ionic conductivities and excellent electrode wetting, but the limited

physiochemical stability, low ion transference number, and poor safety restrict the cell designs.

Nonaqueous electrolytes are preferred over aqueous systems due to the higher electrochemical stability which allows for design of high voltage cells with high energy densities.[5] Many of these nonaqueous liquids though have low flash points, which increases the flammability risk. The increased safety risk has increasingly come to the public attention with the flammability issues of the Tesla Model S and Samsung Note 7, to name just a few.[6,7]
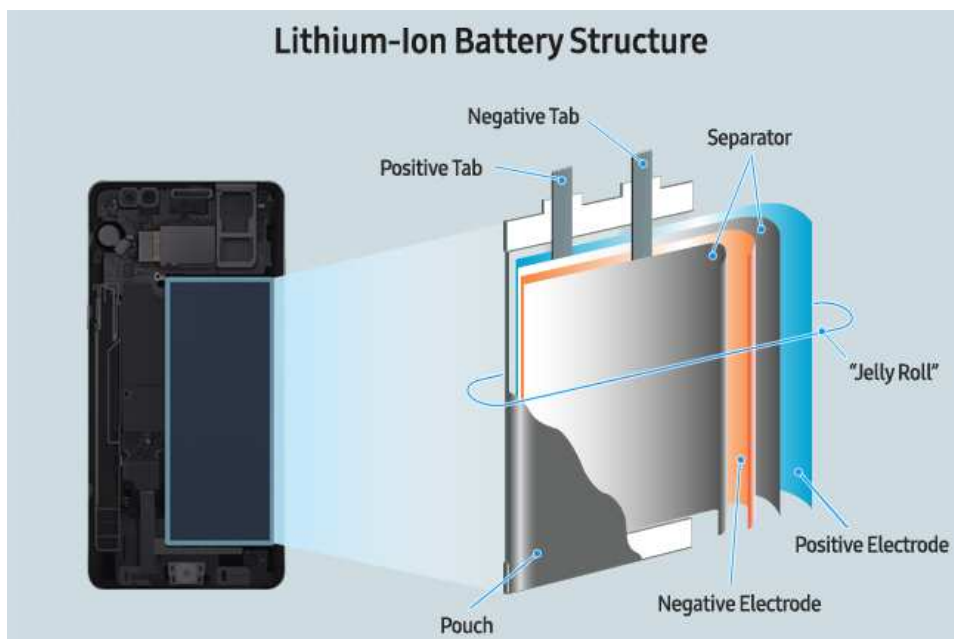
Figure 1.3: Diagram of a Cellphone LIB Structure.

Solid-state electrolytes (SSE), consisting of an ion conducting solid, have been proposed as potential replacements to overcome many of the persistent liquid electrolyte stability problems and as a way to develop new battery chemistries. The conducting solid replaces the liquid, which removes the need for a high volume separator and simplifies the packaging process. While SSE have been explored increasingly over the last several decades, the low ionic conductivity, poor

electrode wetting, and inconclusive electrochemical stability has limited adoption into commercial devices (Figure 1.4).[8] For Li$^+$ battery technology to progress, the issue of replacing liquid electrolytes with SSE must be addressed.
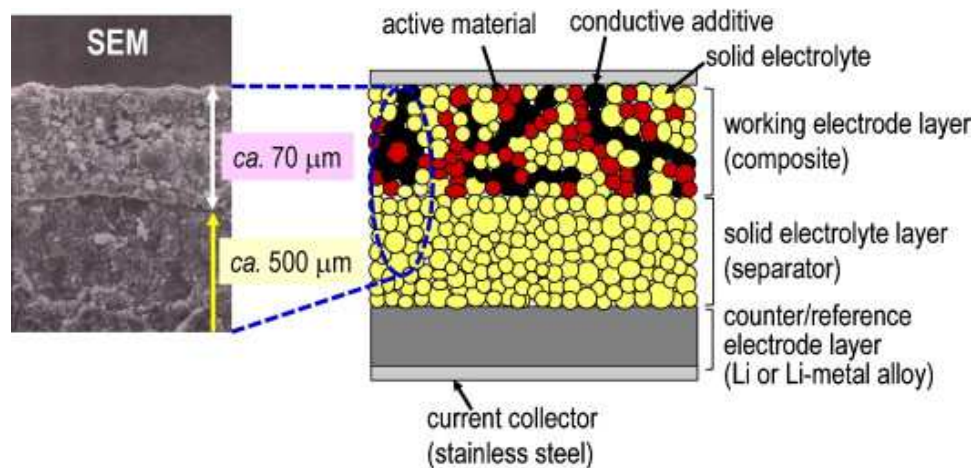
Figure 1.4: Incorporation of a Solid-State Electrolyte into a Li$^+$ Battery.[9]

The work presented in the following chapters center on my work synthesizing an ionogel pseudo-solid electrolyte as a replacement for liquid electrolytes in Li$^+$ ion energy storage devices. The chapters will focus on exploring the functionality of the newly discovered ionogel electrolyte and understanding the interface between the electrolyte and several common electrode materials. Chapter 2 introduces the background of Li$^+$ batteries (LIB) and the various morphologies currently being explored. Chapter 3 presents work on the physiochemical properties of a sub-micron ionogel film (600 nm) and its performance in a LiFePO$_4$ (LFP) full cell. Chapter 4 focuses on understanding the electrode interface with a solution-processed ionogel. The study further explores ways to improve the interface for different electrode materials. Chapter 5 demonstrates the fabrication of an all-solid-state 2.5D battery which is made possible due to the

solution processability of the ionogel electrolyte. Here, high areal energy and power densities were achieved due to scaling in the z-direction.

1.1 References

1.   Atzori, L., Iera, A. & Morabito, G. The Internet of Things: A survey. *Comput. Networks*
      54, 2787–2805 (2010).

2.   Crabtree, G., Kócs, E. & Trahey, L. The energy-storage frontier: Lithium-ion batteries and
      beyond. *MRS Bull.* **40,** 1067–1078 (2015).

3.   Technology Growth Curves. *Ray Bernard Consulting Service* (2015). Available at:
      https://www.go-rbcs.com/articles/tech-growth-curves.

4.   Electric Vehicle Battery: Materials, Cost, Lifespan | Union of Concerned Scientists. *Union
      of Concerned Scientists* (2018). Available at: https://www.ucsusa.org/clean-
      vehicles/electric-vehicles/electric-cars-battery-life-materials-cost#.W9JLVWhKjIU.

5.   Xu, K. Nonaqueous liquid electrolytes for lithium-based rechargeable batteries. *Chem.
      Rev.* **104,** 4303–4417 (2004).

6.   Musk, E. Model S Fire | Tesla. *Tesla Blog* (2013). Available at:
      https://www.tesla.com/blog/model-s-fire.

7.   Galaxy Note7: What We Discovered – Samsung Global Newsroom. *Samsung Newsroom*
      (2017). Available at: https://news.samsung.com/global/infographic-galaxy-note7-what-
      we-discovered.

8.   Manthiram, A., Yu, X. & Wang, S. Lithium battery chemistries enabled by solid-state
      electrolytes. *Nat. Rev. Mater.* **2,** 1–16 (2017).

9.   Tatsumisago, M., Nagao, M. & Hayashi, A. Recent development of sulfide solid

electrolytes and interfacial modification for all-solid-state rechargeable lithium batteries. *J. Asian Ceram. Soc.* **1,** 17–25 (2013).

Chapter 2: Background

2.1 Li⁺ Battery Chemistry

Lithium-ion batteries (LIB) consist of an anode and cathode electronically separated and soaked in a liquid electrolyte. Electrons move between the two electrodes via metallic current collectors connected in an external circuit. The cell can either store energy by moving ions against their thermodynamic gradients (charging) or produce energy by moving the ions down the thermodynamic gradient towards their ground state (discharging). The ions move between the electrodes by means of the liquid electrolyte that is soaked in a separator (Figure 2.1). For LIB, the electrolyte typically consists of an anhydrous, carbonate-based solvent with a lithium salt dissolved in the solution. The separator ensures that a low resistance, internal short circuit is not formed which can lead to electron flow (short).
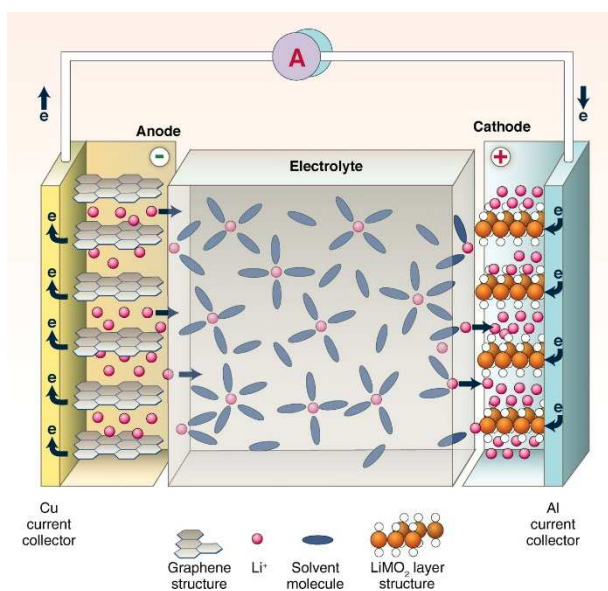
Figure 2.1: Representative Diagram of a LIB.[1]

It is important to distinguish the two conductivity processes that control the electrochemical behavior of LIB electrodes: electronic and ionic transport. Electronic transport consists of the flow of electrons from the redox sites in the electrodes through the current collector to the external circuit. It is important to note that the current collectors need to be chemically inert to the electrolyte to prevent corrosion or breakdown. Good contact between the active material and current collector is required to ensure electron transport. Ideally, mixed conductors are desired to allow for simultaneous ion and electron transport. Many electrode materials though have poor inherent electronic conductivities which can limit the kinetics of the redox reaction, decreasing the available capacity and polarizing the voltage response.[2] Battery engineers typically design around this limitation through the addition of conductive carbon additives. Besides the electronic conductivity, the redox active material should conduct ions readily or have nanoscale architectures to ensure fast intercalation and a homogeneous electrochemical potential (Figure 2.2). Ionic diffusivites for Li^+ electrodes range widely based on the crystal structure (10^{-18} cm s^{-1} for LFP; 10^{-10} for $Li_4Ti_5O_{12}$).[3,4] A low material ionic diffusivity will limit the ability of the cation to reach the redox centers within the cycling conditions, lowering the obtainable capacity. Cell design must take into account the electronic and ionic conductivities of the active material and their effect on cell kinetics.
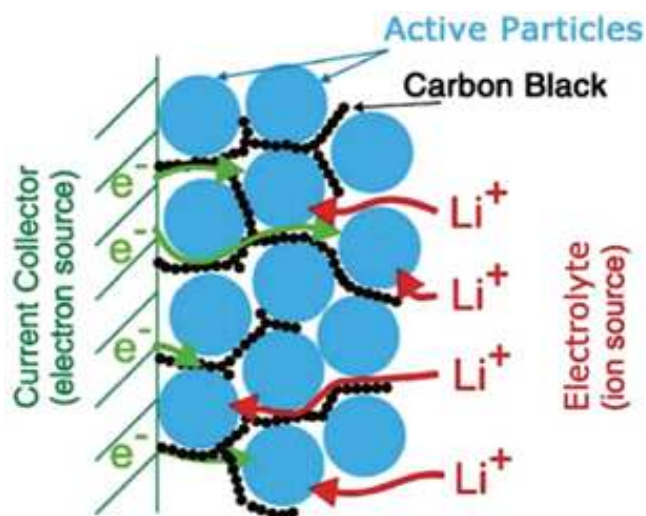
Figure 2.2: Conduction Pathway of Ions and Electrons in a LIB Electrode.

Cell design is central to obtaining a high performance LIB. As mentioned above, a LIB cell consists of electrodes, an electrolyte-soaked separator, and current collectors. In a typical battery, the electrodes consist of active material, carbon additives, and a binder to form a thick film. This essentially is a 3D structure composed of distributed macro and micropores. Designing the tortuosity of pores to decrease the ion interaction rate is important to ensure fast transport.[5] Pore formation is dependent on the interparticle spacing (micro/mesopores) and the solvent evaporation (macropores). The thickness of the film can affect the energy and power density of the cell by increasing the diffusion distance of the ions and electrons. The separator should be as thin as possible but still provide adequate electronic resistance to impede a short circuit. Typically, separators are composed of a tri-layer of polypropylene-polyethylene-polypropylene around 25 μm in thickness with a low tortuosity (Figure 2.3). The current collector is essentially inert mate-

rial, decreasing the gravimetric capacity and increasing the cost of the cell. As such, current collectors are fabricated out of thin sheets of lightweight metals such as copper and aluminum, typically on the thickness of 20 μm.
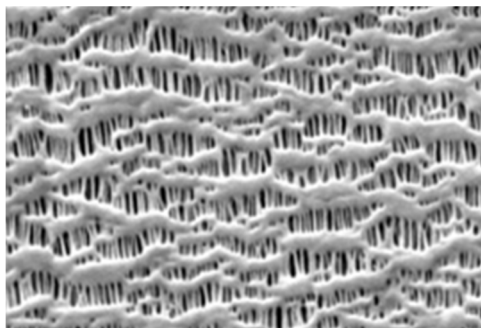
Figure 2.3: Celgard Separator for Nonaqueous Electrolytes.[6]

The energy storage mechanism in LIB can be understood from a thermodynamic viewpoint. In a LIB, a Gibbs free energy of a redox reaction exists from the difference in the chemical potentials of the anode and cathode. This potential exists from the concentration gradient of lithium between the anode and cathode and inherent nature of the host material. The difference can be viewed as the open circuit voltage (OCV) of the cell. On charging with an external voltage, lithium ions are removed from the cathode (oxidation) and driven towards the anode. The removal of lithium ions from the cathode has a simultaneous removal of electrons. The loss of electrons decreases the HOMO, effectively decreasing the cathode's chemical potential (Figure 2.4). The Li^+ and electrons are incorporated into the anode that increases the LUMO and its chemical potential (reduction). The increase in the chemical potential difference during charging can be correlated to the potential measured in the electrochemical cell. The energy (E) stored by the LIB is equal to the charge transferred (Q) and the effective potential (V) between the delithiated cathode and lithiated anode:

$$E = Q*V \tag{2.1}$$

The Gibbs free energy for lithium de/intercalation is theoretically dependent on the material host structure. Cell design, electron and ion solid-state diffusion, and side reactions can polarize the theoretical chemical potential for lithium de/insertion. This polarization can shift the potential outside the stability window of the electrolyte and affect the kinetics of the cell.
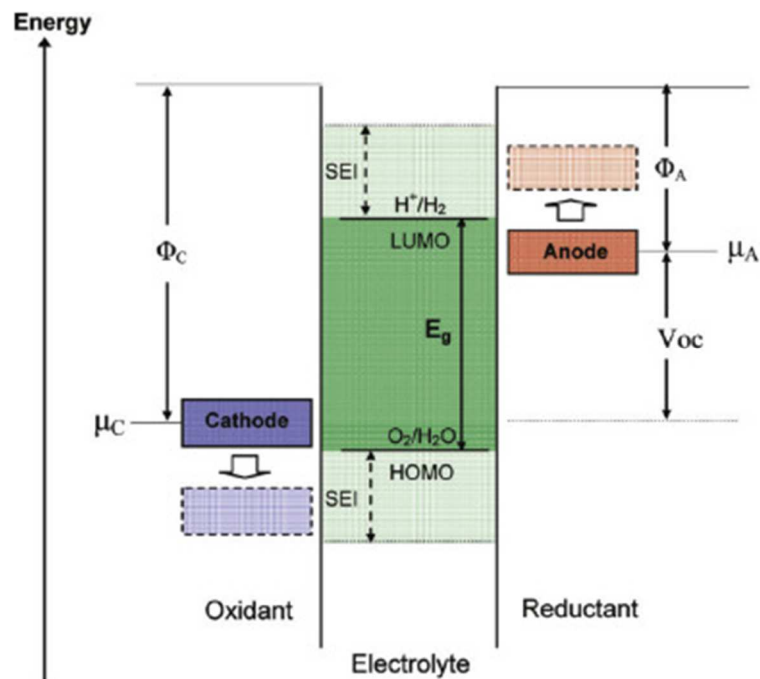
Figure 2.4: Energy Diagram during Cycling of a Battery.[7]

The applied potential difference between the cells determine whether a thermodynamic reaction occurs, but it does not take into account the response time of the reaction. The reaction kinetics are dependent on the several factors related to ion, electron, and mass transport at three scales: intra-material transport, inter-material transport, and cell transport. At the intra-material

level, the kinetics are determined by the mass transport of the redox ion, electron diffusion, and atomic rearrangement inside the active material. The redox ions and electrons must then transfer across the electrode/electrolyte or electrode/electrode interface. To cross this interface, the inherent energy barrier between the two systems must be overcome from an external driving force. Transport of the ions through the electrolyte and electrons between particles at a cell scale will also create bottlenecks that will impede the thermodynamic response of the system. The impedance will require an increasing overpotential that will be dependent on the desired reaction kinetics.

There is a wide range of redox active materials that have been used as the anode and cathode. Materials are chosen based on their electrochemical potential, electronic and ionic conductivity, and cycling stability. These factors will help determine the energy density, power density, and lifetime of the cell. Examples of commonly used electrodes include graphite (0.01V vs Li, 372 mAh g^{-1}), silicon (0.01V vs Li, 4200 mAh g^{-1}), LiCoO$_2$ (LCO, 3.9V vs Li, 140 mAh g^{-1}), and LiFePO$_4$ (LFP, 3.5V vs Li, 176 mAh g^{-1}).[8,9] The choice of which two electrodes will determine the properties of the cell, such as the energy density, power density, and cell lifetime. Redox reactions occur through two mechanisms: intercalation of Li$^+$ into the bulk structure, such as with LCO, LFP, and graphite, or conversion/alloying reactions such as seen with silicon (Figure 2.5). Intercalation redox reactions traditionally occur by an alkali cation diffusing through an open channel in the crystal structure. Some amorphous materials have shown the ability to intercalate ions by octahedral and tetrahedral reorientation, but the lack of long rang order restricts the diffusion distance.[10] The ion travels by hopping between redox active metal centers that produces the charge storage of the electrons.

$$LiFePO_4 \rightarrow FePO_4 + Li^+ + e^- \qquad\qquad (2.2)$$

The cation intercalation causes a phase change which relieves the stress induced from the cation size and charge (volume expansion~5%).[11] The kinetics of intercalation is dependent on the size of the channel, the ion-ligand interaction, the choice of cation, and the thermodynamics of crystal reorientation.
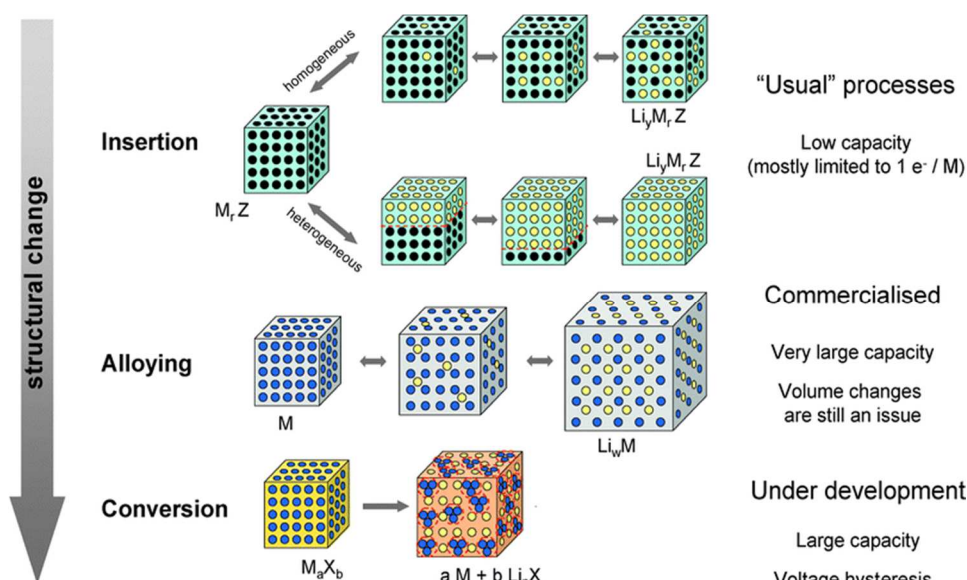
Figure 2.5: Diagram of the Typical Reaction Mechanisms in LIBs.[12]

Conversion and alloying reactions have been explored for various materials including the chalcogenides, group IV elements, and metal oxide (Si, S, Co_3O_4, etc.). Typically, these conversions follow the reaction of a metal oxide or element to form a lithiated metal/compound as seen for the lithium silicon reaction:

$$Si + xLi \rightarrow Li_{15}Si_4 \qquad\qquad (2.3)$$

The conversion reactions allow for the incorporation of a large number of Li$^+$ which leads to high theoretical capacities (4200 mAh g^{-1} for Si), but this also produces large volume expansions (~400% for Si).[13] The expansion can shorten the cell lifetime by causing pulverization of the active material and destruction of the electronic pathway. Typical conversion reactions will lose 75% of the initial capacity over 100 cycles which is significantly higher than seen for intercalation compounds (90% capacity retention over 1000 cycles of LCO/Graphite).[14,15] With conversion reactions, the end lithiation is in a new crystalline or stoichiometric compound. The new compounds create a different reaction pathway for delithiation that causes a large voltage hysteresis. The hysteresis can create issues when designing the cell electronics and lead to capacity loss. Due to the thermodynamic limitations and sluggishness of phase transformation, conversion reactions typically have slow kinetics that limit usefulness in commercial cells. Nanostructuring of conversion materials has been explored to avoid the volume expansion and kinetic issues with varying success.[16] Currently, conversion materials have only been readily studied as anode materials. Sulfur has been used as a cathode but the low redox voltage and shuttle issues of polysulfides have limited the use of sulfur in commercial devices.[17]

2.2 LIB Electrolyte: Liquid vs Solid-State

Liquid electrolytes (a solution containing dissolved salts) have historically been used in energy storage technologies due to the high ionic conductivity, excellent wetting of the electrode, and ease of synthesis. Aqueous solvents are most commonly used in battery electrolytes because of their low cost, low toxicity, and low viscosity. Common examples of aqueous-based batteries include the lead acid battery (car batteries) and primary alkaline batteries (AA batteries) (Figure

2.6). The main limitation of aqueous batteries is the narrow electrochemical stability window, due to electrolysis, which restricts the potential energy density. This window can be shifted by adjusting the pH of the electrolyte, but it is still restricted to 1.23V. While the electrochemical window is limited, aqueous based electrolytes have high flash points, which ensures that the cell is non-flammable.
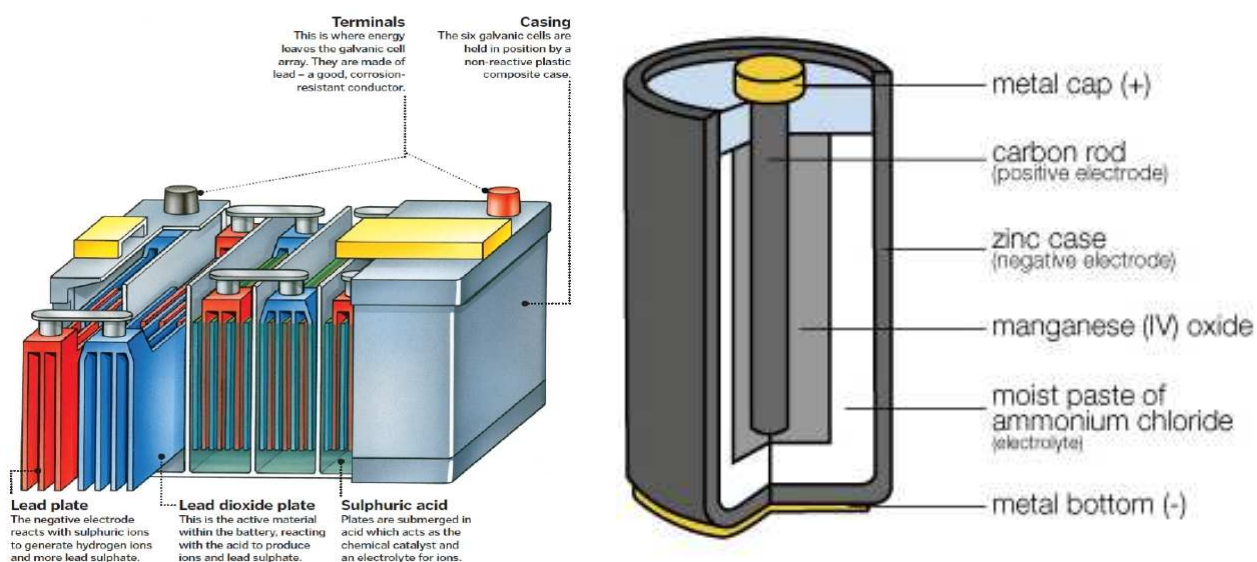
Figure 2.6: General schematics for common household batteries: A) a lead-acid battery B) an alkaline battery.

Non-aqueous (aprotic) electrolytes recently have been used as alternatives for aqueous electrolytes. Unlike aqueous electrolytes, many nonaqueous electrolytes have high electrochemical stability that allows for design of high voltage cells. The high voltage increases the energy density of the cell and possible usable materials. Many different polar solvents have been used in LIB varying from carbonates, sulfonyls, ethers, and nitriles.[18] These solvents can be combined to

tune the desired physiochemical properties. An ideal solvent would have a 1) high dielectric constant to dissolve the salt, 2) low viscosity to ensure facile ion transport, 3) be inert electrochemically and physiochemically, 4) maintain a liquid state over the a wide thermal range, 5) and have low toxicity, a high flash point, and be inexpensive. Due to the strong reducing power of LIB anodes and oxidizing power of cathodes, most protonated solvents are excluded because of their instability outside a 2-4V range.[18] It is important to note that introduction of organics leads to the formation of a solid electrolyte interface (SEI).

Carbonate based electrolytes have been the most widely used nonaqueous solvent because of their formation of a stable SEI on graphite. Graphite is the most commonly used LIB anode due to its low voltage and high capacity. The formation of a stable interface layer is central to ensure long-term cell cycling. While SEI formation is not fully understood for carbonate electrolytes, it is believed that the ethylene carbonate ring opens to form a polymerizable linear chain that can precipitate onto the electrode surface to form a dense coating.[19] (Figure 2.7) The lithium salt plays a large role in the formation of the SEI with the anion commonly decomposing to form inorganic components in the SEI layers.[20] Formation of a SEI that is 1) ionically conductive, 2) electronically insulating, 3) dense and uniform, and 4) insoluble in the electrolyte is paramount for a usable cell.[21] In LIB, SEI formers such as vinylene carbonate or fluoroethylene carbonate have been added to improve the uniformity and insolubility of the SEI. These additives are known polymerizable ring-opening molecules that increase the networking ability of the decomposed carbonates.
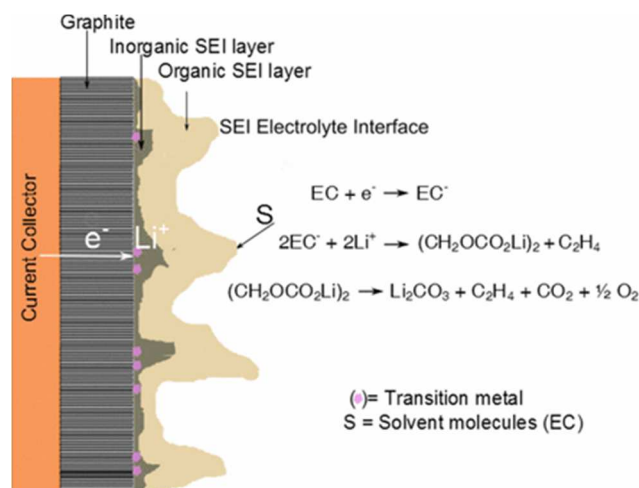
Figure 2.7: SEI formation from a Li⁺ salt Containing EC electrolyte on Graphite.[22]

While aprotic electrolytes have a wider electrochemical window, breakdown of the commonly used carbonate electrolytes starts around 4.3V vs Li, which has limited design of higher energy density cathodes. These carbonate electrolytes typically have a low flash point which has increased the flammability risk of commercial devices. The issue of high flammability of LIB has been seen in the last several years with the Samsung Note 7 and Tesla Model S as mentioned in Chapter 1. This flammability risk has led to an increased interest into alternative electrolytes such as solid-state electrolytes (SSE) and ionic liquid electrolytes (ILE) with safer chemistries.

SSE have been explored as replacements for liquid electrolytes since the 1970's.[23] SSE can be broken up into two categories determined by their backbone: inorganic and organic. Inorganic SSE typically consist of a crystalline solid where a cation hops through the structure either between Schottky or Frenkel defects. Concentration gradients and electric fields provide the thermodynamic driving force for the ion hopping.[24] High ionic conductivities can be obtained from structures with a high defect concentration or low migration barrier. Examples of superionic conductors include the NASICON and LISICON systems such as $Li_{10}GeP_2S_{12}$ or $Li_7La_3Zr_2O_{12}$

which have ionic conductivities on par with liquid electrolytes (10^{-3}-10^{-2} S cm^{-1}).[25,26] Inorganic SSE were originally attractive because of their nonflammability, perceived ability to suppress lithium dendrites, and lithium transfer number close to unity. While initially thought to be able to suppress lithium dendrites due to their high shear modulus, recent studies have shown that dendrites can still grow between grain boundaries and other inner surfaces, propagating to form a cell short.[27] Further study of inorganic SSE have identified several fundamental issues that have limited application. It has been shown that many of these superionic electrolytes are thermodynamically unstable to commonly used Li$^+$ anodes and cathodes, creating highly resistive interfaces.[28] Further, many of these decomposed products are electronically conductive leading to continued decomposition and SEI growth.[29] (Figure 2.8) Processing of the inorganic electrolytes has also proven troublesome because high temperatures and pressures are needed to obtain a sintered pellet with good interparticle contact. The solidity of the particles leads to poor contact between the active material and SSE which creates a highly resistive bottleneck for Li$^+$ diffusion.[30]
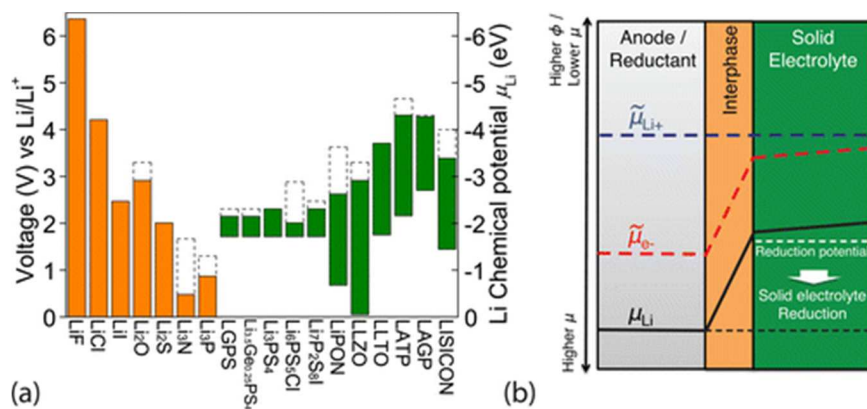
Figure 2.8: Solid Electrolyte Interface Stability: A) Thermodynamic modeling of the electrochemical stability against Li metal. B) Diagram of the electron potentials at the anode/SSE interface.[31]

Organic SSE typically consist of a lithium salt dissolved in a polymer matrix. Several matrixes have been used including poly(ethylene oxide) (PEO), poly(methmethylacrylate) (PMMA), poly(acrylonitrile) (PAN), and poly(vinylidene fluoride) (PVDF).[24] Li$^+$ has been hypothesized to move through the polymer matrix by hopping between polar groups or by segmental motion of polymer chains when the system is around the glass transition temperature.[32] Ionic conductivities range from 10^{-6}-10^{-4} S cm^{-1}, which have limited cells achievable power densities. This low conductivity originates from the high activation energy for ion hopping because of the large distance between hopping centers. Besides the ionic conductivity, organic SSE typically have limited thermal stability and a low oxidation voltage. Though limited, organic SSE have significantly better wetting abilities than inorganic SSE and are easily processed into flexible, large-area membranes.[24] For these reasons, and their stability against lithium metal, organic SSE have been commercialized for low power applications (Lithium Polymer Battery).

Besides SSE, ionic liquids have been explored as an alternative to aqueous and non-aqueous electrolytes for LIB. Ionic liquids are a unique class of liquids composed of room temperature molten salts. Due to only being composed of bulky ions, the liquids have high thermal and electrochemical stability, are non-flammable, have a high ionic conductivity, and have negligible vapor pressure. Ionic liquid properties are highly tunable based on the choice of cation and anion. This can be seen by the increase of ionic conductivity by using an [EMIM]$^+$ cation over [BMIM]$^+$.[33,34] Currently, ionic liquids are used in a multitude of applications besides electrochemical energy storage, such as electrodeposition, actuators, and ionothermal synthesis.[35-37] ILE have been successfully used in LIB systems with no detrimental effect on the cell performance.[38,39] While having many beneficial properties, ionic liquids have been limited by the high

cost for synthesis and low Li$^+$ transfer number. The cost has been progressively decreasing which has led to an increasing number of publications using ionic liquids for LIB and other systems.[40-42]

While ionic liquids have several promising properties, the liquid state complicates packaging and increases the weight and volume of the cell due to the need for a separator. As such, trapping ionic liquids inside an organic or inorganic matrix has been explored as a means to fabricate pseudo-solid electrolytes (Ionogels). Ionogels are most commonly fabricated through polymerizing a monomer around the liquid or by incorporating the liquid into an inorganic sol-gel process. Entrapment using a silica sol-gel synthesis has been commonly used for LIB because of the high physiochemical stability of the silica matrix and good understanding of the gelation mechanism. During gelation, the silica forms around the ionic liquid which creates a highly porous network that allows facile ion transport through the solid.[43] Due to the negligible vapor pressure, the ionic liquid remains in the structure giving the ionogel comparable properties to the neat ionic liquid. Ionogels have been explored for various applications, including electrochromic, thermal management, and actuator devices.[44] Adjusting the matrix or ionic liquid formulation allows for the ionogel properties to be tuned to fit the desired application. Ionogels have already been fabricated in LIB as bulk gels,[45,46] but there is a dearth of work exploring ionogels in novel geometries and applications.

2.3 Battery Architectures

LIB architectures can be grouped into two categories: 2D (planar) or 3D electrodes. Planar electrodes are the most common geometry used in commercial and laboratory devices due to the easy of fabrication and uniform current density during cycling. Planar electrodes typically

consists of a slurry, composed of active material, binder, and conductive additives, cast onto a current collector. Dense films deposited through sputtering or other line-of-sight techniques have also been commonly fabricated for microelectronic applications. Slurry electrodes are typically deposited using a roll-to-roll process (R2R) to obtain thick, uniform films (Figure 2.9). Films typically range from 50-100 µm with weight loadings of 10-20 mg cm^{-2}. Controlling the porosity and tortuosity during deposition is central to ensuring facile electrolyte access. High active material loadings are desired to achieve the highest volumetric capacity, with 90-95% values commonly obtained for commercial electrodes.
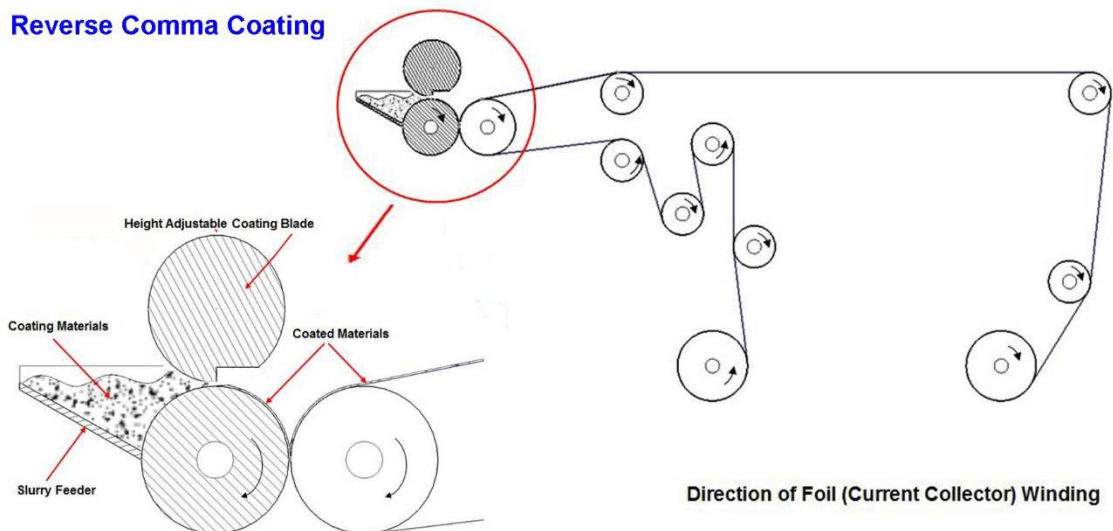
Figure 2.9: Roll-2-Roll setup used in LIB electrode fabrication.

Dense planar films are traditionally used in microbatteries where direct deposition on a structure is required. Examples of microbattery applications include on-chip devices, microrobotics, and the internet of things (IoT). As mentioned, dense planar electrodes are typically deposited through line-of-site techniques that lay down micron-thick films of singular composition.

The deposition thickness limit is determined by the material's ionic and electronic conductivity. If the films are made too thick, the active material will not be completely utilized during typical cycling conditions.[47] SSE are commonly used to simplify the packaging process and to better collaborate with the microelectronic fabrication process. Sputtering targets have been fabricated with the same anodes and cathodes used in slurry electrodes for dense films. $LiCoO_2$ has been one of the most commonly used cathodes for high areal capacity microbatteries because of its high electronic and ionic conductivity.

3D batteries have recently become of interest in the battery community because of their ability to decrease the ionic diffusion distance for high areal loading cells. 3D batteries consist of an anode and cathode that are patterned or templated into a 3D structure (Figure 2.10). By designing the cell in the z direction, the electrodes can be fabricated to minimize the distance between the anode and cathode. Liquid electrolytes and conformal solid electrolytes have been used as electrolytes for these devices. Conformal electrolytes have been deposited from photolithography, ALD, and iCVD techniques, but they have low ionic conductivities.[32,48,49] Multiple fabrication routes have been used for 3D electrodes, ranging from templating to 3D printing.[50-52] While several processes have been used to make 3D batteries, the design is limited by the fabrication process. It is common for voids or shorts to form in the cell due to inadequate electrode or electrolyte filling and from the short electrode-electrode distance. As the majority of conformal solid electrolytes have low ionic conductivities, most 3D LIB have used liquid electrolytes which has restricted commercialization.[32,53]
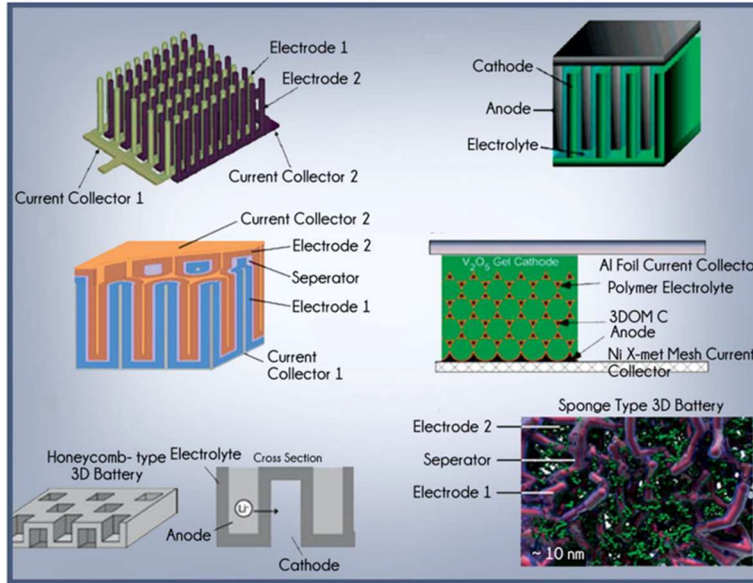
Figure 2.10: Examples of 3D architectures.[54]

2.4 References

1.   Tarascon, J. M. & Armand, M. Issues and challenges facing rechargeable lithium batteries. *Nature* **414,** 359–367 (2001).

2.   Nitta, N., Wu, F., Lee, J. T. & Yushin, G. Li-ion battery materials: Present and future. *Mater. Today* **18,** 252–264 (2015).

3.   Scrosati, B. & Garche, J. Lithium batteries: Status, prospects and future. *J. Power Sources* **195,** 2419–2430 (2010).

4.   Xu, J. J., Kinser, A. J., Owens, B. B. & Smyrl, W. H. Amorphous Manganese Dioxide: A High Capacity Lithium Intercalation Host. *Electrochemical and Solid-State Letters* **1,** (1998).

5.   Julien, C. M., Mauger, A., Zaghib, K. & Groult, H. Comparative Issues of Cathode Materials for Li-Ion Batteries. *Inorganics* **2,** 132–154 (2014).

6.   Yang, M. & Hou, J. Membranes in lithium ion batteries. *Membranes.* **2,** 367–83 (2012).

7.   Goodenough, J. B. & Kim, Y. Challenges for Rechargeable Li Batteries. *Chem. Mater* **22,** 587 (2010).

8.   Nitta, N., Wu, F., Lee, J. T. & Yushin, G. Li-ion battery materials: Present and future. *Mater. Today* **18,** 252–264 (2015).

9.   Scrosati, B. & Garche, J. Lithium batteries: Status, prospects and future. *J. Power Sources* **195,** 2419–2430 (2010).

10.   Xu, J. J., Kinser, A. J., Owens, B. B. & Smyrl, W. H. Amorphous Manganese Dioxide: A

High Capacity Lithium Intercalation Host. *Electrochemical and Solid-State Letters* **1,** (1998).

11.   Julien, C. M., Mauger, A., Zaghib, K. & Groult, H. Comparative Issues of Cathode Materials for Li-Ion Batteries. *Inorganics* **2,** 132–154 (2014).

12.   Palacin, M. R. Recent advances in rechargeable battery materials: a chemist's perspective. *Chem. Soc. Rev.* **38,** 2565–2575 (2009).

13.   Jerliu, B. *et al.* Volume Expansion during Lithiation of Amorphous Silicon Thin Film Electrodes Studied by In-Operando Neutron Reflectometry. *J. Phys. Chem. C* **118,** 9395–9399 (2014).

14.   Piper, D. M. *et al.* Stable silicon-ionic liquid interface for next-generation lithium-ion batteries. *Nat Commun* **6,** 1–10 (2015).

15.   Guan, T. *et al.* Degradation mechanism of $LiCoO_2$/mesocarbon microbeads battery based on accelerated aging tests. *J. Power Sources* **268,** 816–823 (2014).

16.   Shao, D., Tang, D., Mai, Y. & Zhang, L. Nanostructured silicon/porous carbon spherical composite as a high capacity anode for Li-ion batteries. *J. Mater. Chem. A* **1,** 15068 (2013).

17.   Zhang, S. S. Liquid electrolyte lithium/sulfur battery: Fundamental chemistry, problems, and solutions. *J. Power Sources* **231,** 153–162 (2013).

18.   Xu, K. Nonaqueous liquid electrolytes for lithium-based rechargeable batteries. *Chem. Rev.* **104,** 4303–4417 (2004).

19.	An, S. J. *et al.* The state of understanding of the lithium-ion-battery graphite solid electrolyte interphase (SEI) and its relationship to formation cycling. *Carbon.* **105,** 52–76 (2016).

20.	Wang, A., Kadam, S., Li, H., Shi, S. & Qi, Y. Review on modeling of the anode solid electrolyte interphase (SEI) for lithium-ion batteries. *npj Comput. Mater.* **4,** 15 (2018).

21.	Peled, E. & Menkin, S. Review—SEI: Past, Present and Future. *J. Electrochem. Soc.* **164,** A1703–A1719 (2017).

22.	Joshi, T., Eom, K., Yushin, G. & Fuller, T. F. Effects of Dissolved Transition Metals on the Electrochemical Performance and SEI Growth in Lithium-Ion Batteries. *J. Electrochem. Soc.* **161,** 1915–1921 (2014).

23.	Farrington, G. C. & Briant, J. L. Fast ionic transport in solids. *Science* **204,** 1371–1379 (1979).

24.	Manthiram, A., Yu, X. & Wang, S. Lithium battery chemistries enabled by solid-state electrolytes. *Nat. Rev. Mater.* **2,** 1–16 (2017).

25.	Kamaya, N. *et al.* A lithium superionic conductor. *Nat. Mater.* **10,** 682–686 (2011).

26.	Geiger, C. A. *et al.* Crystal chemistry and stability of "$Li_7La_3Zr_2O_{12}$" garnet: A fast lithium-ion conductor. *Inorg. Chem.* **50,** 1089–1097 (2011).

27.	Liang, X. *et al.* A facile surface chemistry route to a stabilized lithium metal anode. *Nat. Energy* **6,** 17119 (2017).

28.	Zhu, Y., He, X. & Mo, Y. First principles study on electrochemical and chemical stability

of solid electrolyte–electrode interfaces in all-solid-state Li-ion batteries. *J. Mater. Chem. A* **4,** 3253–3266 (2016).

29.   Wenzel, S. *et al.* Direct Observation of the Interfacial Instability of the Fast Ionic Conductor $Li_{10}GeP_2S_{12}$ at the Lithium Metal Anode. *Chem. Mater.* **28,** 2400–2407 (2016).

30.   Han, F., Zhu, Y., He, X., Mo, Y. & Wang, C. Electrochemical Stability of $Li_{10}GeP_2S_{12}$ and $Li_7La_3Zr_2O_{12}$ Solid Electrolytes. *Adv. Energy Mater.* **6,** 1501590 (2016).

31.   Zhu, Y., He, X. & Mo, Y. Origin of Outstanding Stability in the Lithium Solid Electrolyte Materials : Insights from Thermodynamic Analyses Based on First- Principles Calculations. *ACS Appl. Mater. Interfaces* **7,** 23685–23693 (2015).

32.   Choi, C. S. *et al.* Synthesis and Properties of a Photopatternable Lithium-Ion Conducting Solid Electrolyte. *Adv. Mater.* **30,** 1703772 (2018).

33.   Galiński, M., Lewandowski, A. & Stepniak, I. Ionic liquids as electrolytes. *Electrochim. Acta* **51,** 5567–5580 (2006).

34.   Ghandi, K. A Review of Ionic Liquids, Their Limits and Applications. *Green Sustain. Chem.* **4,** 44–53 (2014).

35.   Endres, F., MacFarlane, D. & Abbott, A. *Electrodeposition from Ionic Liquids*. (WILEY-VCH Verlag GmbH & Co, 2008).

36.   Morris, R. E. Ionothermal synthesis--ionic liquids as functional solvents in the preparation of crystalline materials. *Chem. Commun.* 2990–2998 (2009).

37.   Ghamsari, A. K., Jin, Y., Zegeye, E. & Woldesenbet, E. Bucky gel actuator displacement:

experiment and model. *Smart Mater. Struct.* **22,** 025034 (2013).

38.   Kim, J. K., Matic, A., Ahn, J. H. & Jacobsson, P. An imidazolium based ionic liquid
       electrolyte for lithium batteries. *J. Power Sources* **195,** 7639–7643 (2010).

39.   Reale, P., Fernicola, A. & Scrosati, B. Compatibility of the $Py_{24}TFSI$-LiTFSI ionic liquid
       solution with $Li_4Ti_5O_{12}$ and $LiFePO_4$ lithium ion battery electrodes. *J. Power Sources* **194,**
       182–189 (2009).

40.   Lewandowski, A. & Świderska-Mocek, A. Ionic liquids as electrolytes for Li-ion
       batteries-An overview of electrochemical studies. *J. Power Sources* **194,** 601–609 (2009).

41.   Liu, C. *et al.* Ionic liquid electrolyte of lithium bis(fluorosulfonyl)imide/N-methyl-N-
       propylpiperidinium bis(fluorosulfonyl)imide for Li/natural graphite cells: Effect of
       concentration of lithium salt on the physicochemical and electrochemical properties.
       Electrochim. Acta **149,** 370–385 (2014).

42.   Lee, J. S., Bae, J. Y., Lee, H., Quan, N. D. & Kim, H. S. H. Ionic liquids as electrolytes
       for Li ion batteries. *Journal of Industrial and Engineering Chemistry* **10,** 1086–1089
       (2004).

43.   Echelmeyer, T., Meyer, H. W. & Van Wullen, L. Novel ternary composite electrolytes: Li
       ion conducting ionic liquids in silica glass. *Chem. Mater.* **21,** 2280–2285 (2009).

44.   Le Bideau, J., Viau, L. & Vioux, A. Ionogels, ionic liquid based hybrid materials. *Chem
       Soc Rev* **40,** 907–925 (2011).

45.   Tan, G. *et al.* Solid-State Li-Ion Batteries Using Fast, Stable, Glassy Nanocomposite

Electrolytes for Good Safety and Long Cycle-Life. *Nano Lett.* **16,** 1960–1968 (2016).

46.   Delannoy, P. E. *et al.* Toward fast and cost-effective ink-jet printing of solid electrolyte for lithium microbatteries. *J. Power Sources* **274,** 1085–1090 (2015).

47.   L Notten, P. H., M Oudenhoven, J. F. & Baggetto, L. All-Solid-State Lithium-Ion Microbatteries: A Review of Various Three-Dimensional Concepts. *Adv. Energy Mater* **1,** 10–33 (2011).

48.   Pearse, A. J. *et al.* Nanoscale Solid State Batteries Enabled by Thermal Atomic Layer Deposition of a Lithium Polyphosphazene Solid State Electrolyte. *Chem. Mater.* **29,** 3740–3753 (2017).

49.   Chen, N. *et al.* Nanoscale, conformal polysiloxane thin film electrolytes for three-dimensional battery architectures. *Mater. Horizons* **2,** 309-314 (2015).

50.   Sun, K. *et al.* 3D Printing of Interdigitated Li-Ion Microbattery Architectures. *Adv. Mater.* **25,** 4539–4543 (2013).

51.   Ning, H. *et al.* Holographic patterning of high-performance on-chip 3D lithium-ion microbatteries. *Proc. Natl. Acad. Sci.* **112,** 6573–8 (2015).

52.   Hur, J. I., Smith, L. C. & Dunn, B. High Areal Energy Density 3D Lithium-Ion Microbatteries. *Joule* **2,** 1187–1201 (2018).

53.   Chen, N. *et al.* Nanoscale, conformal polysiloxane thin film electrolytes for three-dimensional battery architectures. *Mater. Horizons* **2,** 309–314 (2015).

54.   Arthur, T. S. *et al.* Three-dimensional electrodes and battery architectures. *MRS Bull.* **36,** 523–531 (2011).

Chapter 3: Patternable, Solution Processed Ionogels for Thin Film Lithium-Ion Electrolytes

Ionogels have recently attracted attention as pseudo-solid state electrolytes based on their ability to confine an ionic liquid electrolyte within the mesoporous network of a sol-gel derived inorganic matrix. In this chapter, we report on the development of two important capabilities for ionogels. In one case, we incorporated spin coated, 600 nm Li$^+$ conducting ionogel films in electrochemical cells of LiFePO$_4$/ionogel/Li. A key feature in this work is the ability to have the sol thoroughly penetrate the LiFePO$_4$ electrode prior to gelation. Devices operating at C/2 achieved capacities of 125 mAh g^{-1} for some 150 cycles with minimal capacity loss. In the second case, we developed a UV crosslinking synthesis method and demonstrated photo-patterning of the ionogel. The realization of a photo-patterned pseudo-solid state electrolyte increases the versatility of ionogels and potentially enables new fabrication routes for electrochemical device architectures.

3.1 Introduction

The recent interest in the "internet of things" has led to an increasing need for smaller and more geometrically complex electronics.[1] While advances in electronic device technology has enabled substantial progress in design complexity, energy storage has lagged behind. Current planar battery designs are not well suited for adoption into these systems due to their low areal capacity and limited configurations. In addition, the current use of liquid electrolytes adds undue safety concerns because of their flammability. From a cost perspective, the need for a physical separator and packaging complications associated with liquid cells impedes development.[2] To

overcome these restraints, solid-state electrolytes have been studied extensively as a potential replacement.

Solid electrolytes such as lithium phosphorous oxy-nitride (LiPON), lithium aluminum titanium phosphate (LTAP), and several garnet-based systems have been incorporated in thin film solid-state Li^+ batteries.[3,4] For the most part, these electrolytes are limited by either low ionic conductivity, processing restrictions, or poor electrode/electrolyte interfaces. Several common processing techniques, such as physical vapor deposition (PVD) or atomic layer deposition (ALD), are costly and time intensive, ultimately hindering their use for commercial applications.[5] Moreover, these processing routes often require elevated temperatures to achieve the proper phase, leading to interface irregularities which increase the charge transfer resistance.[6] For these reasons, there is considerable interest in finding new processing routes and materials approaches which overcome the shortcomings associated with the current generation of thin film solid electrolytes.

The present chapter describes the synthesis and properties of thin films of a pseudo-solid state electrolyte based on the encapsulation of ionic liquid in an inorganic matrix. The synthesis of materials by the sol–gel process generally involves the use of metal alkoxides, which undergo hydrolysis and condensation polymerization. The sol–gel process can generally be divided into stages: forming a solution, gelation, aging and drying. In the preparation of silica at room temperature, an appropriate alkoxysilane precursor is mixed with water and a mutual solvent, such as ethanol or methanol, to form a solution. Hydrolysis leads to the formation of silanol groups, Si–OH, which react further to form Si–O–Si moieties. The resulting sol consists of colloidal oxide particles suspended in the solvent. The formation of a stable sol is critical in forming materials

from the liquid phase, such as in the spin coating of thin films as detailed in the present study. As the hydrolysis and condensation polymerization reactions continue, viscosity increases until the solution ceases to flow. This sol–gel transition is irreversible, and at this stage, the one-phase liquid is transformed to a two-phase system. The gel consists of a network of amorphous primary particles of variable size (5–10 nm or smaller) with an interstitial liquid phase that fills the pores. During the drying stage, the volatile liquid phase is removed under ambient conditions (xerogels) or supercritically (aerogels), producing materials where porosity depends upon the processing conditions. The distinctive feature in the present work is that an ionic liquid is used as the solvent for the precursors and, because of its very low vapor pressure, solvent evaporation does not occur. That is, with the exception of the small quantity of volatile species produced from hydrolysis and condensation, there is no solvent removal and no pore formation occurs. Instead, the ionic liquid fills the continuous mesoporous matrix produced by the sol-gel process. The resulting material, termed an ionogel, is a dense, macroscopically rigid material that consists of two interpenetrating phases; the ionic liquid and the mesoporous inorganic solid whose pores trap the ionic liquid by capillary forces. Ionogels have been designed to exhibit a number of properties including biosensing, through enzyme entrapment, and actuation through ion or photo stimuli.[7-10] These materials have also been used as electrolytes for lithium-ion batteries, capacitors, and electrochromics. In most of these cases, the ionogel was used as a bulk electrolyte (~ 100's μm thick) as compared to the thin film electrolyte reported here (~ 1 micron).

Processing a solid-state electrolyte as a sol has certain advantages in fabricating electrochemical materials. A low viscosity sol has the ability to penetrate uniformly into porous struc-

tures. This is an important consideration in battery electrodes where the pore network in the electrode material enables the ionically conducting electrolyte to achieve good wetting of the electrode material and to serve as the reservoir of ions for the electrochemical reactions occurring within the electrode. The ability of the electrolyte to access the entirety of the electrode helps ensure both high capacity and rate capability[11] Low temperature processing is also beneficial as it helps limit chemical interaction and decrease the charge transfer resistance. Earlier research by Le Bideau, et al., showed the ability of an ionogel to penetrate into a cast electrode without generating interfacial reactions.[12] By separating solution processing from solidification, there is the opportunity to better integrate the electrolyte into nontraditional geometries, such as hierarchical electrode structures, as solidification occurs after complete wetting of the structure has transpired.

Solution processed pseudo-solid state electrolytes have the potential to replace liquid electrolytes in planar batteries. However, possible applications for a number of device opportunities may be limited due to the lack of spatial control. Patterning through photolithography has the ability to achieve the spatial control of electrolyte processing. Photopatterning has been used extensively in the semiconductor industry for rapidly fabricating low cost, high resolution structures, but it has not been readily adopted in the battery community.[13] UV induced polymerization conventionally occurs by generating free radicals or cations upon irradiation to selectively pattern the desired structure. In free radical controlled syntheses, the radical will attack a carbon double bond allowing the end carbon to undergo additive polymerization to other monomers.[14] Cationic polymerization typically follows the localized control of pH, leading to cleavage of the cation under UV illumination, forming cationic radicals as observed with the onium salts. These

radicals react with solvent or impurities to produce protons that interact with the anion to form protonic acids.[16,17] Studies of the polymerization of siloxane films using onium-based salts indicate their potential for fabricating ionogel films.[17,18] Previous publications have also shown that an organic matrix ionogel can be formed through UV polymerization.[19,20]

In the present chapter we report two important capabilities offered by ionogels. In one case, we demonstrate the synthesis of high quality Li^+ conducting ionogel thin films of < 1 μm, substantially thinner than previous work. We incorporate these solid electrolyte thin films in a Li metal battery structure. A key feature in this work is the ability to control the sol state so that it thoroughly penetrates the porous $LiFePO_4$ (LFP) electrode prior to gelation, leading to higher power density than previously reported cells with ionogel electrolyte. In the second case, we demonstrate the photo-patterning of a Li^+ conducting ionogel. The addition of this novel functionality underscores the flexibility of ionogel materials and their potential use in thin film solid-state batteries.

3.2 Experimental Procedures

3.2.1 Sol-Gel Processing

Tetramethylorthosilicate (TMOS, 99+%, Sigma Aldrich), triethylvinylorthosilcate (VTEOS, 97%, Sigma Aldrich), formic acid (Puram, Fluka Analytical), and cyclohexane (99+%, Sigma Aldrich) were obtained for the sol gel reaction. Lithium bis(trifluoromethanesulfonyl)imide (LiTFSI, 99.95%, Sigma Aldrich), 1-butyl-3-methylimidazolium bis(trifluoromethanesul-

fonyl)imide ([BMIM] [TFSI], 99.5%, Solvionic), and vinylene carbonate (VC, 99.5%, Sigma Aldrich) were obtained for the ionic liquid electrolyte. Methanol (99.8% anhydrous, Sigma Aldrich), acetone (ACS quality, Fischer Scientific), N-hydroxynaphthalimide triflate (NHT, >99% electronic grade, Sigma Aldrich), diphenyliondinium hexafluorophosphate (DPI, 98%, Sigma Aldrich), and methyl methacrylate (99% <30ppm MEHQ as inhibitor, Sigma Aldrich) were obtained for the UV exposed ionogels.

0.5M LiTFSI BMIM TFSI ionic liquid electrolyte (ILE) was prepared inside an Ar filled, 1ppm H_2O glove box. The solution was then removed and degassed using a vacuum oven and bubbled with Ar at 150°C before storing inside the glovebox. 2 wt % of VC was added to aid SEI formation.

For the TMOS-VTEOS gel (referred to now as gel 1), equal volumetric amounts of TMOS, VTEOS, and formic acid were sonicated until mixed. A 3/3/1 volumetric ratio of the silica precursor solution(TMOS,VTEOS, and formic acid) /ILE/cyclohexane was prepared and aged for 4 hours at -20°C before spinning (1.4/1/5.6/2.1/2.1 mole ratio). VTEOS was added to improve the gel's structural stability. Spin coating was conducted using a Headway Research Inc. instrument (PWM32). The sol mixture was spun at 4000 rpm for 15 seconds onto cast cathodes or Si wafers. Bulk ionogels were formed by drop casting gel 1 with the same aging parameters for characterization tests. All gels were further aged at room temperature for 1 day and then heated at 110°C for 2 hours.

UV processed ionogels were synthesized by mixing TMOS/ILE/MeOH (gel 2) in a volumetric ratio of 4/4/1 (4/2/3.6 mole ratio). To this was added 0.8 wt % DPI and stirred overnight.

Gel 2 was spun on O_2 plasma-cleaned cathodes at 4000 rpm for 15 seconds. The spun sol was aged for 4 hours in ambient conditions after UV exposure of 180 mJ cm^{-2} using a 254 nm Spec-tronics Corporation XL-1000 UV crosslinker. The UV exposed film was dried in an 110°C oven overnight to complete the reaction.

The sol for the UV photo-patterned ionogels were made by mixing TMOS/ILE/Acetone (sol 3) in a 53/35/12 volumetric ratio (6/2/3 mole ratio). 0.2 wt % NHT was added and stirred overnight. Spin coating was conducted on plasma cleaned Si wafers at 2000 RPM for 15 sec-onds. The spun sol was exposed at 365nm for 13 minutes with a UVP Blak-Ray B-100 lamp at a distance of 6 inches. Ambient humidity fluctuated between 40-50%. The sol was subsequentially aged for 1 hour in ambient conditions before rinsing in a cyclohexane/MMA solution. MMA was used due to its partial solubility with the ionic liquid. The photo-patterned gel was dried at 110°C.

3.2.2 Characterization Techniques

Thermogravimetric analysis (TGA) was performed using a TA Instruments SDT Q600. The spun ionogels were tested between 30-600°C with a ramp rate of 10°C min^{-1} and held at max temperature for 1 hour.

N_2 adsorption testing was performed using a Micromeritics ASAP 2010 instrument. To characterize the silica network in the ionogel, we modified a procedure reported previously [65]. In the current case, the ionogel was immersed in acetone which tends to dissolve the IL. Then, the acetone is removed by supercritical drying using liquid CO_2. In this way the acetone is removed

without generating the capillary forces that would collapse the SiO_2 network. Samples were out-gassed overnight at 110°C before testing. Testing was conducted at 77°K. BET (Brunauer–Emmett–Teller) surface areas were calculated at 0.24 P/P_o and BJH (Barrett-Joyner-Halenda) pore distributions were calculated from the isotherm data.

Fourier transform infrared spectroscopy (FTIR) was performed using a Jasco 670 Plus. 10 μL of the precursor sol was drop cast onto Thermo Electron Corporation PTFE IR cards. Spectra for the ionogels were taken after carrying out the equivalent processing conditions as those for the spun films. The spectra were taken from 400-4000 cm^{-1} with a resolution of 4 cm^{-1}.

SEM was performed using a FEI Nova 230 Nano SEM with attached EDS. Imaging and EDS mapping were done on cross-section and planar views of the gel films spun on $LiFePO_4$ cathodes and Si wafers. Cross sections were obtained for Si wafers by cleaving a diamond scribed wafer and by sectioning the LFP cathode.

TEM (transmission electron microscopy) images were obtained with a FEI Technai G2 T20 and used to determine a representative pore size. Images were taken of spin-coated films of gel 1 and gel 2 that were supercritically dried.

AFM (atomic force microscopy) was performed on a Bruker Dimension Icon. Scanning was conducted using a silicon probe. Scans were performed using peak force tapping mode in 10μm x 10μm sections.

3.2.3 Electrochemical Testing

$LiFePO_4$ (LFP; MTI), Carbon Black Super P (99%+, Alfa Aeser), Timrex KS4 graphite (MTI), polyvinylidene fluoride (PVDF Sigma Aldrich) and 1-methyl-2-pyrrolidinone (NMP

99.5% anhydrous, Sigma Aldrich) were used without further processing. Slurries were made with 75 wt % $LiFePO_4$, 10 wt % KS4, 5 wt % Super P, and 10 wt % PVDF dispersed in NMP and doctor bladed onto carbon coated aluminum foil. Mass loading of the LFP electrodes was typically 1.5 mg cm^{-2} with a film thickness of 28 microns. Films were tested in a two-electrode configuration versus lithium metal. Pseudo-solid state cells used spun films of gel 1 or gel 2 as the electrolyte, although these cells also contained a Celgard separator to ensure electrical isolation. For reference, electrochemical cells were constructed that used an ionic liquid electrolyte of 0.5M LiTFSI [BMIM] [TFSI that was soaked in a Celgard separator. Galvanostatic (GV) and electrochemical impedance spectroscopy (EIS) measurements were made using a BioLogic VMP3 potentiostat. The frequency range for the EIS was from 1MHz to 100 mHz with a 10 mV amplitude. The measurements were made in a stainless steel (SS) Swagelok. The temperature dependence of the impedance was obtained by measuring (EIS) between 20 and 120°C. The electrochemical window was obtained for gel 1 by sweeping different voltage ranges using cyclic voltammetry (CV) in a three electrode Swagelok with SS as the working electrode (WE) and counter electrode (CE) and Li metal serving as the reference electrode (RE). GV cycling was performed for both the neat ILE as well as with pseudo-solid state cells that used spin coated gel 1 and 2 in a LFP/Li metal cell. Cycling was performed between 2.5-4V at C/10, C/5, and C/2. Long term cycling was conducted at C/2 for 150 cycles for gel 1 and 80 cycles for gel 2.

3.3 Results & Discussion

3.3.1 Materials Processing

The synthesis route of Membreno, et al., which was based on the hydrolysis of tetramethylorthosilicate (TMOS) and triethylvinylorthosilcate (VTEOS) with formic acid, was adapted to control the gelation rate of gel 1 (see Experimental Procedure for details).[21] The resulting mesoporous network trapped the ionic liquid electrolyte (ILE) leading to materials (bulk monoliths and thin films) which were macroscopically rigid but exhibited certain properties, such as ionic conductivity, that behave as a liquid at the nanoscale. An overview of the process is shown in Figure 3.1.
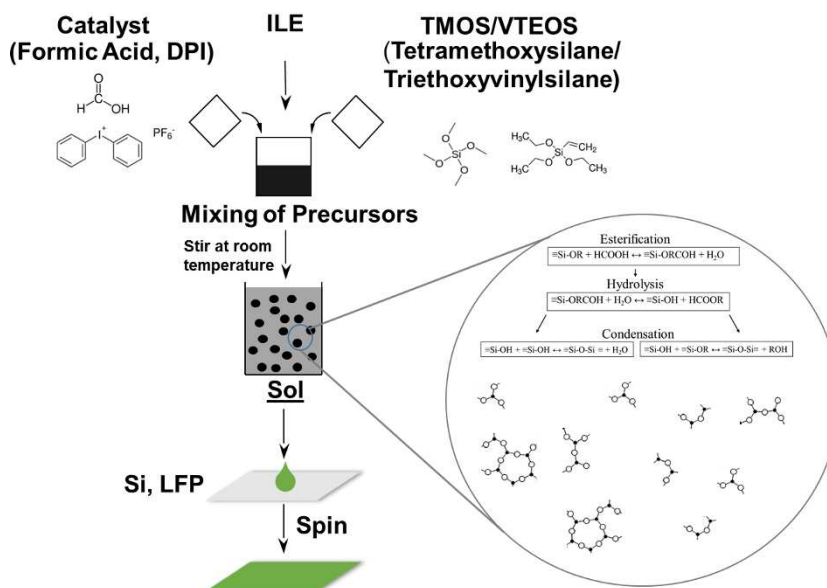
Figure 3.1: Schematic of ionogel synthesis for spin coating.

Gel 2 follows a similar synthesis route using photo-produced HPF_6 rather than formic acid as the acid catalyst for hydrolysis. By using acid catalysis, Brinker and colleagues proposed that hydrolysis occurs rapidly through the protonation of the siloxane to form silanols leading to the Si atom becoming electrophilic.[22] Due to the electrophilicity, further protonation of Si, and thus condensation, occurs along more basic silanol species such as monomers or the end groups of chains. The preferential condensation at the end groups forms extended linear-like chains. These chains quickly deplete the available monomer inducing condensation to occur between end groups and less acidic regions of other chains forming an open, highly branched network.[23] Incorporating ionic liquid into the sol retains the open porous silica network as the ionic liquid does not evaporate. The lithium concentration and fraction of ionic liquid in the structure greatly affect the properties of the ionogel such as the viscosity in the sol state, its penetration into porous electrodes and structural integrity of the matrix.[24,25] In the present study 75 vol % ILE was chosen as the amount of liquid phase as this ionogel exhibits good mechanical integrity coupled with ion transport properties. 0.5M lithium bis(trifluoromethanesulfonyl)imide (LiTFSI) was used to ensure an adequate supply of lithium in the ionogel without producing a high viscosity ILE that would reduce the ionic conductivity.

The morphology of the silica network in the ionogel was characterized using N_2 adsorption methods. For these measurements, the ionogel was processed using a supercritical drying procedure which retains the mesoporous network of the wet gel (see Experimental Procedure). Figures 3.2A and 3.2B show that the networks developed in gels 1 and 2 exhibit Type IV isotherms with a combination of H2 and H3 mesopores based on the hysteresis. This response suggests the pores are a mixture of slit-shaped (H3) and "ink bottle" shapes (H2).[26]
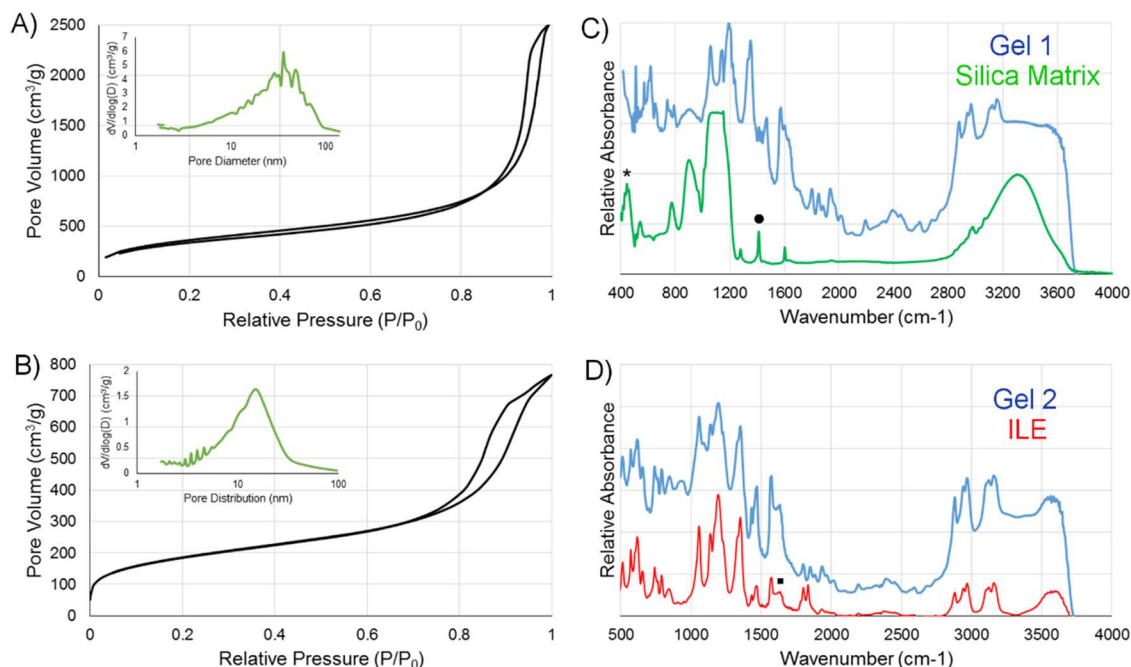
Figure 3.2: Physical Structure and Bonding of Ionogels

A) N$_2$ adsorption isotherm for gel 1 and (B) gel 2. Inset is the calculated BJH pore size distribution from the adsorption isotherms. C) FTIR spectrum for gel 1 and the silica matrix gelled in the absence of ILE. D) FTIR spectrum of gel 2 with an overlay of the ILE spectrum. Peaks associated with Si-O-Si (ˣ), =CH$_2$ (●), and the VC (▪) are indicated.

The surface area calculated from the isotherm in Figure 3.2A gives a value of 1300 m^2 g^{-1}. BJH analysis of the adsorption indicates a broad pore size distribution with an average pore diameter of 20 nm. N$_2$ adsorption of gel 2 leads to a surface area of 700 m^2 g^{-1}. In this case, BJH analysis displays a narrower pore size distribution with an average pore diameter of 10 nm. TEM imaging confirms the approximate pore size of 10 to 20 nm for spin coated gels 1 and 2 (Figure 3.3A, 3.3B). TEM images also confirm the formation of a mesoscale, sponge-like network that is penetrated with ILE.
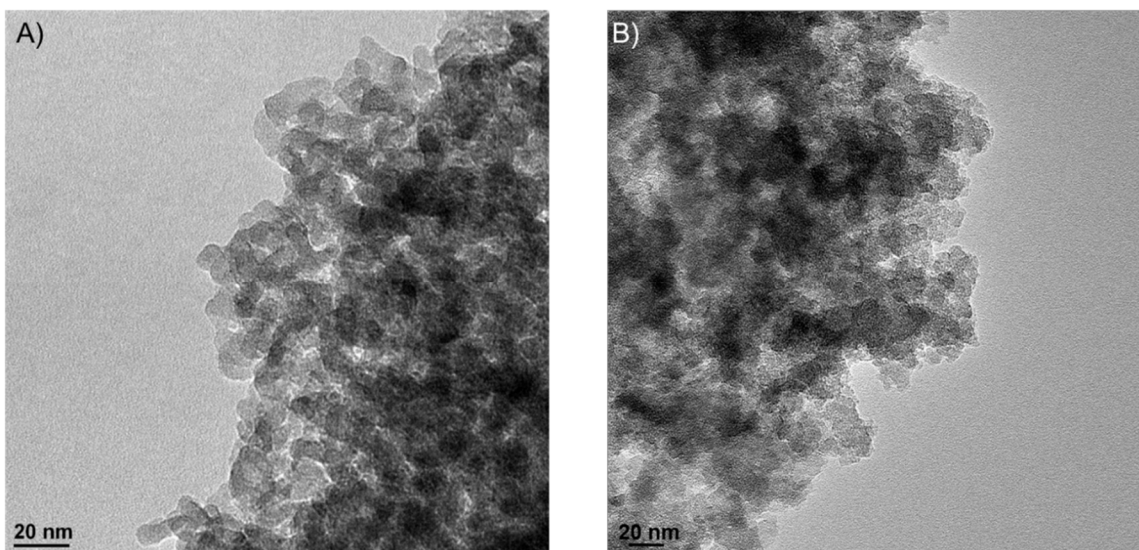
Figure 3.3: Nanostructure Induced from Confined ILE
TEM images of spin coated gels that are supercritically dried; (A) gel 1. (B) gel 2.

The lower surface area for the photo-processed gel 2 compared to gel 1 is believed to originate from the photo-produced HPF_6 acid. PF_6 anions have been shown to undergo hydrolysis in the presence of water to form HF.[27] As shown by various researchers, the effect of the fluoride anion is to accelerate hydrolysis and condensation through nucleophilic attack.[28-31] In the case of iono-gels, Viau, et al. reported that the presence of the PF_6 anion led to a higher degree of silica con-densation compared to chloride anions.[32] For these reasons, we expect that the microstructures resulting from photo-produced HPF_6 are similar to those of base catalysis with smaller pores and reduced surface area.[28,33] While lower than gel 1, the surface area of gel 2 is still quite significant and enables an interconnected pore network.

The structural development and chemical interactions of the ILE with the silica matrix were characterized using FTIR (Figure 3.2C, 3.2D). The spectra for gels 1 and 2 display the Si-

O-Si bending peak associated with the silica matrix at 470 cm⁻¹, indicating that gelation has oc-

curred.[34] Other peaks associated with silica are dominated by the ILE peaks limiting their useful-

ness for identification. FTIR spectra for gels 1 and 2 in the absence of ILE (Figure 3.4A, 3.4B),

show that gelation has occurred through the disappearance of peaks at 2850 and 2950 cm⁻¹ which

are associated with the silica precursor.
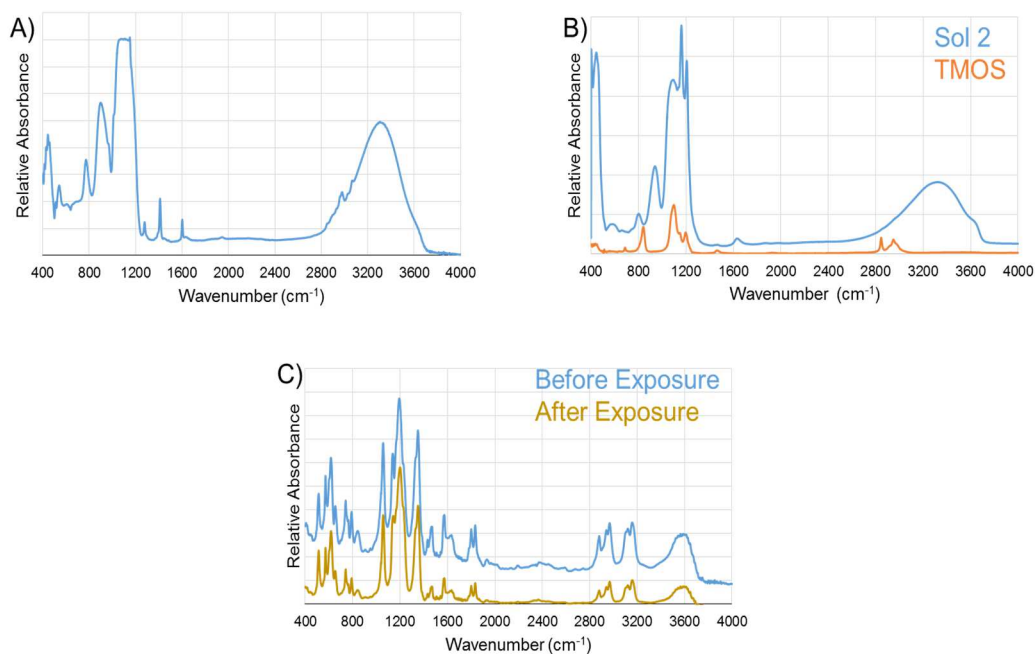
Figure 3.4: The Effect of Processing Conditions on the Ionogel Components

A) FTIR spectrum for gel 1 in the absence of ILE. B) FTIR spectrum for gel 2 in the absence of ILE under UV exposure of 180 mJ/cm². C) ILE spectrum before and after UV exposure.

The peak located at 1410 cm⁻¹ associated with the C-H bend of the =CH₂ vinyl group does not

change during gelation indicating that it is unaffected by the reaction (Figure 3.2C).[34] In addi-

tion, the FTIR spectra for both ionogels (Figure 2C, 2D) show the peak at 1640 cm⁻¹ which is at-

tributed to the skeletal stretching mode of the electrolyte additive, vinylene carbonate (VC; Figure 3.2D)), is unchanged thus demonstrating it is not affected by the synthesis.[35] Looking at Figure 3.4C, we see that UV exposure used in gel 2 does not have an effect on the ionic liquid. By comparing the spectra of ILE and sol-gel matrices without ILE to those obtained from the ionogels (Figure 3.2C, 3.2D), we can determine that there are no new peaks in the ionogel spectrum signifying it is a superposition of the two individual components. This indicates that the ILE is not chemically interacting with the silica matrix but is only physically bound. Physical confinement is believed to only moderately influence the transport properties.[36] In contrast, previous studies have shown interaction between the ionic liquid and the silica matrix. This interaction is believed to originate from the use of highly electronegative anions.[37,38]

3.3.2 Properties of Confined Ionic Liquid Electrolyte

A key consideration for ionogel systems is whether the ILE retains its inherent properties when confined within the SiO_2 network. Thermal gravimetric analysis (TGA) performed on the ionogels shows a weight loss starting at ~370 °C associated with the thermal breakdown of the IL (Figure 3.5A). The magnitude of the weight loss of the ILE for both ionogels indicates that the ILE comprises approximately 75 vol % of the ionogel structure. The small amount of loss in the silica matrix starting at 100°C, 2% of the entire weight, is related to trapped water along with reaction products from silanol condensation.[39] The fact that there is minimal weight loss for both ionogels in the 100°C temperature range indicates that the ILE ratio and not the synthesis route determines the amount of ionic liquid in the structure. The slightly higher decomposition temper-

ature for the IL in ionogels 1 and 2 compared to the ILE is believed to be associated with the capillary forces arising from the mesoporous network which lower the vapor pressure of the ionic liquid and increases condensation on the pore walls.[40]

The ion transport properties of the ionogel films were determined by measuring the complex impedance between 1MHz and 100mHz as a function of temperature, from 20 to 120°C. Drop cast and spin coated gels 1 and 2 were placed in a stainless steel Swagelok cell which functioned as the sample holder. Spin coated ionogels were deposited on p-type Si which served as a conductive substrate while the drop cast samples were gelled inside a glass container, removed, and sandwiched between the stainless steel electrodes. In Figure 3.5B and 3.5D, the spin coated and drop cast films are compared to the neat ILE and the well-known solid electrolyte, LiPON. The room temperature conductivity for drop cast gel 1 is only slightly less than that of the neat ILE (2 mS cm^{-1} *vs*. 3 mS cm^{-1}) while the drop cast gel 2 sample has a lower conductivity (~0.2 mS cm^{-1}). This range of values is typical for ionogels[37,41–43] and the conductivity of the ILE is in good agreement with other ionic liquid electrolytes using similar electrolyte compositions.[43–45] The activation energy for conduction as determined from the temperature dependence is ~ 0.15 eV for the ionogels and the ILE. These values compare well to activation energies found for other silica ionogels and are approximately 3 - 4x smaller than those found in oxide systems such as LLZO and LiPON. [24,37,41,46] Comparing the conductivities and activation energies of drop cast gels 1 and 2 with that of the neat ILE establishes that encapsulation of the ILE in the silica matrix does not have an appreciable effect on ion transport. This behavior is consistent with the absence of chemical interaction between phases as observed in the FTIR results.
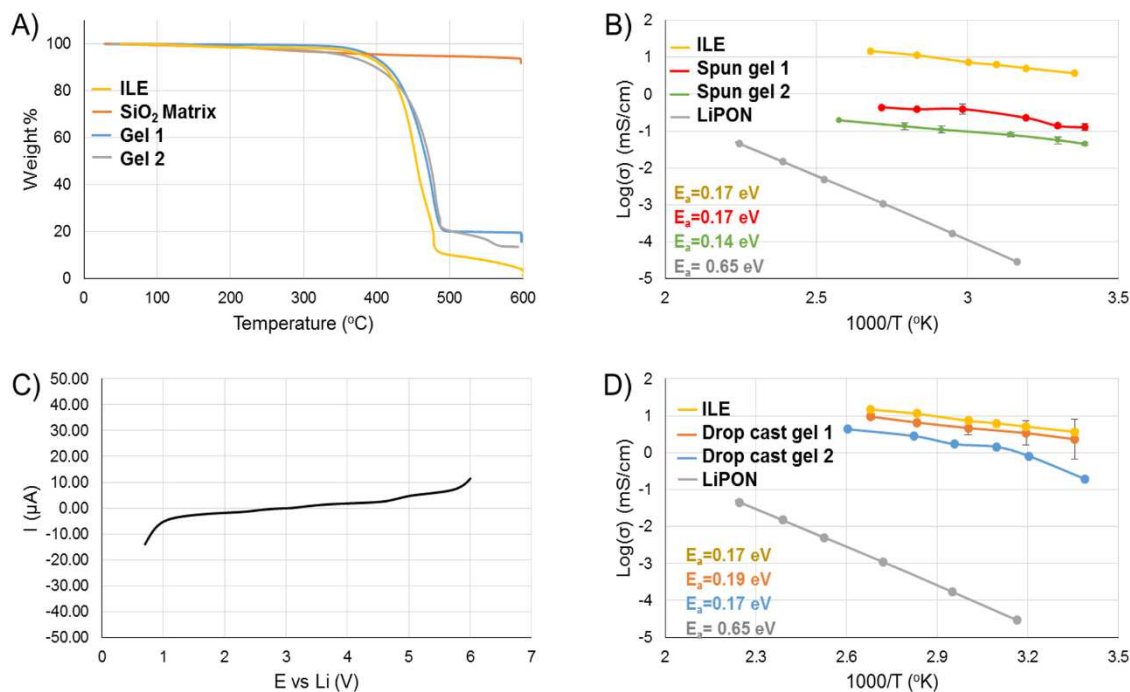
Figure 3.5: Confinement Effect on the ILE Properties

A) TGA showing the thermal stability of the ILE, gel 1, gel 2 and the silica matrix without ILE. B) Temperature dependence of the ionic conductivity for spin coated gel 1 and gel 2. Data is represented as the mean with error bars. These ionogels are compared to neat ILE and LiPON. The activation energies are shown. C) Electrochemical window of gel 1 in a cell with a stainless steel working electrode and lithium metal as the counter and reference electrode. D) Temperature dependence of the ionic conductivity for drop cast gel 1 and gel 2. Data is represented as the mean with error bars. These ionogels are compared to neat ILE and LiPON. The activation energies are shown. LiPON ionic conductivity was obtained from published data.[55]

The difference in the conductivities between drop-cast and spin coated samples can be attributed to the difference in processing conditions. The spinning of the sol creates a dynamic processing condition for gelation as evaporation and centripetal forces will affect the sol. Studies of spin coated silica films have shown the development of a small non-uniformity in density and thickness due to mass transfer from air flow and shear rates affecting the viscosity.[52] With non-

48

newtonian fluids (ionic liquids), a non-uniformity in thickness occurs due to the higher shear forces on the edges, decreasing viscosity.[48] It is possible that non-uniformities at the nanoscale will influence the nature of the silica network, impede ion transport and bring about the lower conductivity. The processing associated with gel 2 is different from that of gel 1. This material is crosslinked after spin coating, upon UV exposure. After spin coating, the film is in the wet gel state which enables its nanostructure to relax prior to being crosslinked. For this reason, spin coated gel 2 has comparable conductivity values to drop cast gel 2. Finally, it should be noted that the ionic conductivities for all the ionogel samples are significantly higher than the ionic conductivities found for LiPON.[49,50]

While high ionic conductivity is essential for batteries, the electrolyte itself also must have electrochemical stability. When swept anodically, the electrochemical window for the drop cast gel 1 ionogel exhibits a high breakdown potential of 5.4V vs Li. When swept cathodically, breakdown starts to occur at 1V (Figure 3.5C). Taken together, these results indicate that the ionogels have an electrochemical window of 4.6V. This correlates well with the values found in literature for [BMIM] [TFSI].[51,52]

3.3.3 Ionogel Processing Control

A critical issue associated with the use of ionogel electrolytes is that the sol precursor must successfully infiltrate the porous electrode in order to provide the source of Li^+ required for energy storage reactions. That is, gelation needs to be controlled so that it occurs well after spin coating or else electrolyte access to the redox-active material will be limited, lowering energy density and, in all likelihood, power density. Scanning electron microscopy (SEM) and Energy Dispersive X-Ray Spectroscopy (EDS) were carried out on both cross-sectional and planar views

of gel 1 in order to characterize the uniformity and conformality of infiltration of the spun iono-

gels (Figure 3.6A, 3.6B).
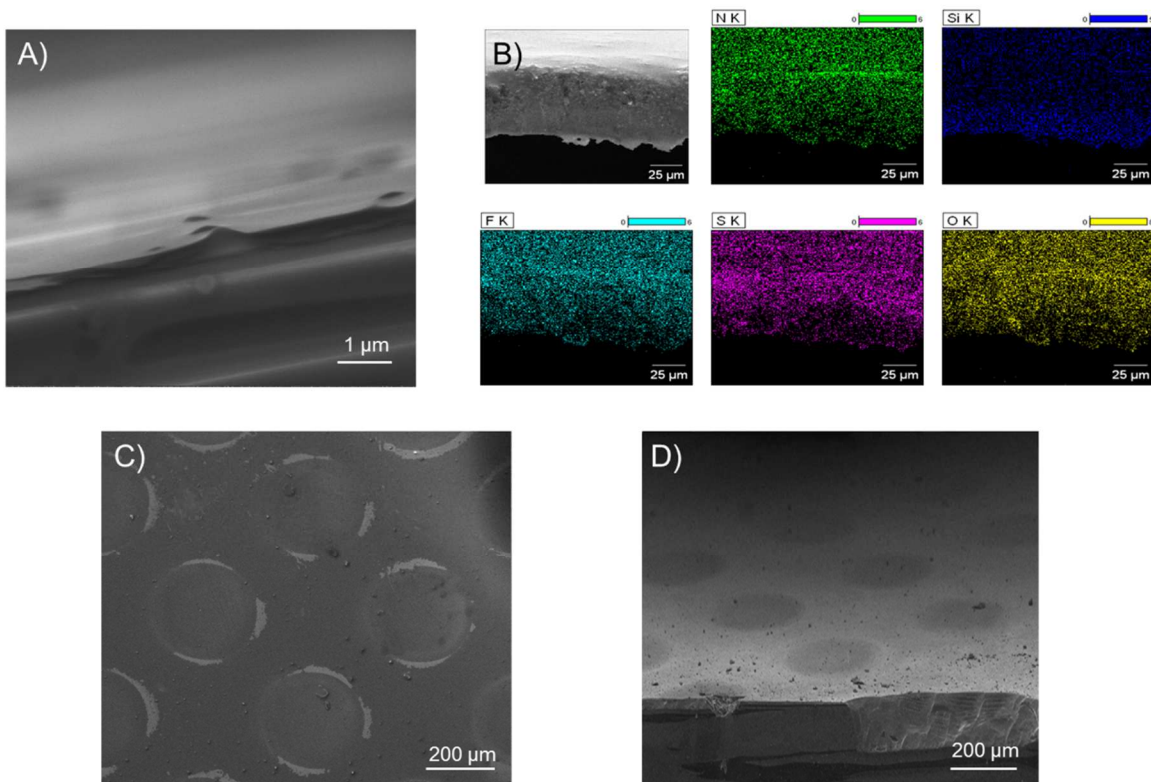
Figure 3.6: Topographical and Penetration Ability of Ionogels

A) SEM cross section of gel 1 spun on a Si wafer with a micron scale bar. B) Gel 1 spun on a LFP cathode. EDS mapping shows the penetration of the ILE and SiO$_2$ components N, Si, F, S, and O with a 25 micron scale bar. C) SEM planar view of gel 3 spun on Si wafer with a 200 micron scale bar. The diameter of the patterned circles is 250 μm. D) Cross-sectional SEM image of photo-patterned gel 3 spun on a Si wafer with a 200 micron scale bar.

Si wafers and LFP electrodes served as substrates and were used to illustrate, respectively, the

ability of the sol to create quality surface films and to penetrate a porous electrode. The planar

view of the Si exhibits a uniform surface with ionic liquid found homogeneously throughout the

structure. AFM analysis shows that a high quality surface is produced with a roughness on the

50

order of 10 nm (Figure 3.7). Cross sections of the spin-coated Si sample show the uniformity of

the film structure, indicating only a small deviation in thickness across the electrode. As shown

in Figure 3.6A, the average ionogel film thickness was 600 nm. By varying the spin speed, it will

be possible to fabricate thinner ionogel films as the thickness is expected to be inversely propor-

tional to the square root of the spin speed.[48]
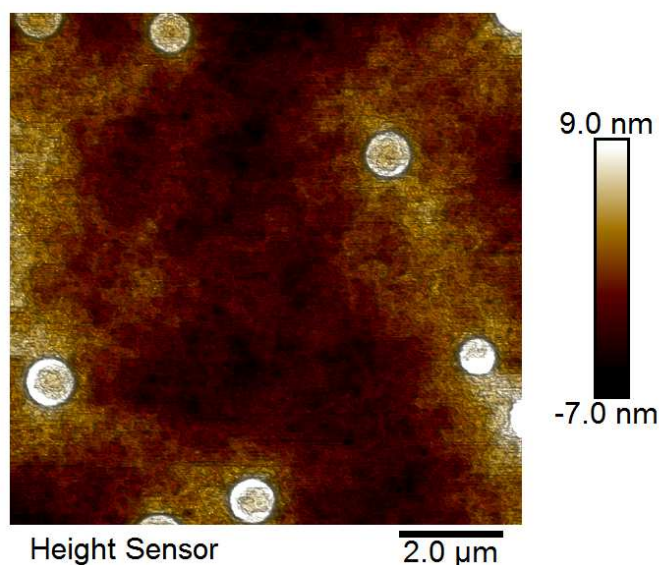
Figure 3.7: Surface Uniformity of Spin coated Ionogels
AFM image of the surface of gel 1. Surface roughness was calculated to be 9.7nm.

Cross sectional analysis of the LFP/ionogel samples show that the precursor sols for gels

1 and 2 thoroughly penetrate into a porous electrode structure (Figure 3.6B). EDS mapping of

both the IL constituents (N, F, S) and those of silica (Si, O) establishes that both the IL and SiO_2

components are distributed evenly within the LFP. This microstructure analysis indicates that the

electrolyte is continuous and seemingly accesses all the LFP particles. Furthermore, the surface

of the cross section indicates that the electrolyte matches the roughness of the electrode. This

morphology and the low electronic conductivity of silica (10^{-13} S cm^{-1}) suggest that the ionogels

may be used directly and without the need for a separator.[53] While additional testing is required to ensure the absence of pinholes, these results show that the spun ionogel can serve as a solid electrolyte film that has the potential to eliminate the need for traditional battery separators.

In this study, we developed an additional functionality for ionogels, namely photopatterning. Photo-patterned electrolytes provide an opportunity to alter battery fabrication procedures and to create battery architectures which are better adapted for integration in complex electronic structures. By adapting the UV synthesis route used for gel 2, we are able to successfully pattern an ionogel film. In this process, the sol precursor for gel 3 was spin coated onto a silicon wafer before exposure. After exposure with a UV lamp operating at 365 nm, the gel was aged, rinsed and dried overnight. SEM imaging of the UV patterned gel 3 shows the distinct pattern of ordered circles with a diameter of 250 μm (Figure 3.6C, 3.6D; 3.8B). The region immediately surrounding the patterned film is silica where a portion of the ionic liquid has been removed. EDS shows that the ionic liquid is retained within the silica structure in appreciable quantities (Figure 3.8A). It should be noted that the significant presence of silicon is associated with signal from the Si wafer. To the best of our knowledge, this is the first example of a photo-patterned Li$^+$ ionogel film. Further optimization of the UV patterning conditions and sol composition are expected to lead to higher resolution patterns.
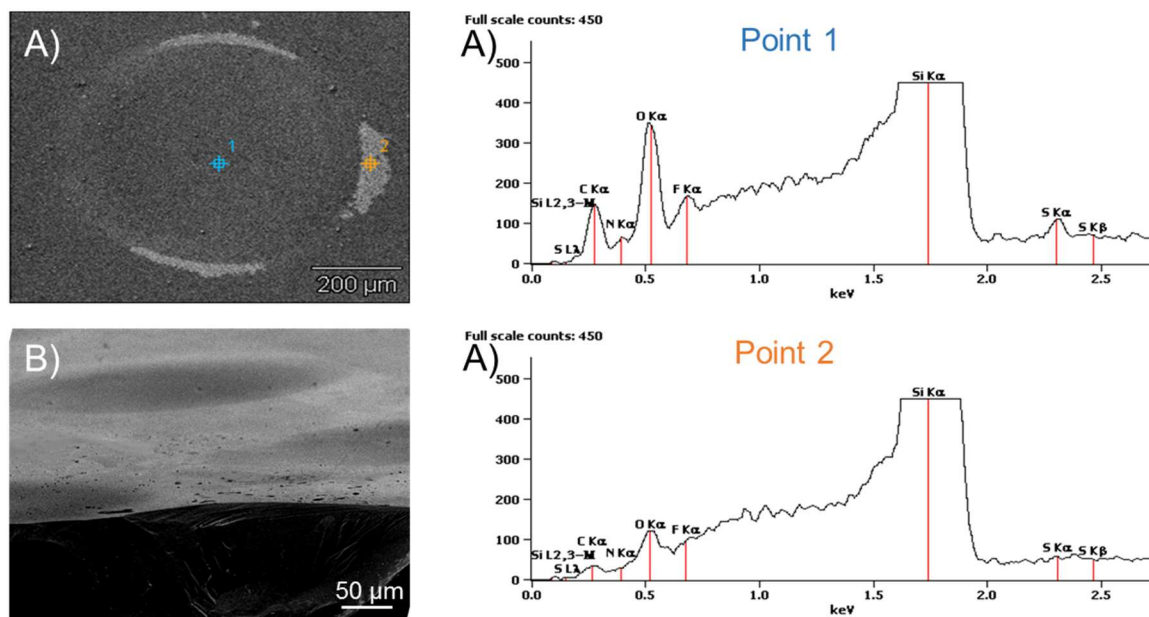
Figure 3.8: Composition Uniformity of Photopatterned Ionogels

A) EDS analysis of the photo-patterned gel 3. EDS was taken at locations in the center of the structure and on the edge. B) Cross-sectional image of gel 3.

3.3.4 Electrochemical Characterization

As mentioned above, ionic liquids possess several desirable properties that make them attractive for use as Li⁺ electrolytes. For this reason, ionic liquids have been studied extensively with a range of positive and negative electrodes used in Li⁺ batteries. In most cases, the ionic liquids display comparable performance to that of carbonate electrolyte based Li⁺ battery cells.[54-57] In general, ionic liquid electrolytes have poorer rate capability, although several studies have shown their potential for use in low rate battery applications. A study by Kim, et al. using N-butyl-N-methylpyrrolidinium bis(fluorosulfonyl)imide ([Pyr13] [FSI]) electrolyte in LFP half cells showed stable capacities of 160 mAh g⁻¹ over 240 cycles.[61] Similar results (140 mAh g⁻¹ at C/10

) were obtained in LFP half cells using 1-n-butyl-1-ethyl-pyrrolidinium bis(trifluoromethanesul-fonyl)imide ([Pyr24] [TFSI]), further indicating their potential as electrolytes for Li^+ batteries.[59] The capacity obtained for our neat ILE cell (145 mAh g^{-1}) matches well with the above systems.

Recently, ionogels have been investigated for use as solid electrolytes for lithium ions. In 2009, Echelmeyer, et al. showed that incorporating lithium salts into a silica ionogel led to Li ion conduction.[60] Subsequently, lithium ionogels were explored for a variety of energy storage systems. To date, some of the more prominent studies have been performed using LFP cathode systems.[61-63] The best results were reported by Tan et al. who synthesized 30 μm ionogel films that achieved 150 mAh g^{-1} for 100 cycles at C/10.[24] These results are on par with their neat ionic liquid electrolyte. Delannoy, et al. demonstrated the inkjet printing of an ionogel sol, obtaining a 10 μm thick conformal electrolyte. These full-cell experiments achieved reasonable capacities (125 mAh g^{-1}) but at low rates (C/30).[64] Bideau et al. reported the fabrication of 5 μm ionogel films prepared by drop casting. In this work, however, lower capacities of 110 mAh g^{-1} were obtained at C/20.[12]
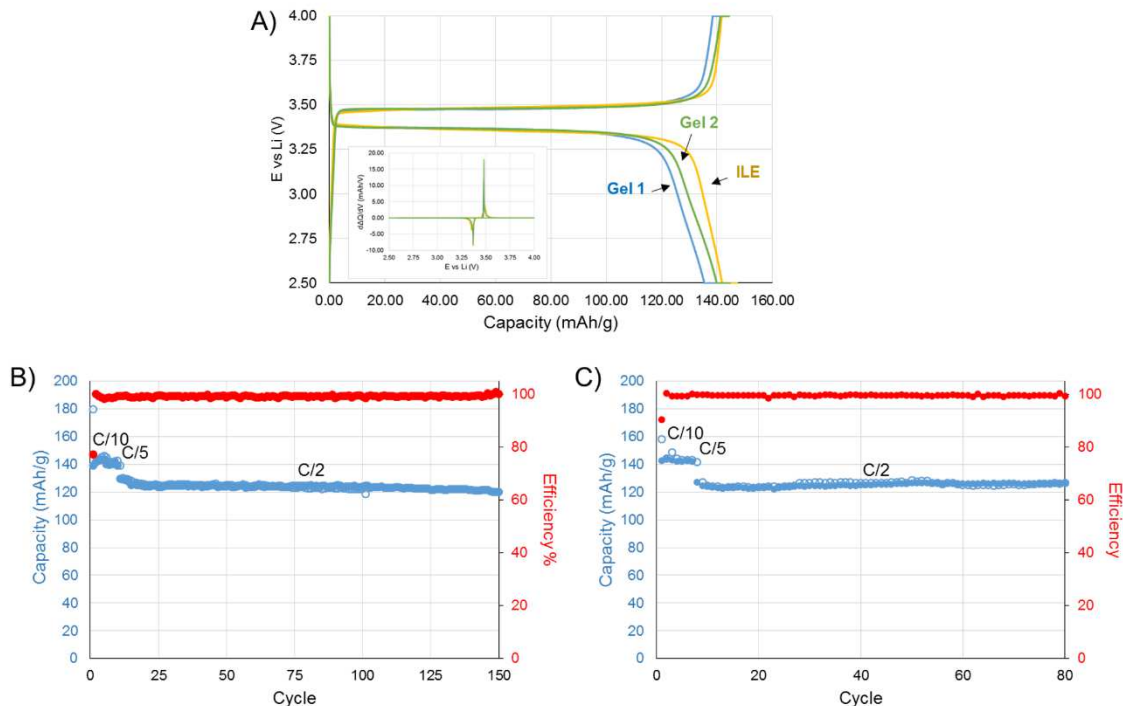
Figure 3.9: Electrochemical Properties of Thin Film Ionogels

A) Galvanostatic measurements of different electrolytes on LFP at C/10. Results are shown for gel 1 and gel 2, with the ILE serving as a comparison. The inset shows the dQ/dV vs V curves extrapolated from the GVs. (B) Capacity variation with cycling for gel 1. Majority of the 150 cycles were at C/2. (C) Capacity variation with cycling for gel 2. Majority of the 80 cycles were at C/2.

In our work to date, we have investigated two different ionogel thin films that were spin coated onto LFP electrodes and evaluated in LFP/ionogel/Li electrochemical cells. Capacities of 145 mAh/g were obtained at C/10 for gel 1. These values are virtually identical to that of the neat ILE (Figure 3.9A), underscoring the importance of controlling the sol state so that it successfully penetrates the porous LFP electrode. The dQ/dV inset illustrates the low level of polarization between the reduction and oxidation reactions. In addition, we successfully increased the rate to C/2 and maintained capacities of 125 mAh/g with only a 4% loss over 150 cycles (Figure 3.9B)

with a coulombic efficiency above 99%. Our LFP/ionogel/Li battery compares very favorably against other LFP battery structures with ionogel electrolytes (Table 1). In particular, our full cells exhibit higher power density. By moving to a thinner film (600 nm), we overcome the relatively lower ionic conductivity arising from the high viscosity of the ionic liquid. The energy density values exceed all but a few reports and in those instances, our power densities are significantly greater.

The second ionogel evaluated in LFP/ionogel/Li electrochemical cells was prepared using UV crosslinking. Prior to the current study, the only UV processed ionogels involved crosslinking of organic matrices which lack the thermal stability and mechanical integrity of the inorganic systems. Nonetheless, reasonable performance was reported; Aidoud, et al. carried out UV crosslinking of an acrylic-based ionogel and achieved capacities of 130 mAh/g at a rate of C/5.[19] Lee, et al. had similar results using a polyethylene glycol matrix (Boron-PEGDMA), achieving capacities for LFP cells of around 140 mAh g^{-1} at C/20.[42] Our electrochemical studies on gel 2 are apparently the first ones for a UV crosslinked inorganic matrix. The capacity for this system was similar to gel 1 as 145 mAh g^{-1} was obtained at C/10; this result was nearly identical to the capacity obtained from the neat ILE (Figure 3.9A). At C/2, the LFP/Li battery exhibited a capacity of 125 mAh g^{-1} with good reversibility (80 cycles) and showed virtually no loss of capacity during cycling (Figure 3.9C). Here, too, the coulombic efficiency was in excess of 99%. The ability to achieve high capacity at relatively fast rates indicates that the UV crosslinking process does not affect the ionogel's ability to wet the electrode nor does this approach lead to side reactions. These results suggest that photopatterning an inorganic ionogel will be able to provide spatial resolution of device structures without compromising device performance.

Table 3.1: Full Cell Ionogel Comparison

The nature of the ionic liquid and salt varies among the different studies. With one exception (Delannoy), the capacity is normalized by the weight of the LFP electrode. Studies marked with (*) represent UV crosslinked ionogels. The current results are highlighted.

Paper	Matrix	Cathode	Anode	Full Cell Capacity (mAh g^{-1})	Wh kg^{-1}	Rate(C)	Power (W kg^{-1})
Current Work	SiO$_2$-Gel 1	LFP	Li	125	406.3	0.5	203.15
Li, et al. (2015)	TiO$_2$	LFP	Li	110	357.5	0.5	178.75
Bideau, et al. (2011)	SiO$_2$	LFP	Li	110	341	0.05	17.05
Delannoy, et al. (2015)	SiO$_2$	LFP	Li$_2$TiO$_3$	65	97.5	0.1	9.75
Lee, et al. (2015)	Polysilsesquioxane	LFP	Li	90	301.5	0.1	30.15
Li, et al. (2015)	SiO$_2$/PVDF	LFP	Li	150	487.5	0.1	48.75
Tan, et al. (2016)	SiO$_2$	LFP	MCMB	145	478.5	0.1	47.85
Current Work*	SiO$_2$-Gel 2	LFP	Li	124	403	0.5	201.5
Lee, et al. (2016)*	Boron/PEGDMA	LFP	Li	150	502.5	0.1	50.25
Aidoud, et al. (2016)*	Acrylate Mixture	LFP	Li	130	403	0.2	80.6
Lee, et al. (2015)*	PEO/Polysilsesquixane	LFP	Li	60	195	0.5	97.5

3.4 Conclusion

In summary, we used different processing approaches to obtain a pseudo-solid state electrolyte based on the confinement of an ILE within a sol-gel derived SiO$_2$ matrix. In addition to using traditional hydrolysis and condensation reactions to form the matrix (gel 1), we also demonstrated that UV crosslinking could be used to form the matrix (gel 2). Using this UV-based approach, we demonstrated the photolithographic patterning of simple structures (gel 3). Both types of gels exhibited the thermal and electrochemical stability and ionic conductivity representative of the confined ILE. Pseudo-solid state devices based on incorporating the ionogels in

electrochemical cells with Li and LFP as negative and positive electrodes, respectively, were investigated. These cells exhibited higher power density than those reported for other ionogel electrolytes with comparable or better energy density. A key feature in this work is that of controlling the sol to ensure that the electrolyte has access to the entire LFP electrode.

3.5 References

1.   Kopetz, H. *Real-Time Systems: Design Principles for Distributed Embedded Applications*. (Springer, 2011).

2.   P.A. Nelson, K.G. Gallagher, I. Bloom, D. W. D. *Modeling the Performance and Cost of Lithium-Ion Batteries for Electric-Drive Vehicles Chemical Sciences and Engineering Division*. (2012).

3.   Fergus, J. W. Ceramic and polymeric solid electrolytes for lithium-ion batteries. *J. Power Sources* **195,** 4554–4569 (2010).

4.   Dudney, N. J., West, W. C. & Nanda, J. *Handbook of Solid State Batteries*. (World Scienctific, 2016).

5.   Johnson, R. W., Hultqvist, A. & Bent, S. F. A brief review of atomic layer deposition : from fundamentals to applications. *Mater. Today* **17,** 236–246 (2014).

6.   Liu, Y., Liao, S. & Liu, B. H. Nanoscale electrochemical characterization of a solid-state electrolyte using a manganese-based thin-film probe. *Nanoscale* **8,** 19978–19983 (2016).

7.   Wang, X. & Hao, J. Recent advances in ionic liquid-based electrochemical biosensors. *Sci. Bull.* **61,** 1281–1295 (2016).

8.   Hatipoglua, G. *et al.* Fabrication and electromechanical performance of a novel high modulus ionogel micro-actuator. *Procedia Eng.* **25,** 1337–1340 (2011).

9.   Ghamsari, A. K., Jin, Y., Zegeye, E. & Woldesenbet, E. Bucky gel actuator displacement: experiment and model. *Smart Mater. Struct.* **22,** 025034 (2013).

10.   Zhang, S., Zhang, J., Zhang, Y. & Deng, Y. Nanoconfined Ionic Liquids. *Chem. Rev.* **117,** 6755-6833 (2016).

11.   Tarascon, J. M. & Armand, M. Issues and challenges facing rechargeable lithium batteries. *Nature* **414,** 359–367 (2001).

12.   Le Bideau, J., Ducros, J. B., Soudan, P. & Guyomard, D. Solid-state electrode materials with ionic-liquid properties for energy storage: The lithium solid-state ionic-liquid concept. *Adv. Funct. Mater.* **21,** 4073–4078 (2011).

13.   Liu, C. Recent developments in polymer MEMS. *Adv. Mater.* **19,** 3783–3790 (2007).

14.   Decker, C. The use of UV irradiation in polymerization. *Polym. Int.* **45,** 133–141 (1998).

15.   Crivello, J. V. The Discovery and Development of Onium Salt Cationic Photoinitiators. *J. Polym. Sci. A Polym. Chem.* **37,** 4241–4254 (1999).

16.   Shirai, M. & Tsunooka, M. Photoacid and photobase generators: Chemistry and applications to polymeric materials. *Prog. Polym. Sci.* **21,** 1–45 (1996).

17.   De Paz, H., Chemtob, A., Croutxé-Barghorn, C., Le Nouen, D. & Rigolet, S. Insights into photoinduced sol-gel polymerization: An in situ infrared spectroscopy study. *J. Phys. Chem. B* **116,** 5260–5268 (2012).

18.   Doshi, D. a. *et al.* Optically defined multifunctional patterning of photosensitive thin-film silica mesophases. *Science (80).* **290,** 107–111 (2000).

19.   Aidoud, D. *et al.* Interfacial stability and electrochemical behavior of Li/LiFePO$_4$ batteries using novel soft and weakly adhesive photo-ionogel electrolytes. *J. Power Sources* **330,**

92–103 (2016).

20. Kim, D., Lee, G., Kim, D. & Ha, J. S. Air-stable, high-performance, flexible microsupercapacitor with patterned ionogel electrolyte. *ACS Appl. Mater. Interfaces* **7,** 4608–4615 (2015).

21. Membreno, D., Smith, L. & Dunn, B. Silica sol-gel chemistry: Creating materials and architectures for energy generation and storage. *J. Sol-Gel Sci. Technol.* **70,** 203–215 (2014).

22. Brinker, C. J. Hydrolysis and Condensation of Silicates. *J. Non. Cryst. Solids* **100,** 31–50 (1988).

23. Danks, A. E., Hall, S. R. & Schnepp, Z. The evolution of 'sol–gel' chemistry as a technique for materials synthesis. *Mater. Horizons* **3,** 91–112 (2016).

24. Tan, G. *et al.* Solid-State Li-Ion Batteries Using Fast, Stable, Glassy Nanocomposite Electrolytes for Good Safety and Long Cycle-Life. *Nano Lett.* **16,** 1960–1968 (2016).

25. Horowitz, A. I. & Panzer, M. J. High-performance, mechanically compliant silica-based ionogels for electrical energy storage applications. *J. Mater. Chem.* **22,** 16534 (2012).

26. Rouquerolt, J. *et al.* Recommendations for the characterization of porous solids. *Pure Appl. Chem.* **66,** 1739–1758 (1994).

27. Freire, M. G., Neves, C. M. S. S., Marrucho, I. M. & Coutinho, A. P. Hydrolysis of Tetrafluoroborate and Hexafluorophosphate Counter Ions in Imidazolium-Based Ionic Liquids. *J. Phys. Chem. A* **2,** 3744–3749 (2010).

28.   Pope, E. J. A. & Mackenzie, J. D. SOL-GEL PROCESSING OF SILICA II. The role of the catalyst. *J. Non. Cryst. Solids* **87,** 185–198 (1986).

29.   Scherer, G. W. *Sol-Gel Science: The Physics and Chemistry of Sol-Gel Processing.* (Academic Press, 1990).

30.   Iler, R. *The Chemistry of Silica.* (Wiley-Interscience Publication, 1979).

31.   Rodriguez, R. & Flores, M. Master behaviour for gelation in fluoride-catalyzed gels. *Mater. Lett.* **15,** 242–247 (1992).

32.   Viau, L. *et al.* Ionic Liquid Mediated Sol-Gel Synthesis in the Presence of Water or Formic Acid: Which Synthesis for Which Material? *Chem. Mater.* **24,** 3128–3134 (2012).

33.   Kajihara, K. Recent advances in sol–gel synthesis of monolithic silica and silica-based glasses. *J. Asian Ceram. Soc.* **1,** 121–133 (2013).

34.   Al-Oweini, R. & El-Rassy, H. Synthesis and characterization by FTIR spectroscopy of silica aerogels prepared using several $Si(OR)_4$ and $R''Si(OR')_3$ precursors. *J. Mol. Struct.* **919,** 140–145 (2009).

35.   Dorris, K. L., Danti, A., Boggs, J. E. & Altpeter Jr, L. L. Infrared and Raman Spectra of Vinylene Carbonate. *J. Chem. Phys.* **46,** 1191–1193 (1967).

36.   Guyomard-Lack, A., Said, B., Dupré, N., Galarneau, A. & Le Bideau, J. Enhancement of lithium transport by controlling the mesoporosity of silica monoliths filled by ionic liquids. *New J. Chem.* **40,** 4269–4276 (2016).

37.   Noor, S. A. M., Bayley, P. M., Forsyth, M. & MacFarlane, D. R. Ionogels based on ionic

liquids as potential highly conductive solid state electrolytes. *Electrochim. Acta* **91,** 219–226 (2013).

38.   Wu, C., Lin, S., Kao, K. & Chen, H. Self-Organization of a Hydrophilic Short-Chain Ionic Liquid Confined within a Hydrophobic Nanopore. *J. Phys. Chem. C* **118,** 17764–17772 (2014).

39.   Mizumo, T., Watanabe, T., Matsumi, N. & Ohno, H. Preparation of ion conductive inorganic–organic composite systems by in situ sol–gel reaction of polymerizable ionic liquids. *Polym. Adv. Technol.* **19,** 1445–1450 (2008).

40.   Mangun, L. & Daley, M. A. Effect of pore size on adsorption of hydrocarbons in phenolic-based activated carbon fibers. *Carbon.* **36,** 123–131 (1998).

41.   Guyomard-Lack, A. *et al.* Hybrid silica-polymer ionogel solid electrolyte with tunable properties. *Adv. Energy Mater.* **4,** 1–6 (2014).

42.   Lee, A. S. *et al.* Boronic ionogel electrolytes to improve lithium transport for Li-ion batteries. *Electrochim. Acta* **215,** 36–41 (2016).

43.   Guyomard-Lack, A. *et al.* Destructuring ionic liquids in ionogels: enhanced fragility for solid devices. *PCCP* **16,** 23639–45 (2014).

44.   Fromling, T., Kunze, M., Schonhoff, M., Sundermeyer, J. & Roling, B. Enhanced lithium transference numbers in ionic liquid electrolytes. *J. Phys. Chem. B* **112,** 12985–12990 (2008).

45.   Monteiro, M. J., Bazito, F. F. C., Siqueira, L. J. a, Ribeiro, M. C. C. & Torresi, R. M.

Transport Coefficients, Raman Spectroscopy, and Computer Simulation of Lithium Salt Solutions in an Ionic Liquid. *J. Phys. Chem. B* **112,** 2102–2109 (2008).

46.   Loho, C., Djenadic, R., Bruns, M., Clemens, O. & Hahn, H. Garnet-Type $Li_7La_3Zr_2O_{12}$ Solid Electrolyte Thin Films Grown by CO_2-Laser Assisted CVD for All-Solid-State Batteries. *J. Electrochem. Soc.* **164,** A6131–A6139 (2017).

47.   Vorotilov, K., Petrovsky, V. & Vasiljev, V. Spin coating process of sol-gel silicate films deposition: Effect of spin speed and processing temperature. *J. Sol-Gel Sci. Technol.* **5,** 173–183 (1995).

48.   Acrivos, A., Shah, M. J. & Petersen, E. E. On the Flow of a Non-Newtonian Liquid on a Rotating Disk. *J. Appl. Phys.* **31,** 963–968 (1960).

49.   Pearse, A. J. *et al.* Nanoscale Solid State Batteries Enabled by Thermal Atomic Layer Deposition of a Lithium Polyphosphazene Solid State Electrolyte. *Chem. Mater.* **29,** 3740–3753 (2017).

50.   Munoz, F. *et al.* Increased electrical conductivity of LiPON glasses produced by ammonolysis. *Solid State Ionics* **179,** 574–579 (2008).

51.   Ong, S. P., Andreussi, O., Wu, Y., Marzari, N. & Ceder, G. Electrochemical windows of room-temperature ionic liquids from molecular dynamics and density functional theory calculations. *Chem. Mater.* **23,** 2979–2986 (2011).

52.   Lewandowski, A. & Stępniak, I. Relative molar Gibbs energies of cation transfer from a molecular liquid to ionic liquids at 298.15 K. *Phys. Chem. Chem. Phys.* **5,** 4215–4218

(2003).

53.   Anderson, J. H. & Parks, G. A. The Electrical Conductivity of Silica Gel in the Presence of Adsorbed Water. *J. Phys. Chem.* **177,** 3662–3668 (1968).

54.   Xu, K. Nonaqueous liquid electrolytes for lithium-based rechargeable batteries. *Chem. Rev.* **104,** 4303–4417 (2004).

55.   Lee, J. S., Bae, J. Y., Lee, H., Quan, N. D. & Kim, H. S. H. Ionic liquids as electrolytes for Li ion batteries. Journal of Industrial and Engineering Chemistry 10, 1086–1089 (2004).

56.   Xu, K. Nonaqueous liquid electrolytes for lithium-based rechargeable batteries. Chem. Rev. 104, 4303–4417 (2004).

57.   Lewandowski, A. & Świderska-Mocek, A. Ionic liquids as electrolytes for Li-ion batteries-An overview of electrochemical studies. *J. Power Sources* **194,** 601–609 (2009).

58.   Kim, J. K., Matic, A., Ahn, J. H. & Jacobsson, P. An imidazolium based ionic liquid electrolyte for lithium batteries. *J. Power Sources* **195,** 7639–7643 (2010).

59.   Reale, P., Fernicola, A. & Scrosati, B. Compatibility of the $Py_{24}TFSI$-LiTFSI ionic liquid solution with $Li_4Ti_5O_{12}$ and $LiFePO_4$ lithium ion battery electrodes. *J. Power Sources* **194,** 182–189 (2009).

60.   Echelmeyer, T., Meyer, H. W. & Van Wiillen, L. Novel ternary composite electrolytes: Li ion conducting ionic liquids in silica glass. *Chem. Mater.* **21,** 2280–2285 (2009).

61.   Li, X. *et al.* Mesoporous silica/ionic liquid quasi-solid-state electrolytes and their

application in lithium metal batteries. *J. Power Sources* **278,** 128–132 (2015).

62.   Li, X., Zhang, Z., Yang, L., Tachibana, K. & Hirano, S.I. TiO_2-based ionogel electrolytes for lithium metal batteries. *J. Power Sources* **293,** 831–834 (2015).

63.   Lee, A. S. *et al.* Ion Conduction Behavior in Chemically Crosslinked Hybrid Ionogels: Effect of Free-dangling Oligoethyleneoxides. *RSC Adv.* **5,** 94241–94247 (2015).

64.   Delannoy, P. E. *et al.* Toward fast and cost-effective ink-jet printing of solid electrolyte for lithium microbatteries. *J. Power Sources* **274,** 1085–1090 (2015).

65.   Smith, L. C. *et al.* Sol–gel encapsulated lithium polysulfide catholyte and its application in lithium–sulfur batteries. *Mater. Horiz.* **3,** 137–144 (2016).

Chapter 4: Electrochemical and Spectroscopic Analysis of the Ionogel-Electrode Interface in Li⁺ Batteries

This chapter reviews our studies of the chemical and electrochemical properties arising from the interface between a Li⁺ conducting ionogel and various positive and negative electrode materials for lithium-ion batteries. Ionogels, pseudo-solid state electrolytes consisting of an ionic liquid electrolyte confined in a mesoporous inorganic matrix, have attracted interest recently due to their high ionic conductivity and physiochemical stability. These traits, coupled with their inherent solution-processability, make them a viable solid electrolyte to replace Li⁺ liquid electrolytes. Despite the unique properties of ionogel, few studies have investigated the nature of the electrode-ionogel interface. XPS, Raman spectroscopy, and electrochemical testing were utilized to probe the electrode-ionogel interface where surface reactions were identified for several electrode materials. Our results indicate that the sol acidity initiates breakdown of the organic components and reduction of the transition metals present in the electrode materials. This chemical attack forms an organic surface layer and affects the electrode composition, both of which can impede Li⁺ access. By modifying the silica sol-gel reaction via a two-step acid-base catalysis, these interfacial reactions can be avoided for a LCO electrode leading to stable cycling of 110 mAh/g over 50 cycles.

4.1 Introduction

As demand for mobile electronics, smart devices, and electrical transportation increases, the need for lighter, smaller, and safer batteries is of utmost importance.[1] For most

commercial batteries, cells consist of an anode, cathode, and a liquid or polymer electrolyte. Liquid electrolytes are traditionally used due to their high ionic conductivity and ability to wet the electrode surfaces, but they also require a separator and increase the flammability risk.[2] For these reasons, researchers have been exploring ionically conductive solids (solid-state electrolytes, SSE) as stable alternatives. While SSEs are typically more thermally stable than liquids, their lower ionic conductivity limits the achievable power density.[3]

Processing of SSEs is generally restricted to powder pressing and sintering or line-of-site techniques such as sputtering. These techniques are usually conducted at elevated temperatures which, along with the inherent chemical instability of some electrode materials, can produce highly resistive interfaces.[4,5] This is best seen in the sulfide class of SSEs which have ionic conductivities on par with liquids (10^{-2} S cm^{-1}), but are limited by their interfacial stability.[6] The interfacial products typically have ionic conductivities several orders of magnitude lower than the bulk electrolyte, drastically increasing the cell's resistance and potentially leading to continued electrolyte decomposition.[7] Line-of-sight and powder processing methods also have poor infiltration into traditionally porous electrode structures which limits the electrolyte/electrode contact and lowers the cell's storage capacity and obtainable power.

Ionogels, a subclass of solid electrolytes composed of a room temperature molten salt (ionic liquid electrolyte, ILE) confined within an inorganic or organic matrix, have recently garnered interest due to their ability to maintain the inherent properties of the trapped ionic liquid. The principal benefit of ionogels over other solid electrolytes is the ability to be processed as a liquid allowing for facile electrolyte access throughout a slurry-cast electrode.[8]

68

Although ionogels have the capability to be processed as a liquid, an understanding of the chemical interaction of the sol with the electrode interface and its stability is incomplete. The majority of literature has limited the use of ionogels to lithium iron phosphate cells (LFP). There is no compelling reason for this choice over other commercial electrodes with higher energy densities or power densities.[9–11] The question arises whether the LFP/ionogel pairing derives from convention or whether this originates from a physiochemical issue of the sol with other electrodes. Many electrode materials have been stably cycled in ionic liquids indicating any issues of the electrode with the ionogel electrolyte, in all probability, originate from the sol-gel process.[12,13] Thus, for greater adoption of ionogels as electrolytes in lithium-ion batteries, the interface during solution processing of the ionogel on different electrode systems must be understood.

In the present paper, we study the interfacial stability of $LiCoO_2$ (LCO) and other lithium electrode materials when paired with a solution-processed ionogel electrolyte. The interface is studied using x-ray photoelectron spectroscopy (XPS), Raman spectroscopy, and electrochemical tests to elucidate the surface stability when exposed to the sol. We find that the acid catalyst from the sol-gel synthesis leads to interfacial reactions that impede electrochemical cycling. We demonstrate that while LFP is stable in the conditions commonly used in ionogel syntheses, other electrode materials (LCO, $LiNi_{0.8}Co_{0.15}Al_{0.05}O_2$, etc.) show reduction of the transition metal and formation of an organic layer that lead to irreversible capacity loss. By adjusting the silica sol-gel synthesis route, the electrode can be protected from the acid leading to stable cycling comparable to that of the neat ILE.

4.2 Experimental Procedure:

4.2.1 Ionogel Synthesis and Electrode Preparation

Tetramethylorthosilicate (TMOS, 99+%, Sigma Aldrich), triethylvinylorthosilcate (VTEOS, 97%, Sigma Aldrich), and formic acid (Puram, Fluka Analytical) were used for the silica sol-gel reaction. The ionic liquid electrolyte was synthesized from lithium bis(tri-fluoromethanesulfonyl)imide (LiTFSI, 99.95%, Sigma Aldrich) and l-butyl-3-methylimidaz-olium bis(trifluoromethanesulfonyl)imide ([BMIM] [TFSI], 99.5%, Solvionic). Methanol (MeOH, Fisher Chemical ACS) was used during analysis of the electrode powders and sol-gel synthesis. Lithium hydroxide (LiOH, 99.995% monohydrate, Sigma Aldrich) was obtained for the modified gel.

Ionic liquid was first degassed using a vacuum oven and bubbled with Ar at 150°C before storing inside an Ar gas filled, l ppm H_2O glovebox. 0.5M LiTFSI BMIM TFSI ionic liquid electrolyte (ILE) was then prepared from the degassed ionic liquid. The ionogel fabrication and processing parameters were reported in a previous paper.[14]

For the modified gel, equal volumetric amounts of TMOS, VTEOS, and formic acid were sonicated until mixed. An equal volumetric ratio of the silica precursor solution (TMOS,VTEOS, and formic acid) and ILE was prepared and aged for 3 hours at -20°C. After aging, 20 mg/ml solution of LiOH in MeOH was added to the sol during mixing in a 1:2 volumetric ratio of sol:LiOH solution. The gel was mixed for 1 hour before spinning. Spin coating was conducted at 4000 rpm for 15 seconds onto the cast electrodes using a Headway Research Inc. instrument (PWM32). The gels were aged in a desiccator overnight before drying for 4 hours in a 120 °C

oven. Bulk ionogels were formed by drop casting the modified gel with the same aging parameters for characterization tests.

4.2.2 Electrochemical Testing

LiFePO$_4$ (LFP; MTI), LiCoO$_2$ (LCO; MTI), LiNi$_{0.8}$Co$_{0.15}$Al$_{0.05}$O$_2$ (NCA; MTI), LiMn$_2$O$_4$ (Sigma Aldrich electrochemical grade), and V$_2$O$_5$ (Sigma Aldrich 99.99%) were obtained as electrode active materials. Nb$_2$O$_5$ was synthesized using a previously reported sol-gel process.[15] Amorphous silicon (a-Si) was deposited by electron beam physical vapor deposition (CHA Mark 40, CHA Industries, Fremont, CA, USA) onto stainless steel current collectors with a thickness of 30nm ($\approx$8 µg cm^{-2}). Carbon Black Super P (99%+, Alfa Aeser), Timrex KS4 graphite (MTI), polyvinylidene fluoride (PVDF, Sigma Aldrich) and 1-methyl-2-pyrrolidinone (NMP 99.5% anhydrous, Sigma Aldrich) were used without further processing. Electrode slurries were made with 75 wt% active material, 10 wt% KS4, 5 wt% Super P, and 10 wt% PVDF dispersed in NMP and doctor bladed onto carbon coated aluminum foil. Mass loading of the electrodes was typically 1.5 mg/cm^2 with a film thickness of approximately 30 microns. In experiments designed to characterize the ionogel-electrode interface, ionogel films were spun directly onto the electrode material. In these stainless steel Swagelok cells, lithium metal served as the counter and reference electrode and to ensure electrical isolation, these cells contained a Celgard separator. In control experiments designed to evaluate the ionic liquid–electrode interface, the ionic liquid electrolyte was comprised of 0.5M LiTFSI [BMIM] [TFSI] soaked in a Celgard separator. Once again, stainless steel Swagelok cells were assembled with lithium metal serving as the counter and reference electrode. Galvanostatic (GV) cycling was performed using a BioLogic VMP3 potentiostat. Cycling was performed between 2.5- 4V for

LFP, 3-4.2V for LCO and NCA, 2-4V for V_2O_5, 0.2-1.5V for a-Si, and 3.5-4.5V for LMO at C/10. Nb_2O_5 was cycled at 2C between 1.2-3V as previous research showed worse cyclability at slow rates. The cell that evaluated the modified gel-LCO interface was additionally cycled for 50 cycles at C/5. A LCO/Ionogel/Li cell using an oxalic acid catalyzed ionogel was additionally cycled. Electrochemical impedance spectroscopy (EIS) at a 10 mV amplitude between 1 MHz and 100 mHz was performed on symmetric cells consisting of LFP/LFP and LCO/LCO electrode materials. In these experiments, the cast electrodes were assembled with an ionogel sol at different stages of gelation.

4.2.3 Electrode Chemical Analysis

Raman Analysis (Renishaw inVia confocal Raman microscope) was performed on the LCO powder exposed to ILE, TMOS, and MeOH diluted formic acid corresponding to a pH of 1.6. The LCO powder was mixed in 6 mg/ml solutions and immersed for one week with periodic mixing. 10 μL aliquots were then dropped on glass slides. Analysis was performed with a 514 nm Ar laser and 1800/mm grating through a 20x objective lens.

X-ray photoelectron spectroscopy (XPS; Kratos Axis Ultra) with a monochromatic aluminum X- ray source was used to probe the surface of the active material after exposure to the acid catalyst. Peak calibration was performed using the adventitious carbon peak. The electrode materials were exposed to the same formic acid/MeOH solution as used for the Raman analysis. 10 μL aliquots were dropped after exposure for 1 week onto aluminum. Ionogel sol was spun onto LCO at a spin speed of 10000 RPM before analysis and dried overnight. Acetic acid (Sigma Aldrich glacial), oxalic acid (Sigma Aldrich anhydrous), citric acid (Sigma Aldrich monohydrate >99%), and hydrochloric acid (HCl, Sigma Aldrich

ACS Reagent 37%) were diluted to a pH of 3 in MeOH based on their dissociation constants in water. LCO was exposed to the acid/MeOH solution for 1 week with periodic stirring before 10 µL aliquots were dropped onto aluminum. All samples were allowed to dry ambiently before performing the XPS analysis.

N_2 adsorption testing was performed using a Micromeritics ASAP 2010 instrument. To characterize the silica network in the ionogel, we modified a procedure reported previously.[16] In the current case, the ionogel was immersed in acetone which tends to dissolve the ILE. Then the acetone is removed by supercritical drying using liquid CO_2. In this way, the acetone is removed without generating the capillary forces that would collapse the SiO_2 network. Samples were outgassed overnight at 110°C before testing. Testing was conducted at 77°K. BET (Brunauer-Emmett-Teller) surface areas were calculated at 0.2 P/P_o and DFT pore distributions were calculated using the Tarazona cylindrical pore model provided by Micromeritics Instruments from the isotherm data.

TEM (transmission electron microscopy) images were obtained with a FEI Technai G2 T20 and used to determine the effect of the acid. Images were taken of the formic acid exposed and unexposed electrode powders.

4.3 Results & Discussion

4.3.1 Ionogel-Electrode Interfacial Reactions

Ionogels have been increasingly used as a solid electrolyte for Li^+ batteries.[17,18] Silica ionogels have been integrated into Li^+ cells through two different approaches: incorporating

the electrolyte as a sol with subsequent gelation (solution-processed) or by separately gelling an ionogel electrolyte and sandwiching it between the anode and cathode (freestanding). While the final configuration is effectively the same, the two processes expose the electrode surface to different chemistries. As freestanding ionogels are gelled before cell fabrication, the electrodes are only exposed to silica and ILE. As such, freestanding ionogels have been used in Li^+ cells with a range of electrode compositions.[18] Although high capacities were obtained for freestanding ionogels, the separate gelation process prevents the sol from penetrating through the electrode and wetting the surface. Processing separately also increases the thickness of the gel which increases the resistance of the cell. For these reasons, solution-processed ionogels where, the sol wets and penetrates the electrode, are favorable. However, solution-processed ionogels have only been reported using LFP. To understand the nature of this limitation, $LiCoO_2$ (LCO) exposed to the ionogel sol was analyzed in terms of its interfacial chemistry, morphology and electrochemical properties. LCO was selected for this series of experiments due to its use frequent use in commercial devices and well understood electrochemical properties.[19-21] LCO has the additional benefit of having shown stable cycling with an ILE electrolyte cell.[22]
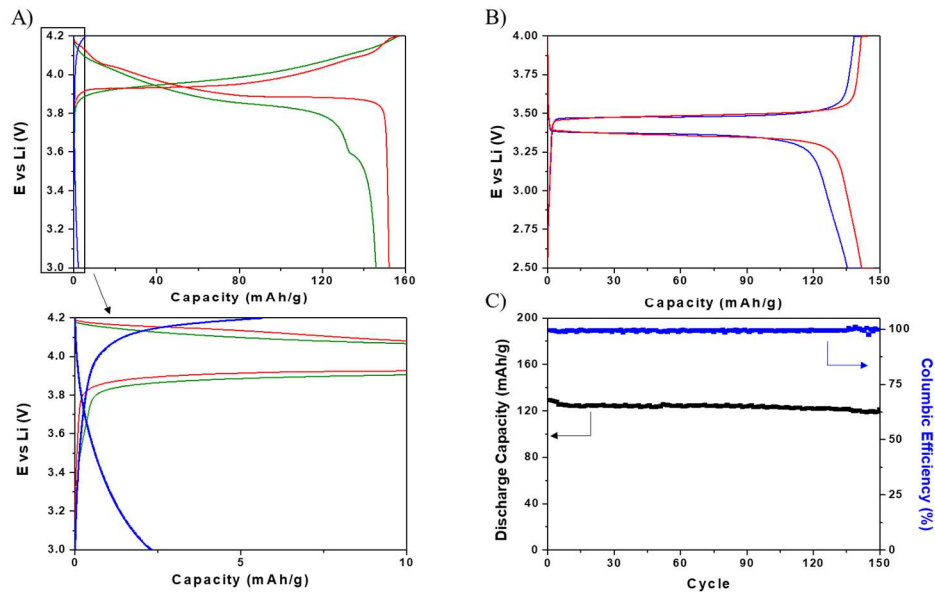
Figure 4.1: Electrochemical Properties of LCO and LFP Ionogel Electrolyte Cells

A) Galvanostatic measurements of different electrolytes for the LCO/Li cell at C/10. Results are shown for ILE (red), a separately processed ionogel (green), and a spun, solution-processed ionogel (blue). A blowup is provided of the low capacity region. (B) Galvanostatic measurements of different electrolytes on LFP at C/10. Results are shown for a spun ionogel (blue) with ILE serving as a comparison (red). (C) Capacity variation with cycling at C/2 for a spun ionogel on LFP for 150 cycles.

Electrochemical cycling of LCO cast electrodes with ionogel electrolyte was performed to identify any electrochemical issues. Processing and cycling conditions were reported earlier in Ashby, et al.[14] Figure 4.1A shows the cycling data for LCO tested at C/10 with neat ILE (red), a freestanding ionogel (green), and the solution-processed ionogel (blue). A blowup of the low capacity region is provided. The figure demonstrates that exposure of the ionogel sol can have a drastic effect on the cycling performance of LCO. For the freestanding ionogel cell, capacities of 140 mAh/g were obtained, comparable to the ILE cy-

cled cell. This is starkly different then the solution-processed ionogel which showed no discernable redox capacity (2 mAh/g). LFP was used as a control to determine if stable cycling could be achieved with the solution-processed ionogel. Figures 4.1B and 4.1C demonstrate that the ionogel sol instability is electrode dependent as stable cycling over 150 cycles (97% retention) was achieved for LFP cycled at C/2. Analyzing the EIS spectrum for a symmetric LCO|LCO cell, the cycling instability can be correlated to the high interfacial resistance (Figure 4.2). The figure shows that the charge transfer resistance greatly increased over 1 day of exposure; such behavior is not seen for the LFP|LFP symmetric cell (Figure 4.2B) subjected to similar exposure. Based on the cycling and impedance data, it is clear that a component of the ionogel sol is affecting the interfacial stability for the LCO|ionogel system.

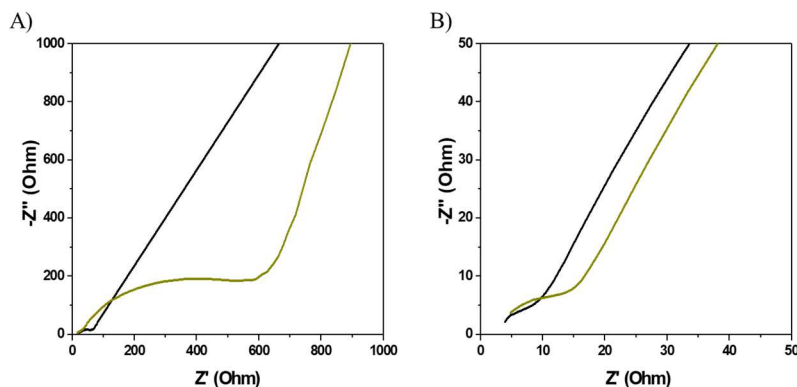**Figure 4.2: Temporal Stability of Ionogel Systems**

A) Electrochemical impedance spectroscopy of an LFP/Ionogel/LFP symmetric cell. (B) Electrochemical impedance spectroscopy of an LCO/Ionogel/LCO symmetric cell. Data is shown for the system immediate after sol addition (black) and after 1 day (gold).

4.3.2 Mechanism of the Acid Attack

The LCO|ionogel interface was analyzed through spectroscopic and microscopic

methods after exposure to the chemical components present in the ionogel sol. For a silica-based ionogel, the sol consists of ILE, silica precursor(s), and an acid catalyst. To understand each component's effect, LCO powder was separately exposed for one week to ILE, tetramethylorthosilicate (TMOS), and formic acid. The formic acid molarity was correlated to the acidity of the ionogel sol. TMOS was chosen as a representative inorganic silica precursor. During the sol-gel reaction, hydrolysis and condensation of the TMOS will produce alcohol and water in solution that must be taken into account when analyzing the spectroscopic data.[23] Likewise, the dissociation of the formic acid will produce formate in solution that can take part in chemical reactions.

The exposed powders were analyzed first using Raman spectroscopy. Figure 4.3A-C show the spectra obtained for the LCO powder exposed to ILE, Formic Acid, and TMOS, respectively. Figure 4.3A shows a superposition of the characteristic LCO and ILE Raman spectra, which indicates LCO does not react with the ILE.[24,25] Figure 4.3B also demonstrates that there is no interaction of the LCO powder with the silica precursor with only the characteristic LCO peaks identified. However when LCO is exposed to formic acid, several new peaks appear indicating an instability between the acid and powder (Figure 4.3C). The peak at 670 cm^{-1} has been associated in literature with Co_3O_4, which indicates a change in the cobalt oxidative state occurs.[26] Along with the identified inorganic peak, large carboxylic and C-O peaks appear indicating a reaction between the organic components of the sol.[27] From Raman spectroscopy, it is unclear the exact bonding nature of the organic species.

77
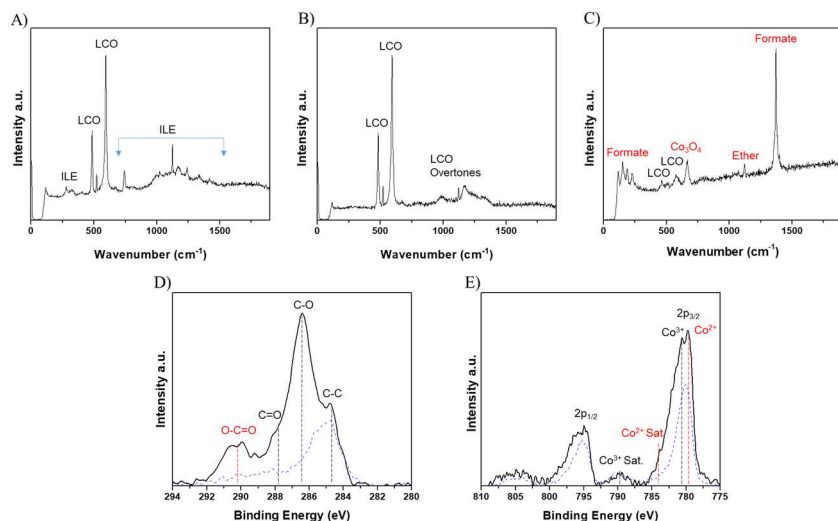
Figure 4.3: Spectroscopic Analysis of the Ionogel Constituents

A) Raman spectroscopy of LCO powder exposed to the ILE electrolyte. (B) Raman spectroscopy of LCO powder exposed to TMOS. (C) Raman spectroscopy of LCO powder exposed to formic acid corresponding to the same molarity as the ionogel sol. Peaks associated with corresponding reacted species (red) and constituents (black) are identified. (D) XPS analysis of the C 1s spectrum for the formic acid exposed LCO powder. (E) XPS analysis of the Co 2p spectrum for the formic acid exposed LCO powder. The unreacted LCO powder spectrum is displayed as the blue dotted line. The reacted species in (D) and (E) are identified (red).
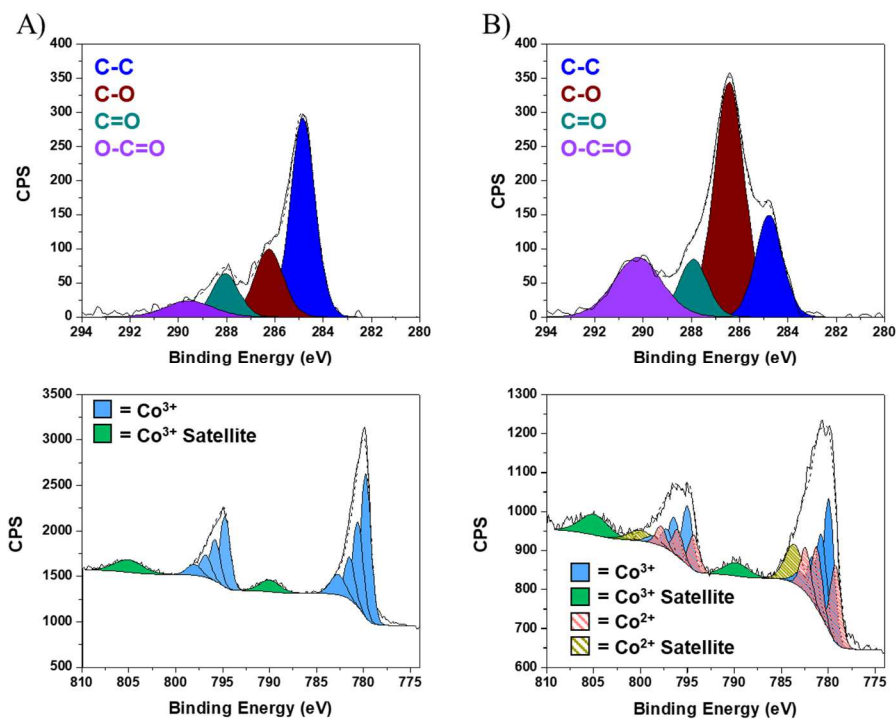
Figure 4.4: XPS Peak Fitting

A) Peak fitting of C 1s and Co 2p spectra for unexposed LCO powder. B) Peak fitting of C 1s and Co 2p spectra for formic acid exposed LCO powder. Multiplet splitting is observed for the Co valence states. The peak envelope is identified by the dotted line.

XPS was performed on the formic acid exposed LCO sample to better identify the products and composition at the interface. XPS analysis focused on the C 1s and Co 2p spectra because of their pertinence to the reaction products identified in the Raman spectra (Figure 4.3D,E). The C ls spectrum confirms that an organic layer forms on the surface as an increase in the C-O and C=O peak intensities occur which correlate well with the Raman data. Formate is identified from the O-C=O peak. The Co 2p spectrum supports the Co^{3+} to Co^{2+} reduction reaction observed seen in the Raman spectra. This result suggests that Co at the interface is either changing phases or transitioning to an inactive intercalation state, either of which could hinder lithium insertion/de-insertion into the LCO material. As the Co-

formate peak overlaps with the Co^{2+} satellite, the presence of cobalt formate on the surface cannot be deconvoluted. XPS peak fitting and identification was performed using Gaussian-Lorentzian peaks and a Shirley background (Figure 4.4). The peak identification process was used to deconvolute the XPS spectra in this chapter.
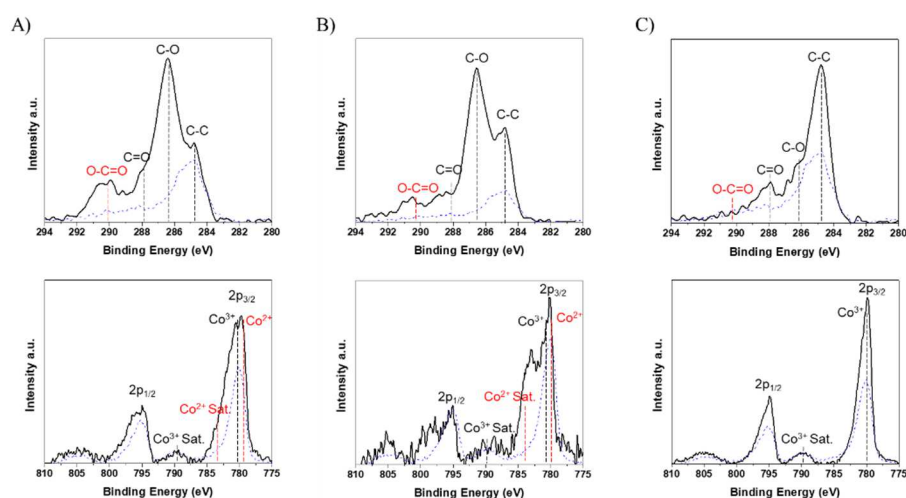
Figure 4.5: Determining the pH Range of Stability

XPS analysis of the LCO powder exposed to different molarities of formic acid corresponding to a (A) pH of 1.6, (B) pH of 3, (C) and a pH of 3.5. The unreacted LCO powder spectrum is displayed as the blue dotted line. The corresponding species are shown for the identified peaks. The species associated with the reacted species are shown (red).

It is unclear from the current testing whether the chemical attack is pH dependent or related to the conjugate base of the acid. To understand the pH dependence, LCO was exposed to formic acid at molarities corresponding to pHs of 1.6, 3, and 3.5 before analyzing using XPS (Figure 4.5A-C). The pH was calculated using the dissociation constant of formic acid in water. The data shows that below pH 3.5 the Co is reduced to the Co^{2+} state and an organic layer develops on the surface. No change in the decomposition products can be identified with the changing pH. At a pH $\geq$3.5, the system is stable to reduction and the acidity is

not sufficient to catalyze alcohol-based reactions.
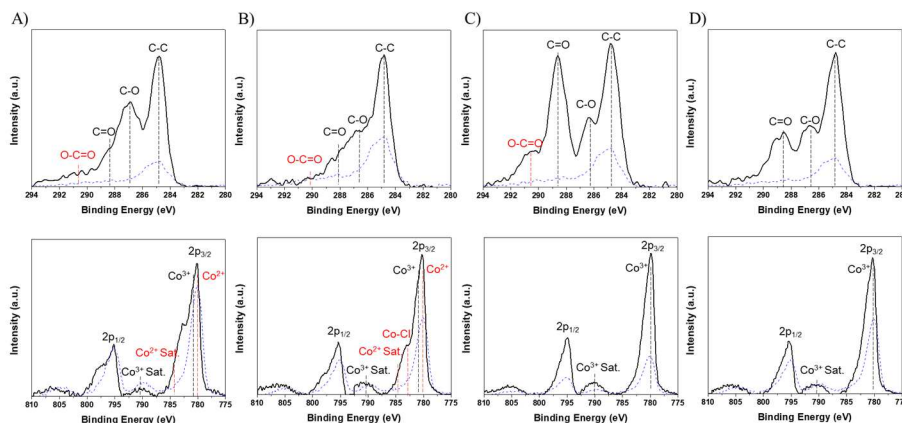
Figure 4.6: Determining the Role of the Acid

XPS analysis of the LCO powder exposed to (A) acetic acid, (B) citric acid, (C) oxalic acid, and (D) HCl with all molarities corresponding to a pH of 3. The unreacted LCO powder spectrum is displayed as the blue dotted line. The corresponding species are shown for the identified peaks. The species associated with the reacted species are shown (red).

XPS was performed on LCO exposed to acetic, citric, oxalic, and hydrochloric acid (HCl) at a pH of 3 to determine the chemical attack dependence on acid composition (Figure 4.5). Organic acids were tested as a nonaqueous route was still desired to reduce the system's water content. The acids were chosen to give a range of dissociation constants, with oxalic and citric acid possessing higher dissociation constants than formic acid whereas the acetic acid constant is lower.[28] The dissociation constant range allows us to discern not only the role of the conjugate base, but if the acid concentration affects the interface stability. HCl was tested as a control to determine if the organic conjugate base affects the reaction mechanism. Figures 4.6A,B show that exposure to acetic and citric acid reduces the system similarly to formic acid. Hydrochloric and oxalic acid exposed LCO do not show Co reduc-

tion seen in the other acids (Figures 4.6C,D). The lack of reduction in the HCl sample indicates the surface instability could be associated with the conjugate base. While no reduction occurred, there is an increase in percentage of organic compounds on the surface for the oxalic acid and HCL exposed LCO. To test the electrochemical performance, oxalic acid catalyzed ionogel was deposited onto LCO electrodes and cycled against lithium metal (Figure 4.7). At a pH of 3 the LCO was still not able to be stably cycled leading to a capacity of only 5 mAh/g at C/10. Further study is required to better elucidate the effect of the conjugate base on the interface reaction and pH stability window for LCO and other lithium-ion electrode materials.
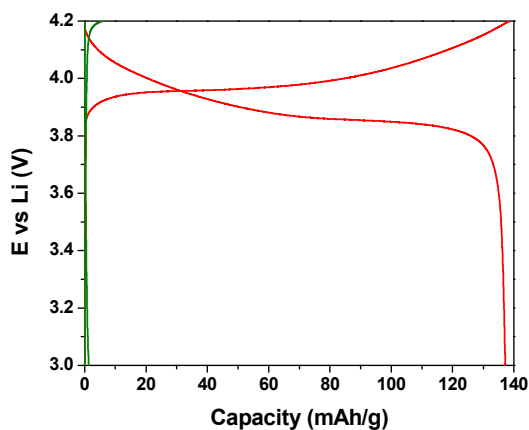
Figure 4.7: The Catalyst's Role in the Ionogel-Electrode Stability
A) Galvanostatic measurements of a pH of 3, oxalic acid-catalyzed ionogel on LCO at C/10. Results are shown for ILE (red) and the citric acid catalyzed ionogel (green).

Two main reaction pathways are proposed to occur from the ionogel sol interaction with LCO (Figure 4.8A). As the proton from the acid interacts with the LCO surface, reduction and dissolution of the Co occurs simultaneously with delithiation forming a surface spinel layer of Co_3O_4 and Co^{2+} and Li^+ in solution. (Equation 1)

82

$$\text{LCO} \xrightarrow{\text{H}^+} \text{Li}_{1-x}\text{Co}_{1-y-z}\text{O}_2 + x\text{Li}^+ + y\text{Co}_3\text{O}_4 + z\text{Co}^{2+} \tag{4.1}$$
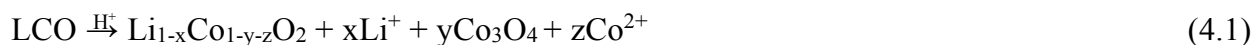
The metal ions can interact with trace amount of water or formate anions to form hydroxides or metal formates. In solution, etherification and esterification of the formate and alcohols is proposed to occur through catalysis by the proton (Equation 2 and 3).[29,30]

$$\text{HCOOH} + \text{ROH} \xrightleftharpoons{\text{H}^+} \text{HCOOR} + \text{H}_2\text{O} \tag{4.2}$$

$$\text{ROH} + \text{R'OH} \xrightarrow{\text{H}^+} \text{ROR'} + \text{H}_2\text{O} \tag{4.3}$$

The two mechanisms would explain the organics identified in the XPS and Raman spectra. The large presence of organics on the surface could also exist due to the catalytic ability of Co_3O_4.[31,32] Acidic attack of LCO has been reported in previous studies that investigated recycling cathode materials. In many of these studies, a strong mineral acid is used to leach Co and Li into solution with efficiencies approaching 100%.[33-35] Even weaker organic acids, such as citric or oxalic acid, have shown dissolution of transition metals from layered cathodes in the pH range used by the majority of silica based ionogel syntheses.[36,37] Comparing TEM imaging of exposed and unexposed LCO, acid exposure is seen to create pitting on the surface which can correlate with the proposed metal dissolution (Figure 4.8B and 4.8C respectively).
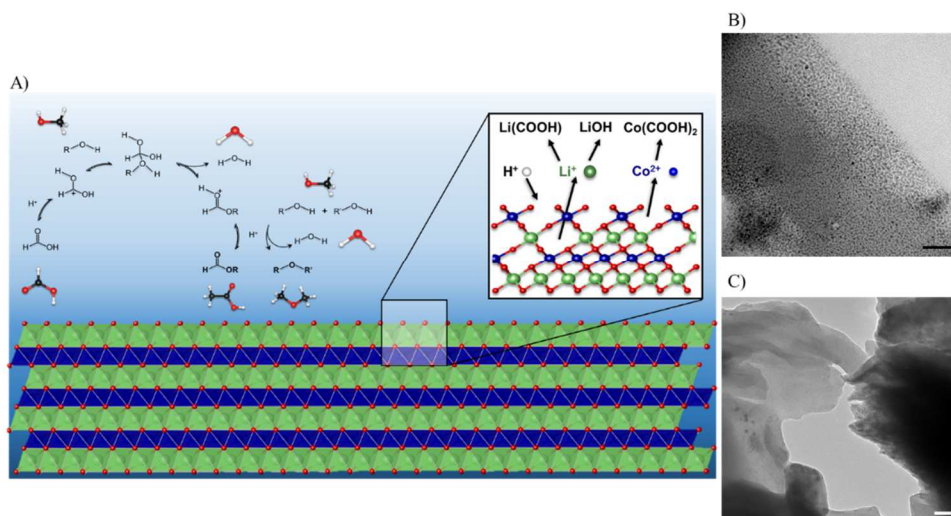
Figure 4.8: The Proposed Chemical Attack

A) Diagram of the proposed chemical attack of the ionogel sol on LCO. (B) TEM imaging of formic acid exposed LCO powder. (C) TEM imaging of the unexposed LCO powder. All scale bars represent 50 nanometers.

4.3.3 Ionogel/Electrode Interfacial Stability for Common Li+ Electrodes

In addition to the interfacial reactions occurring between LCO and a solution-processed ionogel, the question arises as to whether similar reactions are observed with other electrode materials. Several common cathode and anode materials were selected for analysis: $LiMn_2O_4$ (LMO), $LiNi_{0.8}Co_{0.15}Al_{0.05}O_2$ (NCA), Nb_2O_5, V_2O_5, a-Si (amorphous silicon), and LFP. An analogous electrochemical measurement approach to that employed for LCO was used to identify interfacial instabilities as the various electrodes were cycled against Li in ILE or a solution-processed ionogel electrolyte (Figure 4.8). NCA, with the same layered structure as LCO, shows similar cycling behavior as LCO with the ionogel inhibiting Li^+ intercalation/deintercalation (Figure 4.9A). The other electrodes cycled with the ionogel electrolyte show a much higher capacity retention compared to LCO. However, there is a lower

capacity and a greater degree of polarization compared to the ILE, which cannot be explained solely by the resistance of the ionogel (Figure 4.9B-E, 4.1B). All cells, except Nb$_2$O$_5$, were cycled at C/10 rates to reduce any polarization issues arising from the cell resistance. Nb$_2$O$_5$ was cycled at 2C as previous research showed worse cyclability at slow rates.[38] As the polarization for Nb$_2$O$_5$ is comparable to the other cells cycled at C/10, the capacity loss is most likely not due to the electrolyte resistance. From the electrochemical data, it is unclear whether the capacity loss is due to chemical or physical interactions of the electrode with the ionogel or electrode design.
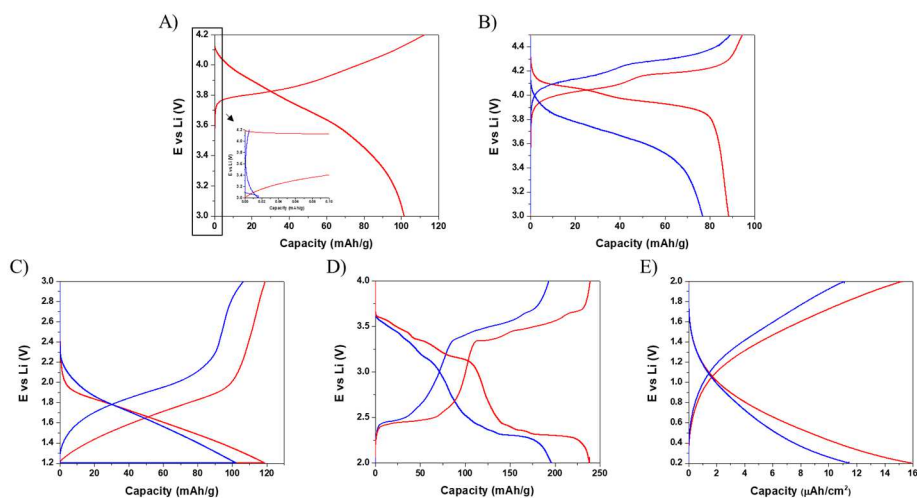
Figure 4.9: Electrochemical Properties of Ionogel Electrolyte Cells

Galvanostatic measurements of different electrolytes on (A) NCA, (B) LMO, (C) Nb$_2$O$_5$, (D) V$_2$O$_5$, and (E) a-Si. All cycling, except for Nb$_2$O$_5$ which was cycled at 2C, was performed at C/10. Results are shown for ILE (red) and ionogel (blue) spun onto the various electrodes.

XPS was used to achieve greater insight regarding the interfacial chemical reactions for each of the cycled electrode materials (Figure 4.9). XPS analysis was performed on the electrode powder after 1 week of exposure to the formic acid corresponding to the same molarity as the ionogel sol. Similar to LCO, NCA exhibits reduction of the Ni^{3+} to Ni^{2+} along

with formation of nickel formate (Figure 4.10A). The C ls spectrum is consistent with the proposed chemical attack mechanism as a large percentage of organics are found at the surface. Like LCO, the significant presence of organics on NCA could relate to the increased catalytic properties of Ni and Co. The XPS spectra for LMO also displays the formation of organics, albeit at lower concentrations than LCO, while also showing an increase in the Mn^{4+}/Mn^{3+} ratio (Figure 4.10B). The stability of LMO to reduction is surprising based on the ease of manganese dissolution during cycling in carbonate electrolytes.[39] Hunter, et al. hypothesized that this increase of the 4^+ state was due to the acidic environment delithiating LMO to form MnO_2.[40] As Li has a low signal to noise ratio in XPS, it is difficult to discern whether there is a change in the Li concentration. The reduction of the lithium concentration and formation of MnO_2 could help explain the lower capacities obtain for the ionogel sample. Additional studies are required to determine if Mn^{2+} was dissolved in solution. Nb_2O_5 and V_2O do show a reduction of the transition metal when exposed to formic acid (Figure 4.10C,4.10D). It is interesting to note that while Nb_2O_5 and V_2O_5 are partially reduced, the capacity retention is comparable to the ILE cells, thus indicating that reduction of the transition metal does not necessarily lead to poor cycling behavior as observed with LCO. Figures 4.10E-F show that exposure of LFP and Si to the ionogel sol does not affect the state of the transition metal or lead to an organic layer. The absence of interfacial reactions with LFP is unsurprising due to the chemical stability of the material.[41] This result is also consistent with studies regarding the leaching of LFP in acidic solutions which show that a low pH is needed for dissolution of the metals.[42,43] Si has a well-known resistance to highly acidic environments due to the native oxide, so its stability versus the ionogel sol is unsurprising.[22]

86
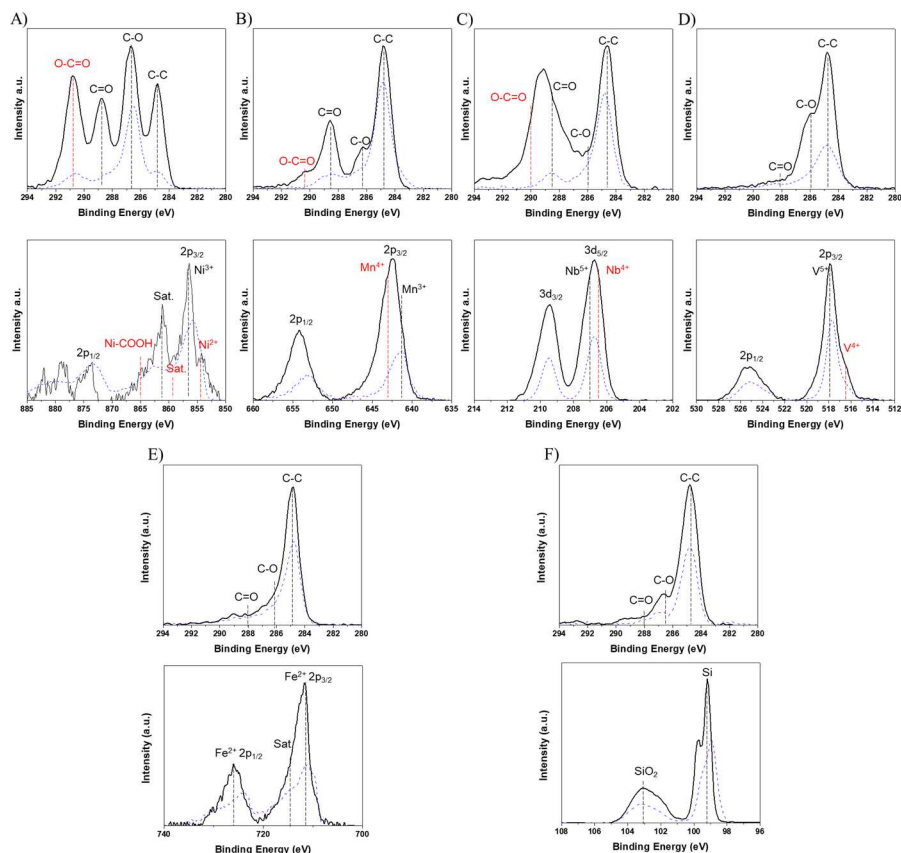
Figure 4.10: Interface Analysis of Ionogel/Electrode Systems

XPS analysis of the formic acid with a molarity corresponding to a pH of 1.6 exposed to (A) NCA, LMO, (C) Nb_2O_5, (D) V_2O_5, (E) a-Si, and (F) LFP. The C ls spectrum and corresponding transition metal spectrum for each material is displayed. The unreacted electrode powder spectrum is displayed as the blue dotted line. The corresponding species are shown for the identified peaks. The reacted species are identified (red).

TEM imaging of the electrode materials was performed before and after exposure to the formic acid solution to ascertain whether morphological changes occurred (Figure 4.11). The images indicate that exposure to the acid does not affect the morphology of LMO, Nb_2O_5, and LFP (Figure 4.11B-C, 4.11E). For NCA and V_2O_5 though, a morphological change observed after exposure to the formic acid can be correlated to dissolution (Figure 4.11A,4.11D). Dissolution of V_2O_5 during cycling or in acidic media is a common issue in

the battery community so its occurrence here is not unusual.[44] The dissolution of V_2O_5 can help explain why a lower capacity was achieved with the ionogel even though similar XPS results to Nb_2O_5 were obtained. Si was not imaged due to its direct processing on a substrate.
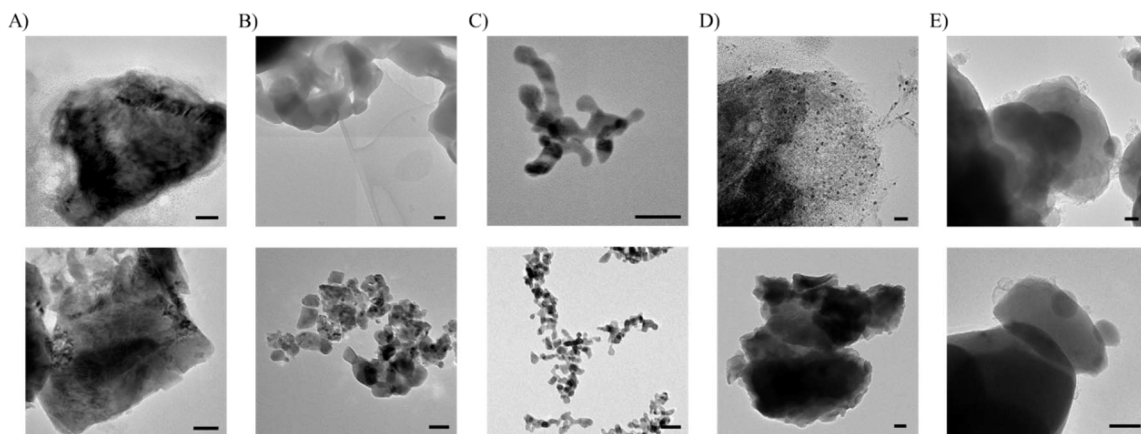
Figure 4.11: Topological Relationship with Ionogel Stability

TEM imaging of formic acid exposed (A) NCA, (B) LMO, (C) Nb_2O_5, (D) V_2O_5, and (E) LFP. The unreacted materials are shown for comparison. All scale bars are 50 nanometers.

4.3.4 Ionogel Modification

This study has established that the acidic catalyst used in the sol-gel process is the source of ionogel-electrode interface reactions which, in turn, have a significant effect on electrochemical properties. To circumvent these reactions, the well-understood silica sol-gel chemistry is used to shift the sol acidity into a stable pH region. Moving the sol to a higher pH by using less acid or a weaker acid can influence the gelation mechanism, which affects gel morphology and porosity.[45,46] With increasing pH, the gelation mechanism will change from electrophilic attack of the end group Si atoms to nucleophilic attack on the central Si atoms. This can decrease the pore size and thus decrease the ionic conductivity. As shown by

Sharp, et al., the use of mild, nonaqueous acids (pK_a >4) also leads to drastically decreased gelation rates.[47] Since a single catalyst does not seem to be beneficial, a two-step catalyst sol-gel route was developed. In this process, the first step involves hydrolysis in the low pH range followed by pH adjustment with a base. The intent of this approach is to maintain the desired pore structure (low pH) and move the processed sol into a pH range that is compatible with LCO. The two-step process has been shown to achieve similar porosities to that of a strong acid catalyzed silica gel.[48]
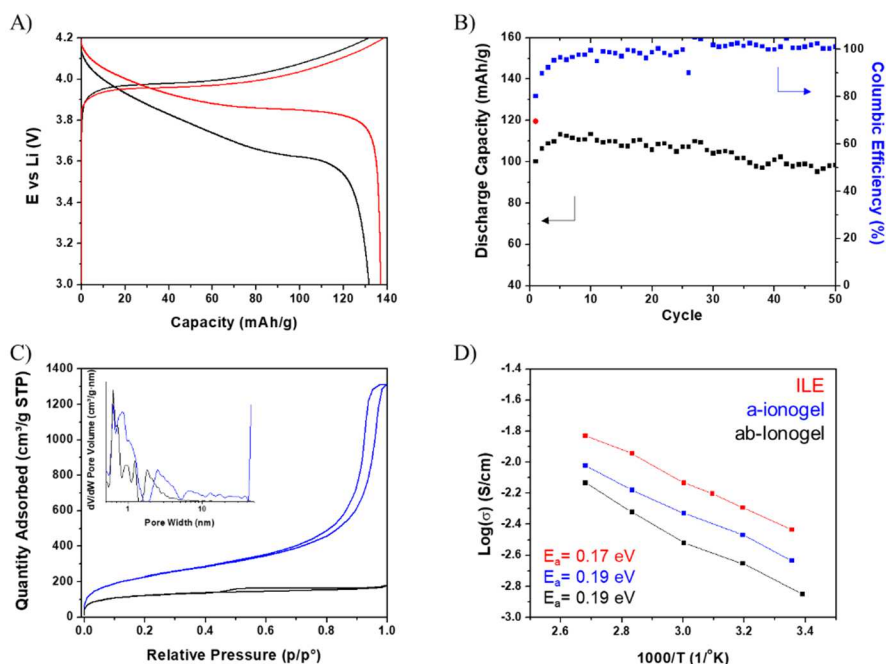
Figure 4.12: Two-Step Modified Ionogel Properties

A) Galvanostatic measurements of the modified ionogel spun onto LCO at C/10 (black). Comparison to ILE is shown (red). (B) Capacity variation with cycling for the ab-ionogel on LCO. All cycles were performed at C/5. The capacity for the 2nd cycle of LCO cycled in ILE at C/5 is provided as a comparison in red. (C) N2 adsorption isotherm for the ab-ionogel sol (black). The isotherm for a-ionogel is provided (blue). An inset is provided for the pore distribution calculated through DFT. (D) Temperature dependence of the ionic conductivity for the modified gel. The ab-ionogel is compared to the neat ILE and a-ionogel. The activation energies are shown.

89

Lithium hydroxide was chosen to adjust the sol pH over organic bases to limit the percentage of organics in the solution that can form an interfacial layer and hinder cycling. The original gel synthesis route (formic acid only) will be herein referred to as a-ionogel and the LiOH-modified synthesis as the ab-ionogel. LiOH has the additional benefit of adding lithium to the system while not adding bulky anions that can increase the viscosity and thus decrease the ionic conductivity. The water produced from the hydroxide was removed along with the trace amount of water from the sol-gel reaction through a heating step. The concentration of added LiOH was calculated to adjust the pH to 4 which was shown earlier to be stable to LCO. Cycling of the ab-ionogel cast onto an LCO electrode obtained capacities comparable to the neat ILE at C/10 (Figure 4.12A, 133 mAh/g). After a few conditioning cycles, a maximum capacity of 110 mAh/g was achieved at C/5 that showed only a 0.2% per cycle drop in capacity over 50 cycles (Figure 4.12B). The obtained capacity at C/5 matches well to the capacity of the system cycled in ILE.

The ab-ionogel was analyzed through N_2 adsorption and EIS to measure the porosity and ionic conductivity, respectively (Figure 4.12C-D). The isotherm demonstrates the ab-ionogel maintains a high surface area of 415 m^2/g with an average pore size comparable to the a-ionogel. The ionic conductivities of the ionogels are quite similar. The a-ionogel is slightly more conductive than the ab-ionogel (1.4 mS/cm vs 2 mS/cm at room temperature) with comparable activation energy (0.19 eV). The lower conductivity can be correlated with the decreased porosity of the modified gel due to the addition of the base. While lower than a-ionogel, the conductivity of the modified ionogel is still significantly greater than other solid electrolyte systems, such as LiPON.[49]

Interfacial reactions between LCO and the modified ionogel were characterized with Raman spectroscopy and XPS. For the Raman spectroscopy, LCO was exposed to the LiOH ionogel sol and aged for one week before analysis. The Raman spectrum indicates there is no discernable reaction between the gel and LCO interface as only peaks characteristic of the ILE, SiO$_2$ matrix, and LCO are evident (Figure 4.13A). For the XPS experiments, LCO powder was exposed to a LiOH-modified formic acid solution. XPS analysis confirms the Raman data with no indication of Co reduction or organic formation (Figure 4.13B). As the modified gel is not material dependent, it should be readily applied to other material systems, thus enabling ionogels to be incorporated in a wider range of cell chemistries.
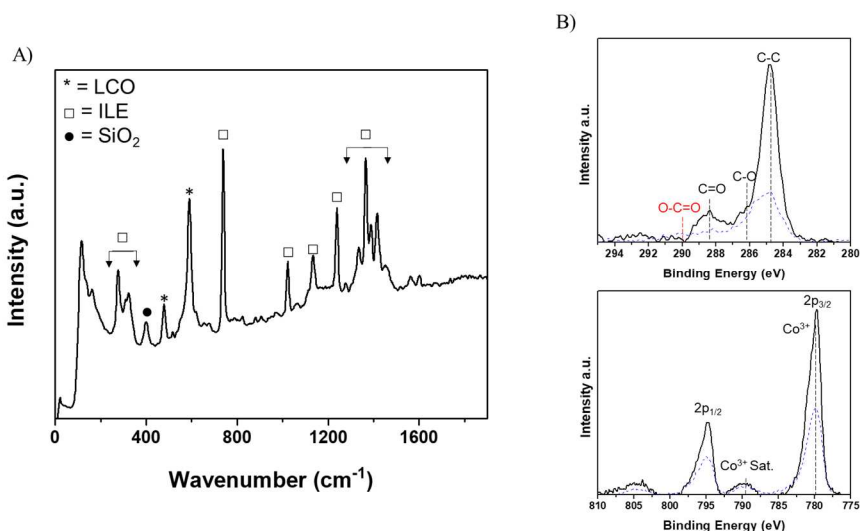
Figure 4.13: Analyzing the LCO/LiOH Ionogel Interface

A) Raman spectroscopy on LCO that was exposed to the ab-ionogel sol. The peaks for LCO (*), ILE (□), and SiO$_2$ (●) are labeled. (B) XPS analysis of LCO powder exposed to a LiOH-Formic acid solution corresponding to the ab-sol. The C 1s and Co 2p spectra are provided.

4.4 Conclusion

Ionogels have recently attracted interest as Li^+ solid electrolytes due to their exemplary physiochemical properties and ability to be solution processed, but the lack of information about the interfacial instability with many electrode materials limits their application. In this study, we demonstrated that the low pH of the sol, originating from the acid catalyst, reduces the Co in LCO and catalyzes organic formation on the surface, which hindered the electrochemical cycling. The degree and pathway of chemical attack is material dependent, with many common Li^+ cathodes and anodes being susceptible to transition metal reduction and organic formation. The chemical attack can be overcome by adjusting the sol-gel process to conditions within the pH stability window of the active material. Using a 2-step, acid-base catalyzed sol-gel synthesis, stable cycling of a LCO/ionogel system was attained, while maintaining the properties of the trapped ionic liquid electrolyte. Though demonstrated only for LCO, the acid-base catalyzed ionogel can be adapted readily to improve the stability of other electrode/ionogel systems. This modification allows the ionogel electrolyte system to be better utilized in various energy storage designs increase their commerciality.

4.5 References

1. Raj, A. & Steingart, D. Review—Power Sources for the Internet of Things. *J. Electrochem. Soc.* **165**, 3130–3136 (2018).

2. Hess, S., Wohlfahrt-Mehrens, M. & Wachtler, M. Flammability of Li-Ion Battery Electrolytes: Flash Point and Self-Extinguishing Time Measurements. *J. Electrochem. Soc.* **162**, A3084–A3097 (2015).

3. Manthiram, A., Yu, X. & Wang, S. Lithium battery chemistries enabled by solid-state electrolytes. *Nat. Rev. Mater.* **2**, 1–16 (2017).

4. Sakuma, M., Suzuki, K., Hirayama, M. & Kanno, R. Reactions at the electrode/electrolyte interface of all-solid-state lithium batteries incorporating Li-M (M = Sn, Si) alloy electrodes and sulfide-based solid electrolytes. *Solid State Ionics* **285**, 101–105 (2016).

5. Han, F., Zhu, Y., He, X., Mo, Y. & Wang, C. Electrochemical Stability of $Li_{10}GeP_2S_{12}$ and $Li_7La_3Zr_2O_{12}$ Solid Electrolytes. *Adv. Energy Mater.* **6**, 1501590 (2016).

6. Richards, W. D., Miara, L. J., Wang, Y., Kim, J. C. & Ceder, G. Interface Stability in Solid-State Batteries. *Chem. Mater.* **28**, 266-273 (2016).

7. Zhu, Y., He, X. & Mo, Y. First principles study on electrochemical and chemical stability of solid electrolyte–electrode interfaces in all-solid-state Li-ion batteries. *J. Mater. Chem. A* **4**, 3253–3266 (2016).

8.   Le Bideau, J., Ducros, J. B., Soudan, P. & Guyomard, D. Solid-state electrode materials with ionic-liquid properties for energy storage: The lithium solid-state ionic-liquid concept. *Adv. Funct. Mater.* **21**, 4073–4078 (2011).

9.   Delannoy, P. E.; Riou, B.; Lestriez, B.; Guyomard, D.; Brousse, T.; Le Bideau, J. Toward Fast and Cost-Effective Ink-Jet Printing of Solid Electrolyte for Lithium Microbatteries. *J. Power Sources* **2015**, *274*, 1085–1090.

10.   Lee, A. S.; Lee, J. H.; Hong, S. M.; Lee, J. C.; Hwang, S. S.; Koo, C. M. Boronic Ionogel Electrolytes to Improve Lithium Transport for Li-Ion Batteries. *Electrochim. Acta* **2016**, *215*, 36–41.

11.   Li, X., Zhang, Z., Yang, L., Tachibana, K. & Hirano, S.-I. TiO_2-based ionogel electrolytes for lithium metal batteries. *J. Power Sources* **293**, 831–834 (2015).

12.   Reale, P., Fernicola, A. & Scrosati, B. Compatibility of the $Py_{24}TFSI$-LiTFSI ionic liquid solution with $Li_4Ti_5O_{12}$ and $LiFePO_4$ lithium ion battery electrodes. *J. Power Sources* **194**, 182–189 (2009).

13.   Kim, J. K., Matic, A., Ahn, J. H. & Jacobsson, P. An imidazolium based ionic liquid electrolyte for lithium batteries. *J. Power Sources* **195**, 7639–7643 (2010).

14.   Ashby, D. S., DeBlock, R. H., Lai, C. H., Choi, C. S. & Dunn, B. S. Patternable, Solution-Processed Ionogels for Thin-Film Lithium-Ion Electrolytes. *Joule* **1**, 344–358 (2017).

15.   Kim, J. W., Augustyn, V. & Dunn, B. The Effect of Crystallinity on the Rapid Pseudocapacitive Response of Nb_2O_5. *Adv. Energy Mater.* **2**, 141–148 (2012).

16.   Smith, L. C.; Malati, P.; Fang, J.; Richardson, W.; Ashby, D.; Lai, C.-H.; Dunn, B. S. Sol–gel Encapsulated Lithium Polysulfide Catholyte and Its Application in Lithium–sulfur Batteries. *Mater. Horiz.* **2016**, *3* (2), 137–144.

17.   Lee, J. H. *et al.* Hybrid ionogel electrolytes for high temperature lithium batteries. *J. Mater. Chem. A* **3,** 2226–2233 (2015).

18.   Tan, G. et al. Solid-State Li-Ion Batteries Using Fast, Stable, Glassy Nanocomposite Electrolytes for Good Safety and Long Cycle-Life. *Nano Lett.* **16**, 1960–1968 (2016).

19.   Mizushima, K., Jones, P. C., Wiseman, P. J. & Goodenough, J. B. Li_xCoO_2 ($0<x\leq1$): A new cathode material for batteries of high energy density. *Mater. Res. Bulltein* **15**, 783–789 (1980).

20.   Tan, H., Takeuchi, S., Bharathi, K. K., Takeuchi, I. & Bendersky, L. A. Microscopy Study of Structural Evolution in Epitaxial $LiCoO_2$ Positive Electrode Films during Electrochemical Cycling. *ACS Appl. Mater. Interfaces* **8**, 6727–6735 (2016).

21.   Horowitz, A. I. & Panzer, M. J. High-performance, mechanically compliant silica-based ionogels for electrical energy storage applications. *J. Mater. Chem*. **22**, 16534–16539 (2012).

22.   Matsumoto, H.; Sakaebe, H.; Tatsumi, K.; Kikuta, M.; Ishiko, E.; Kono, M. Fast Cycling of $Li/LiCoO_2$ Cell with Low-Viscosity Ionic Liquids Based on Bis(Fluorosulfonyl)Imide $[FSI]^-$. *J. Power Sources* **2006**, *160*, 1308–1313.

23. Brinker, C. J. Hydrolysis and Condensation of Silicates. *J. Non. Cryst. Solids* **100**, 31–50 (1988).

24. Huang, W. & Frech, R. Vibrational spectroscopic and electrochemical studies of the low and high temperature phases of $LiCo_{1-x}M_xO_2$ (M = Ni or Ti). *Solid State Ionics* **86**, 395–400 (1996).

25. Kiefer, J., Fries, J. & Leipertz, A. Experimental Vibrational Study of Imidazolium-Based Ionic Liquids : Raman and Infrared Spectra of 1-Ethyl-3-methylimidazolium Bis(trifluoromethylsulfonyl)imide and 1-Ethyl-3-methylimidazolium Ethylsulfate. *Appl. Spectrosc.* **61**, 1306–1311 (2007).

26. Diallo, A., Beye, A. C., Doyle, T. B., Park, E. & Maaza, M. Green synthesis of Co_3O_4 nanoparticles via Aspalathus linearis: Physical properties. *Green Chem. Lett. Rev.* **8**, 30–36 (2015).

27. Hassner, A. & Alexanian, V. Direct room temperature esterification of carboxylic acids. *Tetrahedron Lett.* **19**, 4475–4478 (1978).

28. Bacarella, A. L., Grunwald, E., Marshall, H. P. & Purlee, E. L. The potentiometric measurement of acid dissociation constants and pH in the system methanol-water. pKa, values for carboxylic acids and anilinium ions. *J. Org. Chem.* **20**, 747–762 (1955).

29. Xu, B., Liu, X., Haubrich, J., Madix, R. J. & Friend, C. M. Alcohol Oxidation Selectivity Control in Gold-Mediated Esterification of Methanol. *Angew. Chem. Int. Ed.* **48**, 4206–4209 (2009).

30. Moreno-Castilla, C., Carrasco-Marın, F., Parejo-Perez, C. & Lopez Ramon, M. V. Dehydration of methanol to dimethyl ether catalyzed by oxidized activated carbons with varying surface acidic character. *Carbon* **39**, (2001).

31. Zhou, Y., Dong, C.-K., Han, L., Yang, J. & Du, X.-W. Top-Down Preparation of Active Cobalt Oxide Catalyst. *ACS Catal*. **6**, 32 (2016).

32. Schmidt-Szaøowski, K., Krawczyk, K. & Petryk, J. The properties of cobalt oxide catalyst for ammonia oxidation. *Appl. Catal. A Gen*. **175**, 147–157 (1998).

33. Li, Y.; Qiu, W.; Qin, F.; Fang, H.; Hadjiev, V. G.; Litvinov, D.; Bao, J. Identification of Cobalt Oxides with Raman Scattering and Fourier Transform Infrared Spectroscopy. *J. Phys. Chem. C*, **120** (8), 4511–4516. (2016)

34. Nayl, A. A., Elkhashab, R. A., Badawy, S. M. & El-Khateeb, M. A. Acid leaching of mixed spent Li-ion batteries. *Arab. J. Chem.* **10,** S3632–S3639 (2017).

35. Pinna, E. G., Ruiz, M. C., Ojeda, M. W. & Rodriguez, M. H. Cathodes of spent Li-ion batteries: Dissolution with phosphoric acid and recovery of lithium and cobalt from leach liquors. *Hydrometallurgy* **167**, 66–71 (2017).

36. Nayaka, G. P. et al. Recovery of valuable metal ions from the spent lithium-ion battery using aqueous mixture of mild organic acids as alternative to mineral acids. *Hydrometallurgy* **151**, 73–77 (2015).

37. Zeng, X., Li, J. & Shen, B. Novel approach to recover cobalt and lithium from spent lithium-ion battery using oxalic acid. *J. Hazard. Mater*. **295**, 112–118 (2015).

38. Lai, C. H. *et al.* Designing Pseudocapacitance for Nb_2O_5/Carbide-Derived Carbon Electrodes and Hybrid Devices. *Langmuir* **33,** 9407–9415 (2017).

39. Benedek, R. Role of Disproportionation in the Dissolution of Mn from Lithium Manganate Spinel. *J. Phys. Chem. C* **121**, 22049–22053 (2017).

40. Hunter, J. C. Preparation of a new crystal form of manganese dioxide: λ-MnO_2. *J. Solid State Chem.* **39**, 142–147 (1981).

41. Huang, Y. *et al.* Thermal Stability and Reactivity of Cathode Materials for Li-Ion Batteries. *ACS Appl. Mater. Interfaces* **8,** 7013–7021 (2016).

42. Li, H. et al. Recovery of Lithium, Iron, and Phosphorus from Spent $LiFePO_4$ Batteries Using Stoichiometric Sulfuric Acid Leaching System. *ACS Sustain. Chem. Eng.* **5**, 8017–8024 (2017).

43. Zheng, R. et al. Optimized Li and Fe recovery from spent lithium-ion batteries via a solution-precipitation method. *RSC Adv.* **6**, 43613–43625 (2016).

44. Skyllas-Kazacos, M. & Limantari, Y. Kinetics of the chemical dissolution of vanadium pentoxide in acidic bromide solutions. *J. Appl. Electrochem.* **34**, 681–685 (2004).

45. Horowitz, A. I., Westerman, K. & Panzer, M. J. Formulation influence on the sol–gel formation of silica-supported ionogels. *J. Sol-Gel Sci. Technol.* **78**, 34–39 (2016).

46. Brinker, C. J. & Scherer, G. W. Sol- Gel Glass: I. Gelation and Gel Structure. *J. Non. Cryst. Solids* **70**, 301–322 (1985).

47. Sharp, K. G. & Scherer, G. W. Interaction of Formic Acid with the Silica Gel Network. *J. Sol-Gel Sci. Technol.* **171**, 165–171 (1997).

48.   Sharp, K. G. A Two-Component, Non-Aqueous Route to Silica Gel. *J. Sol-Gel Sci. Technol.* **2**, 35–41 (1994).

49.   Pearse, A. J. et al. Nanoscale Solid State Batteries Enabled by Thermal Atomic Layer Deposition of a Lithium Polyphosphazene Solid State Electrolyte. *Chem. Mater.* **29**, 3740–3753 (2017).

Chapter 5: Fabrication of an All-Solid State 2.5D Battery

In current battery designs, the gravimetric and areal capacities of planar and stacked electrodes are restricted by the electrode electronic and ionic diffusion distances. Herein, the fabrication and properties of a multidimensional, high areal-capacity 2.5D battery is described. The battery is composed of a 3D $LiFePO_4$ array, a planar anode, and the solution-processable ionogel electrolyte. Due to the solution-processability and high ionic conductivity (2 mS cm^{-1}) of the ionogel electrolyte, appreciable current densities can be obtained between the planar anode and the 3D cathode. The resulting device configuration demonstrates high areal capacities at fast cycling rates of 1.1 mAh cm^{-2} at 1 mA cm^{-2} (4.6 mWh cm^{-2} at 1.4 mW cm^{-2}) with uniform electrolyte access to the 3D cathode. The 2.5D device demonstrates comparable energy and power densities to the best 3D batteries in literature while having a simpler fabrication process. These results present a promising direction for the integration of high performance, electrochemical energy storage devices into on-chip devices and microelectronic applications.

5.1 Introduction

Technological advancement in the last several decades has been driven by the miniaturization of electronics.[1] With electronics shrinking, the need for smaller energy storage devices (i.e. microbatteries) that still maintain high energy and power densities has increased accordingly. While electronic fabrication technology has steadily progressed, energy-storage device design has lagged behind. To achieve high energy densities, current battery designs stack or roll electrodes, which increases the percentage of the cell consisting of separators or current collectors. This not only increases the volume of the cell, which limits the specific capacity, but also

increases the cost. Dense planar electrodes have been fabricated using solid-state electrolytes for microelectronic applications to increase the volumetric capacity, but these devices have a trade-off between energy and power density.[2] High areal capacities using these devices have been obtained by scaling the film thickness, but this increases the diffusion distance for both electrons and ions which can severely hinder the power density.[3] For these reasons, 3D electrodes have been increasingly explored as a means to maximize the areal capacity while not limiting the device's power density.

Three-dimensional (3D) batteries were first proposed in the early 2000's by Rolison, et al. as a novel design to deliver high areal energy densities while maintaining acceptable power density and cycling stability.[4] The 3D design takes advantage of the third dimension, height, to increase the amount of electrode within a footprint area. Through intertwining 3D architectures, the ion diffusion distance between electrodes is kept short, essentially decoupling the energy and power density. Several electrode architectures have been fabricated using ALD deposition[5,6] 3D printing,[7,8] templating[9,10,] or electrodeposition.[11,12] Energy densities which are an order of magnitude higher than planar films have been achieved in the 3D structures at appreciable power densities, but many of these designs have inherent limitations which limit the cell performance. Formation of internal short circuits or voids has limited the build success rate and performance of the cells.[9,13,14] Incorporating a conformal electrolyte for an all solid-state device also reduces the achievable power density due to the inherently low ionic conductivity of materials designed for conformal coatings ($\sim 10^{-8}$-10^{-6} S cm^{-1}).[15–17]

In literature, discussion of non-planar batteries have focused on 3D batteries. However, recent interest has arisen for other multidimensional architectures, such as "2.5D" batteries. 2.5D batteries, consisting of a 3D electrode partnered with a 2D planar electrode, were recently proposed as a means of simplifying the fabrication issues typically found in traditional 3D batteries and increase the functional electrolyte and electrode selection. By not needing a second 3D electrode, the chances of having voids and short-circuits during electrode alignment/filling is reduced. Further, as a conformal solid electrolyte is no longer needed, a solid electrolyte with high ionic conductivity can be used as a replacement for liquid electrolytes to create a high power, all-solid-state device. Several studies on these 2.5D or "semi-3D" architectures have shown that high areal capacities (>1 mAh cm^{-2}) can be achieved at reasonable cycling rates. While these semi-3D structures were designed for 3D batteries, they demonstrate the feasibility of fabricating a 2.5D device. Recent multiphysics-based modeling by Mckelvey et, al. of a 2.5D system has also emphasized that for electrolyte ionic conductivities above 10^{-3} S cm^{-1}, theoretical capacities can be achieved in high aspect ratio devices at appreciable power densities.[18] A key result of this analysis is that the ionic conductivity of the electrolyte is the limiting factor for both the energy and power densities. A key result of their analysis was that the ionic conductivity of the electrolyte is the limiting factor to achieve high, electrochemical performance 2.5D batteries. The analysis by Mckelvey et al. underscores the importance of choosing high ionic conductivity electrolytes, such as ionogels, for these multidimensional batteries. Though 2.5D devices generally have a simpler fabrication process, this is dependent on the fabrication route and material choice. Ionogels, a subclass of solid electrolytes composed of a room temperature molten salt (ionic

liquid, ILE) confined within an inorganic or organic matrix, have demonstrated promising properties for LIB. In research to date, ionogels have been adapted as high ionic conductivity Li^+ electrolytes in planar batteries as thin films,[19] ink-jet printing,[20] and cast bulk films.[21] These materials have not been explored in 3D electrode architectures.

In this study, we fabricated an all-solid state 2.5D battery consisting of a 3D $LiFePO_4$ (LFP) post array and a planar anode separated by a solution-processed ionogel electrolyte. 3D LFP posts were fabricated through slurry infiltration to obtain a 5:1 aspect ratio cathode. Ionogel electrolyte is shown to infiltrate uniformly throughout the array and penetrate into the individual posts. The ionogel-infiltrated posts were cycled against Li metal and a-Si in full cell devices demonstrating capacities up to 1.1 mAh cm^{-2} at 1 mA cm^{-2} (4.1 mWh cm^{-2} at 2.8 mW cm^{-2}). These cells were shown to be stable over 50 cycles at 500 µA cm^{-2} with a 99% capacity retention. In comparison against 3D devices, the 2.5D Li cell demonstrates energy and power densities comparable to the best devices while having a simpler design.

5.2 Experimental Procedures

5.2.1 Ionogel Synthesis

Tetramethylorthosilicate (TMOS, 99+%, Sigma Aldrich), triethylvinylorthosilcate (VTEOS, 97%, Sigma Aldrich), and formic acid (Puram, Fluka Analytical) were purchased for the silica sol-gel reaction. Lithium bis(trifluoromethanesulfonyl)imide (LiTFSI, 99.95%, Sigma Aldrich) and l-butyl-3-methylimidazolium bis(trifluoromethanesulfonyl)imide ([BMIM] [TFSI], 99.5%, Solvionic) were obtained for the ionic liquid electrolyte.

103

Ionic liquid was first degassed using a vacuum oven and bubbled with Ar at 150°C before storing inside an Ar gas filled, l ppm H_2O glovebox. 0.5M LiTFSI BMIM TFSI ionic liquid electrolyte (ILE) was then prepared from the degassed ionic liquid. The ionogel fabrication and processing parameters were reported in a previous paper.[19]

5.2.2 Electrode Fabrication

The silicon mold templates were fabricated following a published procedure.[22] In brief, the patterns for silicon molds were defined by lithographic techniques using AZ5214-E photoresists, and silicon dioxide grown by plasma-enhanced CVD (STS Multiplex CVD) served as a hard mask. Using a Plasma-Therm Versaline DSE II, deep reactive ion etching (DRIE) was performed to anisotropically etch channels through the silicon.

LiFePO$_4$ (LFP; MTI), Ketjen Black EC300J (Lion Specialty Chemicals Co.), Timrex KS4 graphite (MTI), polyvinylidene fluoride (PVDF Sigma Aldrich) and 1-methyl-2-pyrrolidinone (NMP 99.5% anhydrous, Sigma Aldrich) were used without further processing. Electrode slurries were made with 70 wt % LiFePO$_4$, 8 wt % KS4, 13 wt % Ketjen Black, and 9 wt % PVDF dispersed in NMP. The slurry was infiltrated into the Si mold using a high-pressure syringe pump inside a Whatman filter holder (14 mg cm^{-2} mass loading). Pelco Conductive Carbon Glue (Ted Pella) was used to adhere the infiltrated molds onto a stainless steel substrate. A XeF$_2$ dry etching process (homebuilt etcher) was used isotropically etch the silicon after filling the mold. The freestanding posts were infiltrated with ionogel sol and let sit overnight to dry. Before testing, the infiltrated electrodes were dried overnight in a 110 °C oven.

Amorphous boron doped, silicon anode films were deposited by electron beam physical vapor deposition (CHA Mark 40, CHA Industries) onto a stainless steel substrate with a thickness of 300 nm.

5.2.3 Array Characterization

SEM was performed using a FEI Nova 230 Nano SEM with attached EDS. Imaging and EDS mapping were performed on the 3D $LiFePO_4$ cathodes and ionogel infiltrated electrode. Cross sections were obtained by sectioning the LFP cathode and ionogel infiltrated cathode. The longitudinal and latitudinal cuts were performed approximately halfway through the post array.

Raman Analysis (Renishaw inVia confocal Raman microscope) was performed on planar LFP films before and after exposure to the XeF_2 gas. Analysis was performed with a 514 nm Ar laser and 1800/mm grating through a 20x objective lens.

X-ray photoelectron spectroscopy (XPS; Kratos Axis Ultra) with a monochromatic aluminum X- ray source was used to probe the surface of the LFP posts after exposure to the XeF_2. Peak calibration was performed using the adventitious carbon peak.

5.2.4 Electrochemical Characterization

3-electrode half-cells were tested using a 3-neck flask containing 10 ml of ILE and a Li metal counter and reference electrode. The cathode consisted of a freestanding LFP array or one infiltrated with ionogel. The 2.5D full cells were constructed by pressing a planar Li or a-Si electrode against the ionogel-infiltrated LFP array. The full cells were cycled without packaging inside an Ar filled glovebox. Galvanostatic (GV) and electrochemical impedance spectroscopy (EIS) measurements were made using a BioLogic VMP3 potentiostat. GV measurements were performed between 2.5-4V for the LFP-Li cells and 0.5-3.9V for the

LFP-Si cells. The cells were cycled at rates from 50-5000 μA cm^{-2}. Long term cycling was conducted at 500 μA cm^{-2} for 50 cycles. EIS was performed from 1MHz to 100 mHz with a 10 mV amplitude. For reference, planar LFP electrodes fabricated through doctor-blade deposition were constructed in a two-electrode configuration versus lithium metal with a 0.5M LiTFSI [BMIM] [TFSI] electrolyte.

5.3 Results & Discussion

5.3.1 Fabrication of the 2.5D Device

Fabrication of a 2.5D microbattery has many similarities to fabrication of a 3D battery, but it differs in several key areas. In both cases, production of a 3D electrode array is needed to obtain high areal capacities. In 3D batteries, this array is typically coated with a conformal electrolyte and backfilled with a complementary electrode material or interdigitated with a second 3D electrode array and backfilled with a liquid electrolyte.[7,9] In either electrode configuration, low ionic conductivity of the conformal electrolyte, shorting from nonuniform electrolyte coverage, or void formation has limited 3D battery commerciality. 2.5D batteries differ as a solution-processable solid electrolyte can backfill the array and be combined with a planar electrode instead of requiring a conformal/liquid electrolyte and second electrode array (Figure 5.1). This design simplifies the fabrication process and allows for a greater flexibility in geometric design and material choice.
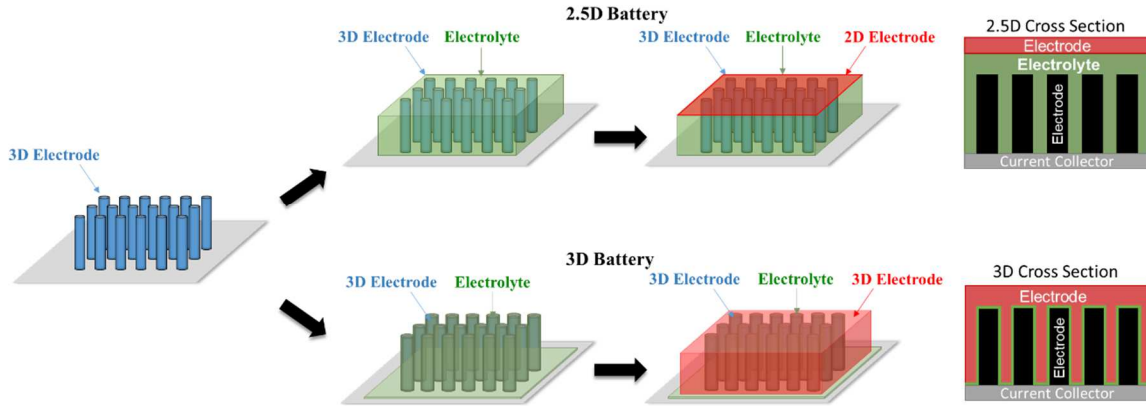
Figure 5.1: Multidimensional Battery Architectures
Diagram representing the design differences between 3D and 2.5D batteries.

In fabricating the 2.5D battery, first a 3D LFP post array was created using a silicon template adapted from Cirigilano.[22] The template was formed using deep reactive ion etching (DRIE) on a Si wafer to give a 15x15 post array with a 100 micron pitch between posts. The molds were designed in a 5:1 aspect ratio with 100x500 micron dimensions. A slight increase in diameter is seen at the bottom of each post pattern due to the scalloping during the DRIE etching process. By using a syringe pump, the LFP slurry was infiltrated uniformly through the mold and dried before adhering to a stainless steel current collector. After mounting, the Si template can be selectively removed using a XeF_2 etch to give a freestanding LFP array. An overview of the process is provided in Figure 5.2.
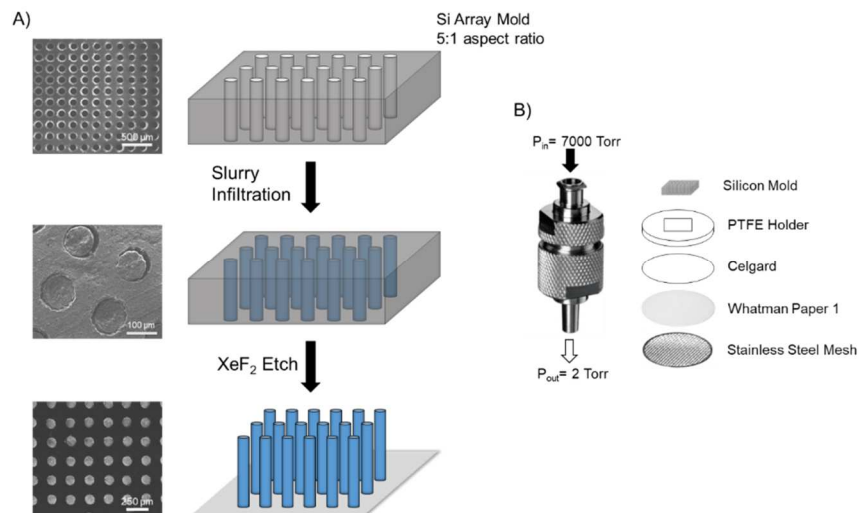
Figure 5.2: Fabrication Process of the 3D Cathode Array

A) Schematic of the required steps to infiltrate the Si mold and remove the template to obtain a freestanding array. SEM images are provided of the posts/mold at each step of the process with 500, 50, and 250 micron scale bars, respectfully. (B) Diagram of the slurry infiltration setup.

LFP was selected because of its previously shown stability to the ionogel sol. Due to the simplicity of the fabrication process, other electrode materials can be easily incorporated into the design to tailor the electrochemical performance. After etching the template, the freestanding cathode array was infiltrated with ionogel sol. The ionogel sol was fabricated using a process described previously.[18] The ionogel sol consists of a homogenous mixture of silica sol and ionic liquid that exhibits low viscosity. The low viscosity allows the sol to incorporate uniformly through the post array and penetrate into the posts (Figure 5.3A). When gelation occurs, the sol forms a solid network around the posts producing a mechanically rigid solid electrolyte that has high ionic conductivity. The homogenous distribution of ILE in the gel ensures uniform electrolyte access to all of the LFP. Once gelation is complete and the water is removed through heating, a planar electrode can be partnered on the infiltrated array to produce a 2.5D cell. The infiltrated array was

cycled against Li and Si as high volumetric capacity materials are required to match the high areal loading of the array.
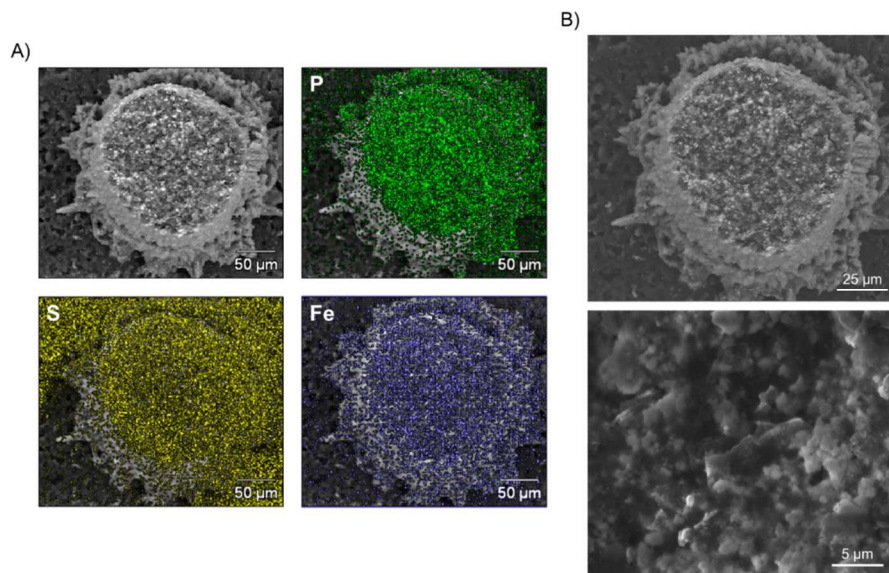

Figure 5.3: Cross-sectional Analysis of LFP Posts

A) EDS mapping of a SEM cross-section of an ILE-infiltrated LFP array shows the penetration of the ILE component identified from S. LFP can be identified from the P and Fe signal. (B) SEM cross-section of an ILE-infiltrated LFP array. A magnified image is provided to demonstrate the porosity.

The LFP posts were analyzed before infiltration to understand the physiochemical properties. SEM imaging of the posts shows the array is relatively free of defects and has sufficient mechanical stability for infiltration (Figure 5.4A). The image also demonstrates that the posts are geometrically uniform throughout the length. The porosity and electronic conductivity of the posts were measured after etching the template (Table 5.1). Using a two-point probe setup, the electronic conductivity of the posts was determined to be approximately 50 mS cm^{-1} which is on the same order of magnitude as planar cast electrodes.[23] Assuming a uniform resistance, the voltage drop arising from the electronic resistance across the array should only be 4 mV at 1 mA cm^{-}

[2]. A calculated porosity of 35% was estimated based on the measured weight and geometric dimensions. This porosity matches well to what is seen in planar slurry electrodes.[24] The porosity is high enough to allow for sufficient electrolyte access without affecting the mechanical integrity of the posts. SEM imaging of the LFP post-cross-section demonstrates the porosity is uniform through the post with no indication of voids or inclusions (Figure 5.3B).
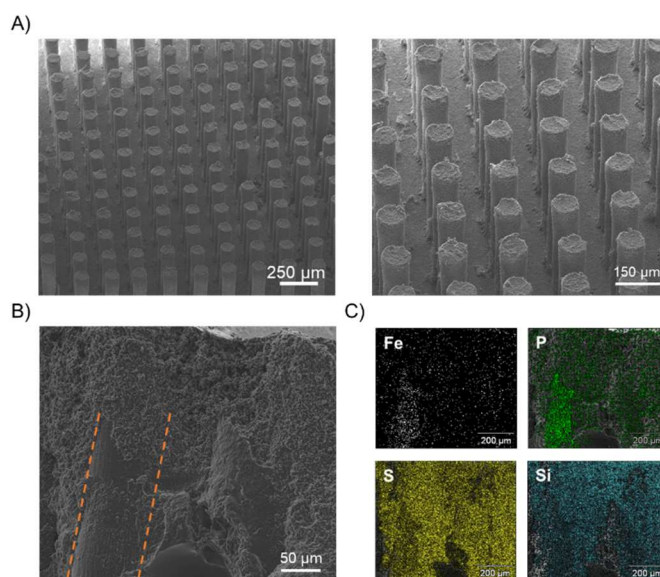
Figure 5.4: Microscopic Analysis of the 2.5D Battery

A) SEM image of the LFP posts after removal of the Si template. A magnified image of the array is provided. The scale bar corresponds to 250 and 150 microns, respectfully. (B) Cross-sectional SEM image of the posts after ionogel infiltration. An outline of a post is provided in orange. The scale bar corresponds to 50 microns. (D) EDS analysis of the ionogel infiltrated cross section. The post can be identified from the P and Fe spectrum. The ionogel is identified from S and Si.

). Previous work has demonstrated a high electrolyte ionic conductivity of 2 mS cm^{-1} at room temperature, sufficiently high enough to not hamper the electrochemical performance.[18] SEM imaging and EDX of the LFP/ionogel post array shows infiltration occurs uniformly throughout the array while not affecting the mechanical stability of the posts (Figure 5.4C and 5.4D). A

cross-section analysis of the ionogel infiltrated array demonstrate that ILE and SiO_2 are able to penetrate uniformly into the post (Figure 5.5). The electronic properties of the Si or Li metal are not expected to inhibit the cycling performance of the 2.5D cell.

Table 1: Cell Physiochemical Properties

Physiochemical properties for the components of the 2.5D cell.

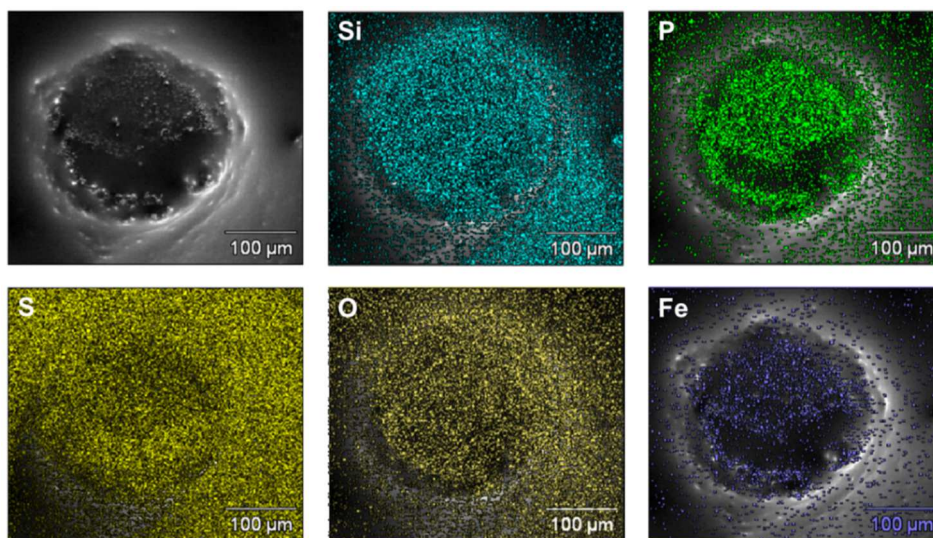| Post Electronic Conductivity (100 μm)	~50 mS cm^{-1}
Porosity	~35%
Ionic Conductivity	2 mS cm^{-1}
Si Electronic Conductivity	2.5 mS cm^{-1}

Figure 5.5: Topographical and Penetration Ability of Ionogels

SEM cross-section of an ionogel-infiltrated LFP array. EDS mapping shows the penetration of the ILE and SiO_2 components Si, and S. LFP can be identified from the P and Fe signal.

111

5.3.2 Electrochemical Performance

Electrochemical cycling was first performed on the 3D LFP array in an ILE, 3-electrode setup to understand the innate characteristics of the array. Figure 5.6A demonstrates the electrochemical cycling of the posts. A blowup of the low capacity region is provided. The cycling shows a high OCV (3.5V) and essentially zero capacity from the posts in the initial charge. During discharge, a capacity of 1.55 mAh cm^{-2} was obtained which is close to theoretical values calculated from the post density and geometry (1.8 mAh cm^{-2}), but at a lithiation voltage much lower than expected for LFP. After the first cycle of the posts in ILE, the capacity retention reduces to 25% (0.375 mAh cm^{-2}), but the cell does maintain satisfactory rate capability. SEM imaging of the posts after cycling in ILE shows post fracture, which helps explains the low capacity achieved after the first cycle (Figure 5.6B). It is unclear why the fracture occurred with relithiation as LFP is known to have a low volume change during lithium cycling (6.8%).[25] The fracturing could stem from high density regions of voids or inclusions originating from the fabrication process.[26] Subsequent cycling of the array for 50 cycles show a stable capacity indicating that, after the initial lithiation step, the surviving posts are mechanically stable (Figure 5.6C).
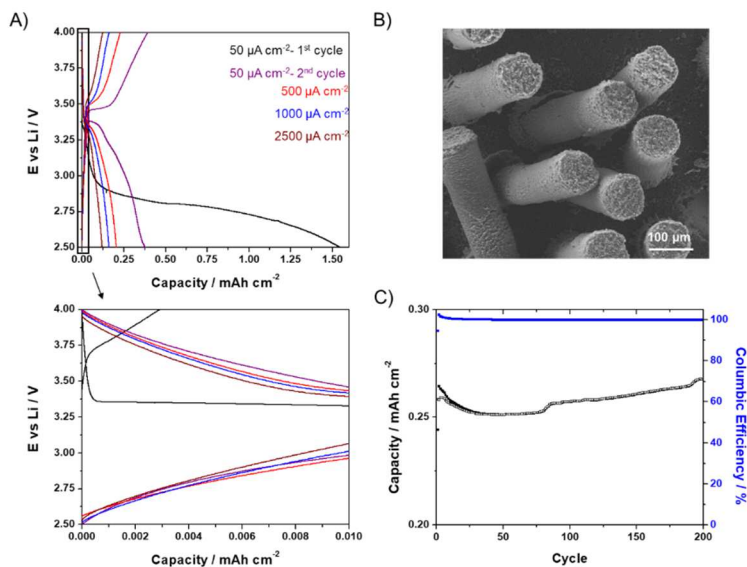
Figure 5.6: Electrochemical Performance of the 3D Cathode

A) Galvanostatic cycling of the LFP posts in an ILE half-cell. All cycles correspond to the 3rd cycle at that current density. The low capacity region is magnified to show the first charge. (B) SEM imaging of the LFP posts after cycling. Posts were rinsed with MeOH before imaging. (C) Capacity variation with cycling for the half cell. Cycling stability was performed at 0.5 mA cm⁻².

The irregular first cycle behavior indicates that the XeF_2 etching process might be affecting the cycling performance. To understand the relationship, Raman spectroscopy of the LFP electrode was performed before and after XeF2 etching. The data suggests that the system became delithiated after exposure forming $FePO_4$, which explains the low capacity in the first cycle (Figure 5.7A). All unidentified Raman peaks are associated with $LiFePO_4$.[27] The XeF_2 induced delithiation can be explained by the formation of LiF on the surface, which is inactive in Raman spectroscopy. XPS analysis after XeF_2 etching could only identify a dominant F signal along with O and C which indicates that a thick, surface fluoride layer could be affecting lithium intercalation (Figure 5.7B). As Li has a low signal to noise ratio in XPS, it is difficult to discern whether there is a change in the lithiation state. In order to understand the effect of the XeF_2 etching, impedance spectroscopy of the cell was performed before and after cycling (Figure

113

5.8A). Tracking the frequency of the initial interfacial resistances at 140 and 3 Hz, a decrease is seen for both interfaces after cycling. The interfaces are most likely related to the LFP charge transfer resistance (140 Hz) and the fluorine compound that forms from the XeF_2 etch (3 Hz). The decrease in the resistance with cycling can be attributed to the relithiation of the LFP and dissolution of the fluorine compound after exposure to the electrolyte. Dissolution of the fluorine is supported by the impedance of an ionogel-infiltrated sample that shows a much smaller initial interfacial resistance than the ILE sample (Figure 5.8B). The decrease of the fluoride interface resistance with exposure to the ionogel could originate from the acidity of the sol, lengthier exposure time, or exposure to elevated temperatures during the water removal step.
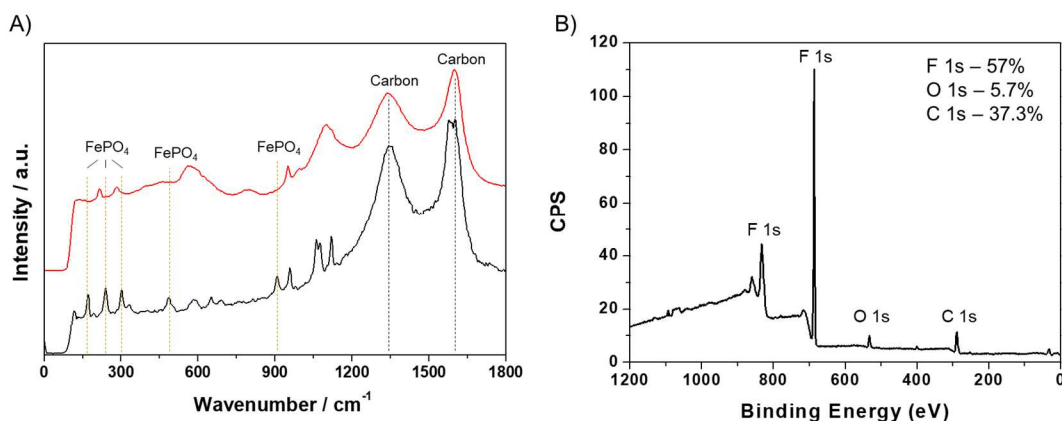

Figure 5.7: Processing Conditions effect on the 3D cathode

A) Raman analysis of the LFP electrode before (red) and after (black) XeF_2 exposure. (B) XPS analysis of the LFP electrode after XeF_2 exposure. The concentration percentage of the identified elements are provided.
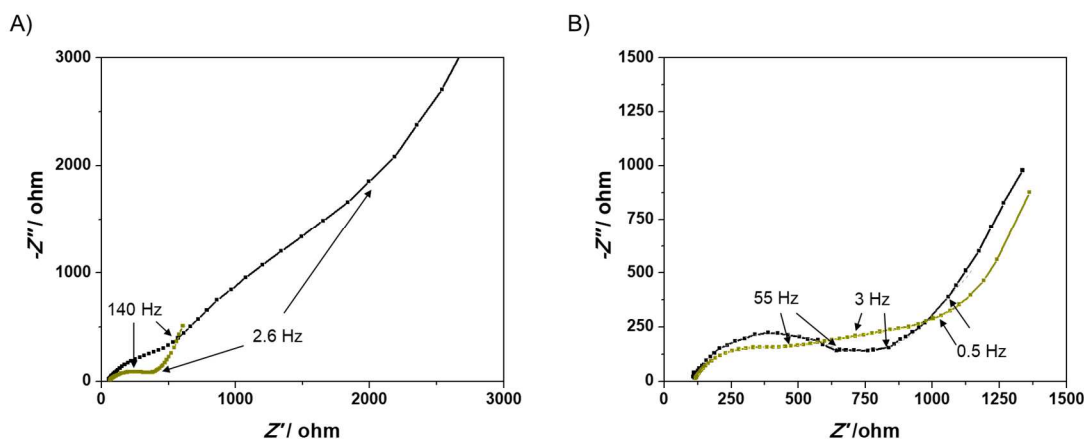
Figure 5.8: Interfacial Analysis of the 3D Cathode

A) Impedance analysis of the ILE half-cell before (black) and after cycling (gold). The frequency is provided corresponding to the interfaces. (B) Impedance analysis of the ionogel half-cell before (black) and after cycling (gold). The frequency is provided corresponding to the interfaces.

Cycling of the LFP array that was infiltrated with ionogel electrolyte shows a significantly improved response. The cell was cycled in a 3-cell setup with excess ionic liquid electrolyte and a Li metal counter and a reference electrode. Figure 5.9A shows that capacities of 1.2 mAh cm^{-2} are achieved at 50 μA cm^2. All cycles shown correspond to the third cycle at that rate. High capacities of 0.35 mAh cm^{-2} are maintained at fast charging rates of 5 mA cm^{-2}. Long-term cycling was performed at 0.5 mA cm^{-2} for 50 cycles after the rate capability test (Figure 5.9B). The cell maintained 99% of its capacity over the 50 cycles and there was no loss of capacity from cycling at faster rates. Comparing the results in Figure 5.9 and Figure 5.6, the capacity is shown to be significantly higher for the ionogel-infiltrated sample than the ILE cycled array at all sweep rates. The higher capacity obtained after relithiation suggests that the ionogel provides sufficient mechanical support to keep the majority of the posts from fracturing. While there is a loss of capacity from the first and second cycle, it is significantly less than that seen for the ILE cycled sample. The initial charge capacity for the ionogel is significantly higher than the ILE

sample supporting the potential prelithiation of the 3D cathode. It is a possible the lithiation

helps avoid mechanical failure of the posts during cycling. The improved capacity and kinetics

can be explained by the removal of the fluoride surface layer and relithiation of the LFP as seen

by the decrease in the interfacial resistances (Figure 5.8B). The impedance spectrum indicates

that the posts are only partially relithiated initially as seen by the drop of the LFP charge transfer

resistance with cycling (55Hz). The impedance spectrum does show that SEI is forming on the

surface with cycling which can partially explain the lower capacity obtained between the first

and second cycle.
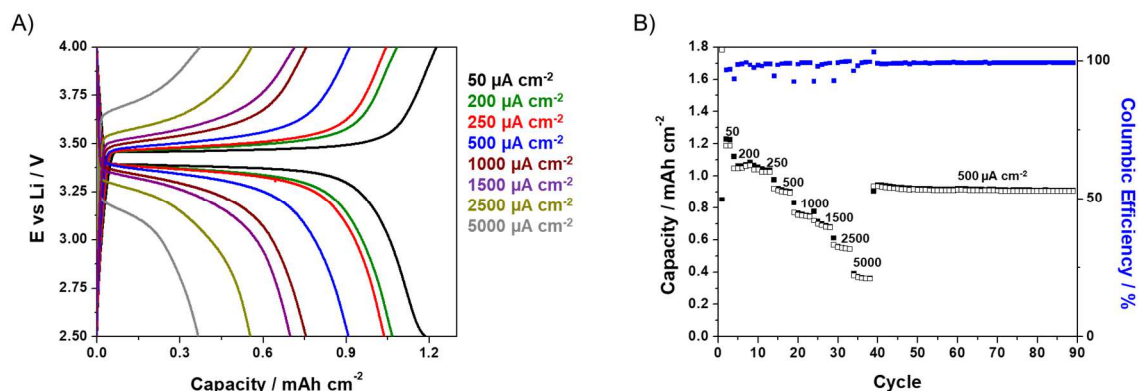
Figure 5.9: Electrochemical Performance of 2.5D Half Cell Batteries

A) Galvanostatic cycling of the ionogel infiltrated LFP posts in a Li half-cell. All cycles correspond to the 3rd cycle at that current density. (B) Capacity variation with cycling for the half-cell. Cycling stability was performed at 0.5 mA cm^{-2}.

2.5D devices were fabricated from the 3D LFP posts and planar Li and Si. These devices

were cycled in a two-electrode setup with no external packaging inside an Ar glove box. Cycling

of the Li 2.5D battery showed similar behavior to that of the 3-electrode cell. Figure 5.10a shows

the galvanostatic cycling of the 2.5D device from 50-5000 µA cm^{-2}. Capacities as high as 1.4

mAh cm^{-2} were obtained at 50 µA cm^{-2}. With the short distance between the electrodes, high capacity was retained even at fast rates (0.31 mAh cm^{-2} at 5 mA cm^{-2}). Long-term cycling was performed at 0.5 mA cm^{-2} for 50 cycles after testing the rate capability (Figure 5.10B). The capacity was maintained over the 50 cycles with no loss of capacity from cycling at faster rates. The high cycling stability and good rate capability indicate that the ionogel can act as a sufficient ion conductor and physical separator in a 2.5D device. The poorer columbic efficiency can be associated to the lithium anode reaction with trace amount of water and oxygen in the glove box. A 2.5D device was also fabricated using planar a-Si to demonstrate a device for on-chip applications. Due to the high volume expansion of Si, the thickness of the Si was limited to 300 nm which did not allow capacity matching of the electrodes.[28] Figure 5.10C demonstrates the galvanostatic cycling of the 2.5D device using a-Si (0.35 mAh cm^{-2} at 50 µA cm^{-2}). This matches close to the expected capacity of 0.4 mAh cm^{-2} for a 300 nm Si cell. The lower rate capability obtained for the Si than Li 2.5D cell most likely is due to material loss from the volume expansion masking the true capacity at faster rates. The cycling demonstrates that with proper design, the 2.5D design can be used for high capacity, on-chip applications. Further work is required to optimize the Si anode to better match the high areal capacity of the 3D cathode.

A)

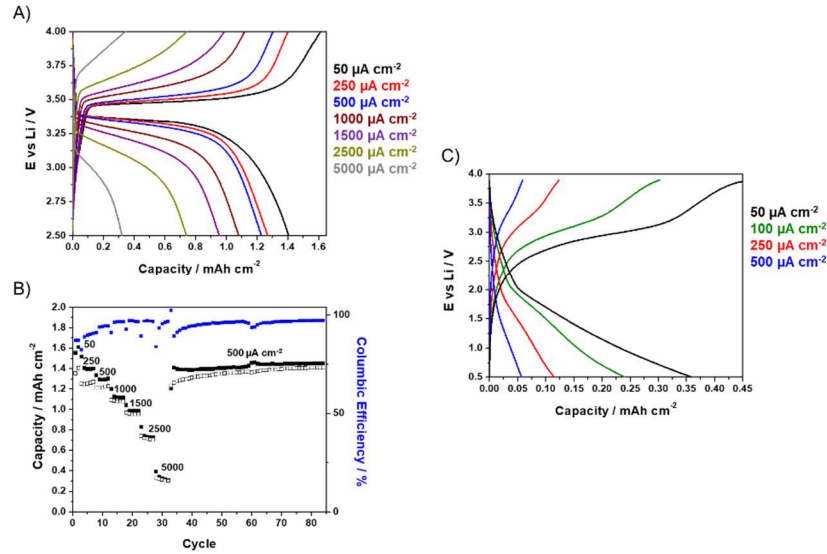**Figure 5.10: Electrochemical Cycling of a 2.5D Battery**

A) Galvanostatic cycling of ionogel infiltrated LFP post/Li full cell. All cycles correspond to the 3rd cycle at that current density. (B) Capacity variation with cycling for the LFP post/Li full cell. Cycling stability was performed at 0.5 mA cm^{-2}. (C) Galvanostatic cycling of ionogel infiltrated LFP post/Si full cell. All cycles correspond to the 3rd cycle at that rate.

5.3.3 Microbattery Comparison

As mentioned above, multidimensional batteries have been fabricated in several different geometries for Li$^+$ batteries. The energy and power densities of these devices range widely based on the electrode dimensions and the electrolyte (Table 5.2). Examples include 3D printed,[7,10] patterned,[11,12,29] and templated structures.[9,13,30] Sun, et al. demonstrated that by using ink-jet printing, high areal capacities could be achieved even at fast rates (0.9 mAh cm^{-2} at 7.1 mA cm^{-2}).[7] While high power densities were achieved, the use of a liquid electrolyte creates packaging limitations and restricts the usage in microelectronic devices. Patterning and other techniques have been applied to fabricate 3D networks, but low mass loadings have limited the available areal capacity as seen by Ning, et al. work with an inverse-opal structure.[11] Templates, ranging from inverse molds to pillared structures, have also been used to create 3D structures.[5,9] Depending on

118

the material deposition method, the obtained capacity and power density ranged widely. Hur, et al. demonstrated that by using a conformal electrolyte coating, high areal capacities could be obtained from a Si/NCA array (2.8 mAh cm^{-2} at 110 μA cm^{-2}), but the low ionic conductivity and volume expansion of the Si limited the cyclability and rate capability. In contrast, Pearse, et al. demonstrated remarkable rate capability through an all-solid-state battery deposited using ALD, but only achieved low capacities because of the low material loadings (3.5 μAh cm^{-2} at 10 mA cm^{-2}).[5] These systems demonstrate that for the majority of 3D battery designs a compromise exists between the energy and power density stemming from the electrode material choice, electrolyte conductivity, and material loading. By moving to the simpler fabrication process of 2.5D materials, there is less need to compromise the material choice and loading allowing for high power and energy densities.

Table 5.2: 3D Batteries Electrochemical performance

Comparison of the electrochemical performance of reported 3D batteries. The architectures were designed in several different geometries using multiple fabrication techniques. Electrolyte, material loading, and electrode dimensions vary between the reported devices. The current result is in red.

Electrodes	Electrode Geometry	Electrode Height (um)	Aspect Ratio	Electrolyte	Capacity (mAh cm^{-2})	Charge Rate (mA cm^{-2})	Reference
LFP-Li	Pillar	500	5	Ionogel	1.4 / 1.1	0.050 / 1	This Work
LCO/Li	Thin Film	2.5	NA	LiPON	0.130 / 0.032	0.015 / 5.25	[3]
LCO/LTO	3D printed	30	1.5	PMMA/LiClO4	0.270 / 0.170	0.420 / 2.65	[10]
LFP/LTO	3D printed	420	14	1M LiClO4 EC:DMC	1.5 / 0.9	1.48 / 7.1	[7]
LMO/NiSn	Inverse Opal	14.9 / 12.6	0.45 / 0.45	1M LiClO4 EC:DMC	0.08 / 0.007	0.120 / 17.5	[11]
LMO/NiSn	Holographic Pattern	10	0.29	1M LiClO4 EC:DMC	0.045 / 0.006	0.045 / 45	[12]
V2O5/SnOx	Silicon Array	300	10	LiPON	0.02 / 0.0035	0.1 / 10	[5]
LCO/Si	Si Cone Array	4	2.5	LiPON	0.025 / 0.003	0.0037 / 0.028	[13]
Si/NCA	Pillar	400	4	SU8	2.8 / 0.5	0.11 / 0.66	[9]

Figure 5.11 presents a Ragone plot of the energy and power densities of multidimensional batteries presented in Table 2. We believe the plot represents an accurate comparison of the higher energy or power density 3D batteries existing in the literature. As seen from the plot, many of the 3D devices have excellent power densities due to the short diffusion distance between the electrodes, but there is a trade-off with a lower energy density. The microbattery fabricated by Dudney is included as it is representative of a planar battery. The 2.5D device described here not only shows high energy densities but also comparable high power densities because of the high ionic conductivity and solution processability of the ionogel electrolyte that allows for uniform electrode infiltration (2.8 mWh cm^{-2} at 9 mW cm^{-2}). Only the 3D printed device by Lewis, et al. has comparable performance, but these cells used a liquid electrolyte.[7] This illustrates that ionogel can act as a viable solid-state replacement for liquid electrolytes in multidimensional batteries while offering higher thermal and electrochemical stability. While this paper demonstrates a 2.5D device with excellent cycling performance, there is still an ever-increasing need to improve the energy and power density for microelectronics. By changing the electrolyte or post geometry, it is possible to tune the energy and power density of the 2.5D battery. The physiochemical properties of ionogels have been shown to be adaptable either through varying the ionic liquid or the matrix formulation.[31–33] This allows for control of the ionic conductivity, temperature range where fluidity is maintained, and electrochemical window. As the molds are fabricated through a simple templating method, the 2.5D cell can be improved by focusing on optimizing the post height, diameter, and pitch through modeling and experimental data to achieve the highest areal energy and power densities. This paper has focused on using LFP as the

cathode because of its stability to the ionogel electrolyte; but, by modifying the ionogel synthe-

sis, stability can be achieved for other cathodes with higher specific capacities or improved rate

capability. The nature of the 2.5D system allows for these adaptations to be incorporated simulta-
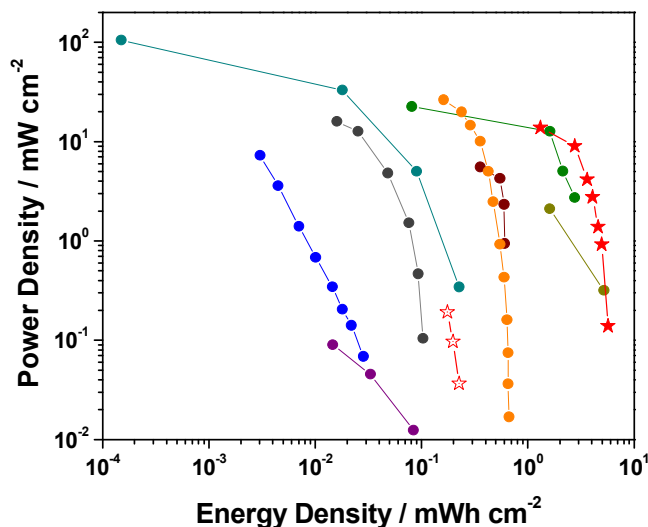
neously or in an incremental manner.

Figure 5.11: Ragone Plot of Multidimensional Batteries

**Ragone plot of varying multidimensional battery architectures. All plotted samples corre-
spond to the data in Table 2. A thin-film planar cell is provided as comparison (orange).
This papers work is marked with red stars. The planar cell is marked with open red stars.**

5.4 Conclusion

In this chapter, we have described the fabrication of a 2.5D battery consisting of a 3D

LFP post array cathode, ionogel electrolyte, and planar lithium or silicon anodes. By using the

innate solution processability of a Li^+ conducting ionogel, the electrolyte can uniformly penetrate

the array to act as a Li^+ reservoir and a physical separator between the 3D cathode and 2D anode.

The use of the ionogel electrolyte in a 2.5D architecture simplifies the fabrication process while

allowing for outstanding electrochemical performance. Cycling of a Li anode-2.5D cell demonstrated capacities of 1.1 mAh cm^{-2} at 1 mA cm^{-2} (3.7 mWh cm^{-2} at 2.5 mW cm^{-2}). The device has energy and power densities comparable to the best-reported 3D microstructures with the added advantage of being all solid state. The nature of the ionogel and post-fabrication process allows a high degree of flexibility in adjusting the performance of the cell to meet desired specifications. Future work will focus on optimizing the cell design to achieve the highest areal energy and power densities.

5.5 References

1.   Raj, A. & Steingart, D. Review—Power Sources for the Internet of Things. *J. Electrochem. Soc.* **165,** 3130–3136 (2018).

2.   Wang, Y. *et al.* Lithium and lithium ion batteries for applications in microelectronic devices: A review. *J. Power Sources* **286,** 330–345 (2015).

3.   Dudney, N. J. Solid-state thin-film rechargeable batteries. *Mater. Sci. Eng. B* **116,** 245–249 (2005).

4.   Hart, R. W., White, H. S., Dunn, B. & Rolison, D. R. 3-D Microbatteries. *Electrochem. commun.* **5,** 120–123 (2003).

5.   Pearse, A. *et al.* Three-Dimensional Solid-State Lithium-Ion Batteries Fabricated by Conformal Vapor-Phase Chemistry. *ACS Nano* **12,** 4286–4294 (2018).

6.   Liu, J., Zhu, H. & Shiraz, M. H. A. Toward 3D Solid-State Batteries via Atomic Layer Deposition Approach. *Front. Energy Res.* **6,** 1–5 (2018).

7.   Sun, K. *et al.* 3D printing of interdigitated Li-ion microbattery architectures. *Adv. Mater.* **25,** 4539–4543 (2013).

8.   Fu, K. *et al.* Graphene Oxide-Based Electrode Inks for 3D-Printed Lithium-Ion Batteries. *Adv. Mater.* **28,** 2587–2594 (2016).

9.   Hur, J. I., Smith, L. C. & Dunn, B. High Areal Energy Density 3D Lithium-Ion Microbatteries. *Joule* **2,** 1187–1201 (2018).

10.   Yoshima, K., Munakata, H. & Kanamura, K. Fabrication of micro lithium-ion battery with

3D anode and 3D cathode by using polymer wall. *J. Power Sources* **208,** 404–408 (2012).

11. Ning, H. *et al.* Holographic patterning of high-performance on-chip 3D lithium-ion microbatteries. *Proc. Natl. Acad. Sci.* **112,** 6573–8 (2015).

12. Pikul, J. H., Gang Zhang, H., Cho, J., Braun, P. V. & King, W. P. High-power lithium ion microbatteries from interdigitated three-dimensional bicontinuous nanoporous electrodes. *Nat. Commun.* **4,** 1732 (2013).

13. Talin, A. A. *et al.* Fabrication, Testing, and Simulation of All-Solid-State Three-Dimensional Li-Ion Batteries. *ACS Appl. Mater. Interfaces* **8,** 32385–32391 (2016).

14. Arthur, T. S. *et al.* Three-dimensional electrodes and battery architectures. *MRS Bull.* **36,** 523–531 (2011).

15. Choi, C. S. *et al.* Synthesis and Properties of a Photopatternable Lithium-Ion Conducting Solid Electrolyte. *Adv. Mater.* **30,** 1703772 (2018).

16. Chen, N. *et al.* Nanoscale, conformal polysiloxane thin film electrolytes for three-dimensional battery architectures. *Mater. Horizons* **2,** 309–314 (2015).

17. Pearse, A. J. *et al.* Nanoscale Solid State Batteries Enabled by Thermal Atomic Layer Deposition of a Lithium Polyphosphazene Solid State Electrolyte. *Chem. Mater.* **29,** 3740–3753 (2017).

18. McKelvey, K., Talin, A. A., Dunn, B. & White, H. S. Microscale 2.5D Batteries. *J. Electrochem. Soc.* **164,** A2500–A2503 (2017).

19. Ashby, D. S., DeBlock, R. H., Lai, C. H., Choi, C. S. & Dunn, B. S. Patternable, Solution-

Processed Ionogels for Thin-Film Lithium-Ion Electrolytes. *Joule* **1,** 344–358 (2017).

20.   Delannoy, P. E. *et al.* Toward fast and cost-effective ink-jet printing of solid electrolyte for lithium microbatteries. *J. Power Sources* **274,** 1085–1090 (2015).

21.   Le Bideau, J., Ducros, J. B., Soudan, P. & Guyomard, D. Solid-state electrode materials with ionic-liquid properties for energy storage: The lithium solid-state ionic-liquid concept. *Adv. Funct. Mater.* **21,** 4073–4078 (2011).

22.   Cirigliano, N. *et al.* 3D Architectured Anodes for Lithium-Ion Microbatteries with Large Areal Capacity. *Energy Technol.* **2,** 362–369 (2014).

23.   Peterson, S. W. & Wheeler, D. R. Direct Measurements of Effective Electronic Transport in Porous Li-Ion Electrodes. *J. Electrochem. Soc.* **144,** 2175–2181 (2014).

24.   Taleghani, S. T., Marcos, B., Zaghib, K. & Lantagne, G. A Study on the Effect of Porosity and Particles Size Distribution on Li-Ion Battery Performance. *J. Electrochem. Soc.* **164,** E3179–E3189 (2017).

25.   Padhi, A. K., Nanjundaswamy, K. S. & Goodenough, J. B. Phospho-olivines as Positive-Electrode Materials for Rechargeable Lithium Batteries. *J. Electrochem. Soc.* **144,** 16 (1997).

26.   Cirigliano, N. Primary and Secondary Three Dimensional Microbatteries. (University of California, Los Angeles, 2012).

27.   Burba, C. M. & Frech, R. Raman and FTIR Spectroscopic Study of Li_xFePO_4 ($0 \leq x \leq 1$). *J. Electrochem. Soc.* **151,** A1032 (2004).

28.   Jerliu, B. *et al.* Volume Expansion during Lithiation of Amorphous Silicon Thin Film Electrodes Studied by In-Operando Neutron Reflectometry. *J. Phys. Chem. C* **118,** 9395–9399 (2014).

29.   Min, H. S. *et al.* Fabrication and properties of a carbon/polypyrrole three-dimensional microbattery. *J. Power Sources* **178,** 795–800 (2008).

30.   Kotobuki, M. *et al.* Fabrication of Three-Dimensional Battery Using Ceramic Electrolyte with Honeycomb Structure by Sol–Gel Process. *J. Electrochem. Soc.* **157,** A493 (2010).

31.   Lee, A. S. *et al.* Boronic ionogel electrolytes to improve lithium transport for Li-ion batteries. *Electrochim. Acta* **215,** 36–41 (2016).

32.   Viau, L. *et al.* Ionic Liquid Mediated Sol-Gel Synthesis in the Presence of Water or Formic Acid: Which Synthesis for Which Material? *Chem. Mater.* **24,** 3128–3134 (2012).

33.   Ong, S. P., Andreussi, O., Wu, Y. & Marzari, N. Electrochemical Windows of Room-Temperature Ionic Liquids from Molecular Dynamics and Density Functional Theory Calculations. *Chem. Mater.* **23,** 2979–2986 (2011).

Chapter 6: Summary and Future Direction

The use of liquid electrolytes in LIBs has increasingly limited the safety and energy density of commercial cells. Solid electrolytes have been explored as safe alternatives, but their poor electrochemical stability and processing issues have curbed their use in commercial devices. A pseudo-solid electrolyte (ionogel), where ionic liquid was trapped inside a solid, mesoporous matrix, is explored in this dissertation as an alternative to solid-state electrolytes. Ionogels maintain the properties of the trapped ionic liquid, which allows the gels to preserve high ionic conductivities and a high electrochemical and physiochemical stability. The use of the sol-gel process lets the electrolyte to be processed as a solution, which allows the electrolyte to be uniformly incorporated through complex 3D structures. This high conductivity and solution-processability helps address the issues associated with solid-state electrolytes.

Chapter 3 demonstrates a novel way to process ionogel electrolytes through a spin-coating method to achieve low electrolyte resistances. The work highlights the importance of the processing conditions on achieving good electrolyte wetting. As the ionogel is solution processable, it is able to penetrate uniformly through a $LiFePO_4$ cast electrode, acting as a Li^+ reservoir. The uniform penetration enables the construction of low resistance, high power density cells. In comparison, electrolytes processed as a solid have poor electrode/electrolyte contact that leads to high bottleneck resistance for ion diffusion. Solid electrolytes will be unable to achieve widespread use if the processing conditions are not improved to allow for better wetting.

The sol-gel process was further modified in Chapter 3 by the addition of a photoacid generator to control the local gelation through a UV source. The ability to pattern the electrolyte increases the processing versatility, allowing complex battery geometries to be designed for on-

chip and microbattery applications. This versatility is especially important as battery designs have gradually miniaturized to keep pace with microelectronic technologies. While patternable, the photopolymerization process requires further optimization to better control the interaction of the UV-produced acid with the ionic liquid to allow for higher resolution and thicker films to be deposited.

The electrode/electrolyte interface is one of the least studied aspects of solid electrolytes, but also one of the most limiting aspects in battery devices. As demonstrated in Chapter 4, LCO, among other electrode materials, is not stable to the solution-processable ionogel electrolyte. The chapter further elucidated that the instability originates from the acid catalyst used in the sol-gel reaction that causes reduction of the transition metal and formation ethers and esters on the surface through the catalysis of alcohols and the carboxylic acid. The reduced transition metal and alkali metal can further dissolve in solution. This attack is shown to be pH dependent, with increasing pHs improving the stability of the interface. Because of the instability, current ionogel research is restricted in the possible cell designs because of the lack of understanding of the sol-gel's reaction with electrode materials. The chapter demonstrates that by using a 2-step acid base catalyst the instability can be avoided. The modification of the sol-gel reaction is important as it allows not only stable cycling, but also the creation of high energy and power density cells using new, designer cathodes without hindrance from high interfacial resistances. This modified sol-gel process is not yet optimized and can be further improved. This will be especially important in developing ionogel electrolytes for high performance electrode materials.

The solution processability of the ionogel offers unique opportunities to use in complex-geometry cell designs, such as multidimensional batteries. These opportunities are further improved when the stability of LFP to the ionogel sol is taken into consideration. Using the ionogel electrolyte, a 2.5D battery was fabricated from a 3D LFP cathode and a 2D Li metal anode (Chapter 5). The ionogel is shown to infiltrate uniformly through the LFP array and individual posts. This provides mechanical stability to the posts, a reservoir of Li^+ ions, and electronic isolation of the electrodes. High energy and power densities are achieved with this design, comparable to the best 3D batteries in literature. It should be noted that the 2.5D design greatly simplifies the fabrication process, which increases the build success rate of the battery. The 2.5D design also allows the energy and power densities to be controlled by tuning the electrolyte, material choice, and architecture. By changing the sol-gel process or ionic liquid, higher ionic conductivities are possible, which decreases the electrolyte resistance allowing for high power densities. The use of NCA, LCO, or other cathode materials would also increase the voltage, capacity, and rate capability of the cell with little change required to the fabrication process. The use of the other cathodes are possible through our understanding of the ionogel/electrode interface. Modification of the 3D electrode architecture to smaller diameter posts with a decreased pitch would increase the theoretical capacity by two times and have the possibility to increase the rate capability. Another benefit of the 2.5D design is that these improvements can be applied incrementally or all at once to better tailor the device to meet the cell requirements.